SPECTROSCOPIC FACTORS NEAR THE R-PROCESS PATH USING COMBINED MEASUREMENTS: ^{86}Kr$(d,p)^{87}$Kr AND ^{84}Se$(d,p)^{85}$Se

By

DAVID GREGORY WALTER

A dissertation submitted to the

School of Graduate Studies

Rutgers, The State University of New Jersey

in partial fulfillment of the requirements

for the degree of

Doctor of Philosophy

Graduate Program in Physics and Astronomy

written under the direction of

Professor Jolie A. Cizewski

and approved by

_____

_____

_____

_____

New Brunswick, New Jersey

October, 2018

ABSTRACT OF THE DISSERTATION

Spectroscopic factors near the r-process path using combined measurements: $^{86}\mathbf{Kr}(d,p)^{87}\mathbf{Kr}$ and $^{84}\mathbf{Se}(d,p)^{85}\mathbf{Se}$

By DAVID GREGORY WALTER

Dissertation Director:

Professor Jolie A. Cizewski

Modern nuclear structure models suggest that the shell structure near the valley of stability, with well-established shell closures at N=50, for example, changes in very neutron-rich nuclei far from stability. Single-particle properties of nuclei away from stability can be probed in single-neutron (d,p) transfer reactions with beams of rare isotopes. The interpretation of these data requires reaction theories with various effective interactions. Often, approximations made to the final neutron bound-state introduce a large uncertainty in the extracted spectroscopic factor. To mitigate this uncertainty, Mukhamedzhanov and Nunes have proposed a combined, two-measurement method, where the external contribution of this bound-state wave function is fixed using a peripheral reaction, and is combined with a higher energy measurement with

a larger contribution from the nuclear interior. By constraining the asymptotic behavior, the method enables spectroscopic factors to be deduced with uncertainties dominated by experimental statistics rather than the bound-state potential.

The (d, p) neutron transfer reaction with 35 MeV/u beams of ^{86}Kr has been measured at the National Superconducting Cyclotron Laboratory (NSCL) to test this method. The reaction protons were detected with the Oak Ridge Rutgers University Barrel Array (ORRUBA) and Silicon Detector Array (SIDAR), arrays of segmented silicon strip detectors, the first implementation of such a configuration with fast beams at the NSCL. These measurements at 35 MeV/u were combined with previous studies of the ^{86}Kr(d, p) reaction at 5.5 MeV/u to test the combined method. The bound-state potential for the ground state of ^{87}Kr was successfully constrained by extracting an asymptotic normalization coefficient (ANC) consistent with both the high- and low-energy measurements, which provides a corresponding constrained spectroscopic factor of $S = 0.44^{+0.09}_{-0.13}$ for the ground state of ^{87}Kr.

Although a constrained bound-state potential for other low-lying states was not achieved, the successful results for the ground state prompted a study of the $d(^{84}\text{Se},p)^{85}\text{Se}$ reaction. The low-energy ANC analysis based on previously published results is presented in this work as well as preliminary results from the higher energy measurement using radioactive ion beams of ^{84}Se at 45 MeV/u at the NSCL.

Acknowledgments

Im fortunate to have many supportive people in my life that have helped me along the way. Of course, there are many people I could thank, but rather than filling up the dissertation with an homage to everyone, here are a select few.

First I would like to thank my parents and my bothers who have encouraged me to follow the path of being a scientist despite having to live far away from each other, which in my opinion is the hardest part of this career path.

Caitlin, I thank you for always being so loving and proud of my accomplishments and for always making me feel like I am in the right place. Thank you for putting up with my long work hours and travel, and for cooking me warm delicious meals when I was overwhelmed. I am excited for our next adventures together!

I would also like to thank my advisor Jolie Cizewski, for her guidance and support, and for providing me with so many opportunities through conferences and experiments that strengthened me as a nuclear physicist, and for making sure everyone knows that a photo will always be better when I am in it.

Thanks to Steve Pain, the nuclear experiment Jedi who took me on as a young Padawan, helping me learn the critical experiment techniques in over drive by staying up days at a time to get ready for beam time, and for understanding that hard work goes hand in hand with craft beer.

Thanks to Kelly Chipps for keeping the Oak Ridge astro group thriving through the difficult changes in the physics division over the years, making our small group feel like a physics family.

Thanks to Mike Febbraro for teaching me organic chemistry and helping me realize

that many aspects of this career are really just "Mickey Mouse". I enjoyed helping to turn your crazy ideas into reality.

Also thanks to Harry Sims for the hard work with the preliminary (and continued) analysis of the $d(^{84}\mathrm{Se},p)$ experiment, and for being such a great friend and colleague throughout my graduate career.

The experiments in this dissertation would not be possible without Tony Ahn "the ASICs king", Jorge Pereira, Ron Fox, Jeromy Tompkins, Giordano Cerizza, Andrew Ratkiewicz, Cory Thornsberry, Brett Manning, Travis Baugher, Alex Lepailleur, Robert Varner, Mike Famiano, Tom Ginter and also Filomena Nunes for telling us experimentalists what to measure.

Dedication

For my two brothers

"It's a seven story mountain. It's a long, long life ahead. Got to find a voice and fill my throat again."

- Railroad Earth

Table of Contents

List of Tables

List of Figures

Chapter 1

Introduction

The composition of elements in our universe is an extraordinary puzzle that we are only recently beginning to understand. A harmonious mixture of astronomy, astrophysics, and nuclear physics is imperative to reveal the intricacies of how the elements were formed in the cosmos. Recently, our understanding of the origin of heavy elements has deepened with the observation of gravitational waves in coincidence with photons created by the merger of two neutron stars [Abb17]. This fantastic observation has pinpointed a dominant site of the rapid neutron capture process (r-process) [Kas17], where nuclei capture neutrons more rapidly than they β-decay back to stability. The rapid neutron capture process is the mechanism responsible for the creation of about half of the elements heavier than iron [Arn07]. The r-process has been theorized to occur in neutron star mergers and also supernovae, where there is a very high neutron density ($>10^{20}$ neutrons/cm^3) and high temperatures ($>10^9$ K).

One of the greatest challenges in understanding r-process nucleosynthesis is that the relevant nuclei are very neutron rich and short lived. Modern accelerator facilities are now able to produce radioactive ion beams (RIBs) with sufficient intensities to make measurements on some of these exotic nuclei, although the ability to produce particle beams close to the neutron drip line for the heavier elements is still out of reach. To extract spectroscopic information on unstable nuclei, such reactions can be performed in inverse kinematics with beams of rare isotopes and light mass targets. Single-nucleon transfer reactions such as (d, p), (p, d) or (d, n) are beneficial reactions to study the single-particle structure of nuclei [Sat83; Aus70].

The extracted spectroscopic properties can be used to constrain nuclear structure models, and therefore improve their reliability when predicting properties of nuclei further from stability. In addition, the measured spectroscopic factors are important in calculating the direct-semidirect (DSD) component of neutron capture needed to understand observed r-process abundances [Koz12].

Recent r-process network calculations [Sur14; Mum16] have highlighted the need to obtain better measurements of nuclear properties such as masses, half lives and neutron capture rates to understand the observed r-process elemental abundances. In particular, such studies have recognized that neutron capture at late times in an r-process event, when the neutron densities and/or temperatures are below the maximal values, can significantly affect the predictions of final abundances. Nuclei near the peaks in r-process abundances have closed shells of neutrons where the level densities are low and neutron capture is dominated by direct processes. These are sensitive to the detailed spectroscopic properties of low-excitation, low-spin states; therefore, it is crucial to accurately measure the properties of neutron-rich nuclei near closed shells and near the r-process waiting points.

1.1   Background

The creation of heavy elements occurs in the cosmos due to nuclear processes such as fusion, fission, decay, and a variety of other reactions. Nuclear fusion occurs in the core region of the stars and is responsible for the creation of many of the heavier elements up to iron (A = 56). The fusion process can only synthesize elements up to iron because of binding energy, which is the energy required to hold a nucleus together given by the mass difference as shown in eq. 1.1.

$$B(A,Z) \ = \ (Zm_p + Nm_n - m_{A,Z})c^2 \tag{1.1}$$

where A is the total number of nucleons, Z is the number of protons, $m_{A,Z}$ is the rest mass, and m_p and m_n are the masses of the proton and neutron, respectively. The nuclear binding energy per nucleon (Fig. 1.1) is peaked at the most tightly bound nuclei (*e.g.* Fe); therefore it is energetically unfavorable to produce elements heavier than iron in the fusion process.
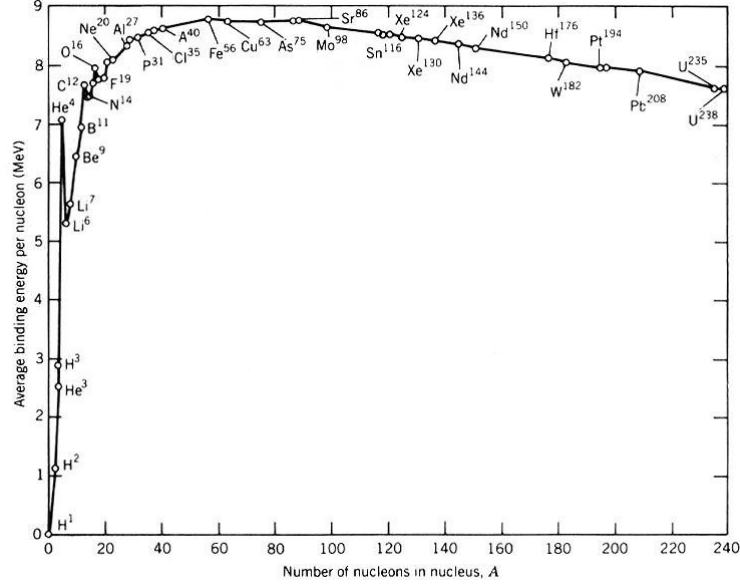
Figure 1.1: Binding energy per nucleon for stable nuclei. Figure adopted from Ref. [Bin18]

Elements heavier than iron are created by many different processes, with the most productive being the s-process and r-process. Each process creates elements along a path on the nuclear chart as shown in Fig. 1.2. The s-process or slow neutron capture process follows a path close to the stable nuclei and occurs in Asymptotic Giant Branch (AGB) stars. The neutron capture occurs at a rate that is comparable to or longer than the β-decay rate, so the nuclei have enough time to decay back to stability before increasing in mass with an additional neutron capture. Of particular interest is the rapid neutron capture process or r-process. Unlike the s-process, the r-process occurs where there is an abundance of neutrons that can create heavier neutron-rich nuclei through capture reactions on a faster time scale than that of β decay. All of the

processes of nucleosynthesis are limited in the heavy mass region (A<200) because of competition with α-decay and fission.
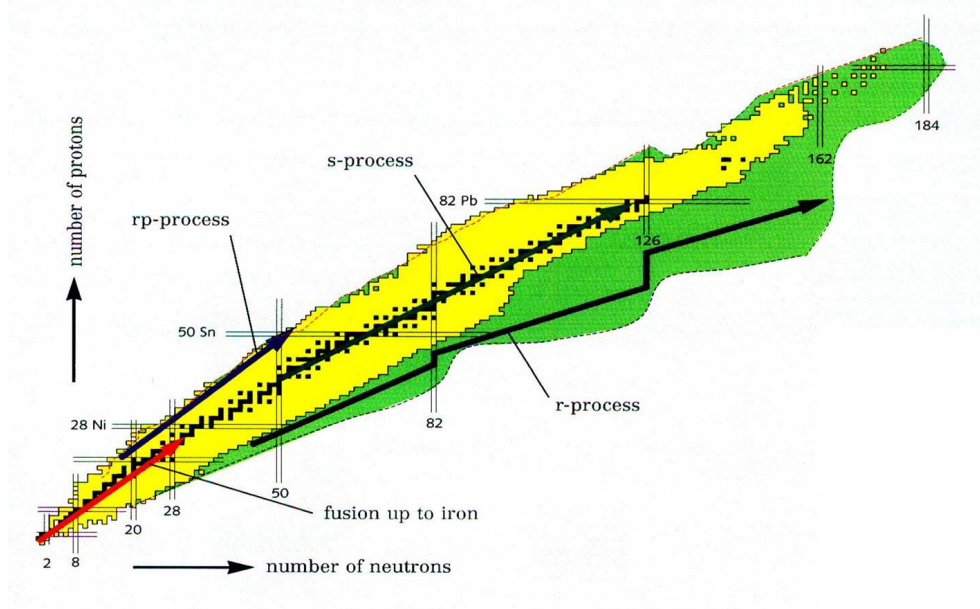
Figure 1.2: Chart of nuclei showing the stable elements in solid black squares, unstable elements in yellow, and an unknown region in green. The rapid neutron capture process path is the lower black line labeled r-process. Figure adopted from Ref. [Nuc18]

The nuclear properties of neutron-rich nuclei are not well understood because of the extremely limited experimental data in this exotic region. There are still many open questions in nuclear physics including defining the limits of nuclear stability to determine which combinations of neutrons and protons can be bound to form a nucleus, and also how the shell structure of the nucleus evolves in the exotic, neutron-rich region. This unknown region of nuclei is a very large portion of the chart of nuclei, shown in green in Figure 1.2. Experimentalists are limited by the facilities that are capable of producing these neutron-rich isotopes, but new facilities such as the Facility for Rare Isotope Beams (FRIB) [Gad14] will help extend our understanding in this unknown region of isotopes.

1.2   Nuclear structure

Distinct patterns emerge as we look deep into the atomic nucleus. As fermions, protons and neutrons obey the Pauli principle and have a characteristic way of ordering themselves into configurations that are similar to the atomic shell structure. Research suggests that distinct patterns, such as "magic numbers" arise because of nuclear shell closures that are due to clustering of energy levels, locations of which require inclusion of spin-orbit forces [May48; May49; Hax49]. This shell model of the nucleus has been very successful to describe the behavior of nuclei near stability, and continues to serve as a basis as we discover more about nuclei further from stability.

The shell model predicts single-particle energy levels that are the basis states of a given potential. Choosing a flat or modified harmonic oscillator potential, the single-particle state solutions emerge, split in energy by their angular momentum. Accounting for spin-orbit interactions, we are left with a shell structure as shown in Fig. 1.3. This shell model predicts large gaps between certain energy levels, which are referred to as shell closures or "magic numbers" of nucleons.

A more realistic choice of mean field potential to describe the nucleus and build the single-particle states is the Woods-Saxon potential, which is given by,

$$V(r) = -\frac{V_0}{1 - exp(\frac{r-R}{a})} \tag{1.2}$$

$$R = r_0 A^{1/3} \tag{1.3}$$

where V_0 is the potential well depth, a is the diffuseness or surface thickness with a typical value of $a = 0.65\ fm$, R is the nuclear radius defined in eq. 1.3 with a typical value r_0=1.25 fm, and A is the total number of nucleons [Tho09]. The nuclear radius is proportional to the size of the nucleus and is defined as a type of interaction length rather than a classical radius.
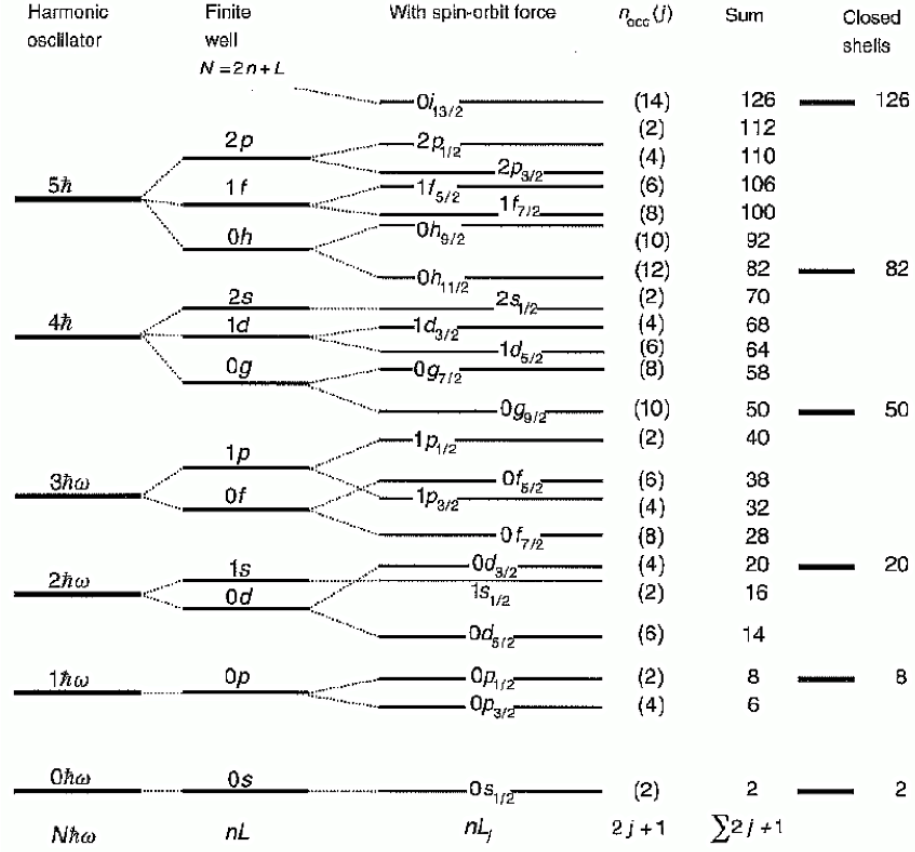
Figure 1.3: Single-particle levels as the basis states for the shell model around the valley of stability. Harmonic oscillator states split into defined closed shells by adding spin orbit interactions. Figure adopted from Ref. [Tho09]

The structure of nuclei far from stability is of particular interest in this work because the evolution of the nuclear shell structure is not well understood in this region. It is advantageous to start to benchmark the evolution of shell structure near closed shells, such as N=50, because the excitations above this shell closure are expected to be single-particle configurations rather than more complicated configurations due to the shell closure acting as an inert core. It is clear from the N=51 isotones, shown in Fig. 1.4, that the shell structure is drastically changing with an increasing imbalance of neutrons and protons in the nucleus.
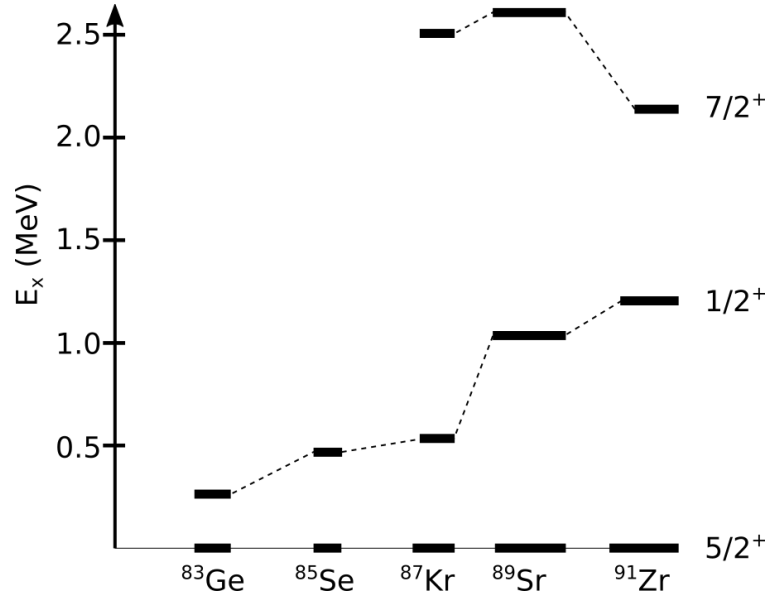
Figure 1.4: Spectroscopic properties of some low lying states of the even Z, N=51 isotones. Lengths of the lines represent approximate spectroscopic factors. Data taken from: ^{83}Ge and ^{85}Se [Tho07], ^{87}Kr [Har70], ^{89}Sr [Cle78], ^{91}Zr [Rat73]

Although some of the energy levels have been measured and some of the spin-parities have been assigned for these levels, their spectroscopic strengths are largely unknown. The spectroscopic factor (S) is a measure of this spectroscopic strength, which informs how much a nuclear state resembles a single-particle excitation. The single-particle structure of these nuclei, specifically near shell-closures, are important quantities to help constrain theoretical structure models. Systematic studies in this region are helpful to constrain theoretical models and help inform extrapolations of

the theory to nuclei that are currently unreachable experimentally. Transfer reaction measurements on nuclei near closed shells are well suited to extract the location and fragmentation of the single-particle strengths.

1.3 The r-process

In the rapid neutron capture process, neutron capture (n, γ) and photo-disintegration (γ, n) occur on a much faster time scale than β-decay. This equilibrium between (n, γ) and (γ, n) determines the abundances along an isotopic chain [Qia03]. The r-process has to wait for a nucleus within this equilibrium to β-decay in order to build up heavier nuclei and establish $(n, \gamma) \rightleftharpoons (\gamma, n)$ equilibrium in a new isotopic chain. These are referred to as waiting points and are usually nuclei near closed neutron shells, where the neutron separation energy falls off drastically with increasing neutron number. Eventually, the r-process will "freeze out" when there is not an abundance of neutrons and the temperatures are sub-optimal. The remaining isotopes eventually decay back to stability creating isotopic abundances as shown in Fig. 1.5, where these r-process elemental abundances have been observed for many metal-poor stars (*e.g.* Refs. [Cow99; Hon04]).

Interestingly, the waiting points near nuclear shell closures are directly correlated with the peaks in observed r-process abundances at A~80, A~130, and A~195 corresponding to neutron shell closures N=50, N=80, and N=126, respectively. Fig. 1.5 also shows final abundances predicted by theoretical r-process models. These models involve full network calculations that constitute a large number of unstable nuclei, some of which have yet to be observed. Therefore, assumptions have to be made where data is unavailable based on theoretical predictions and observed trends in neutron-rich nuclei.

There are large discrepancies between the theoretical calculation and observation
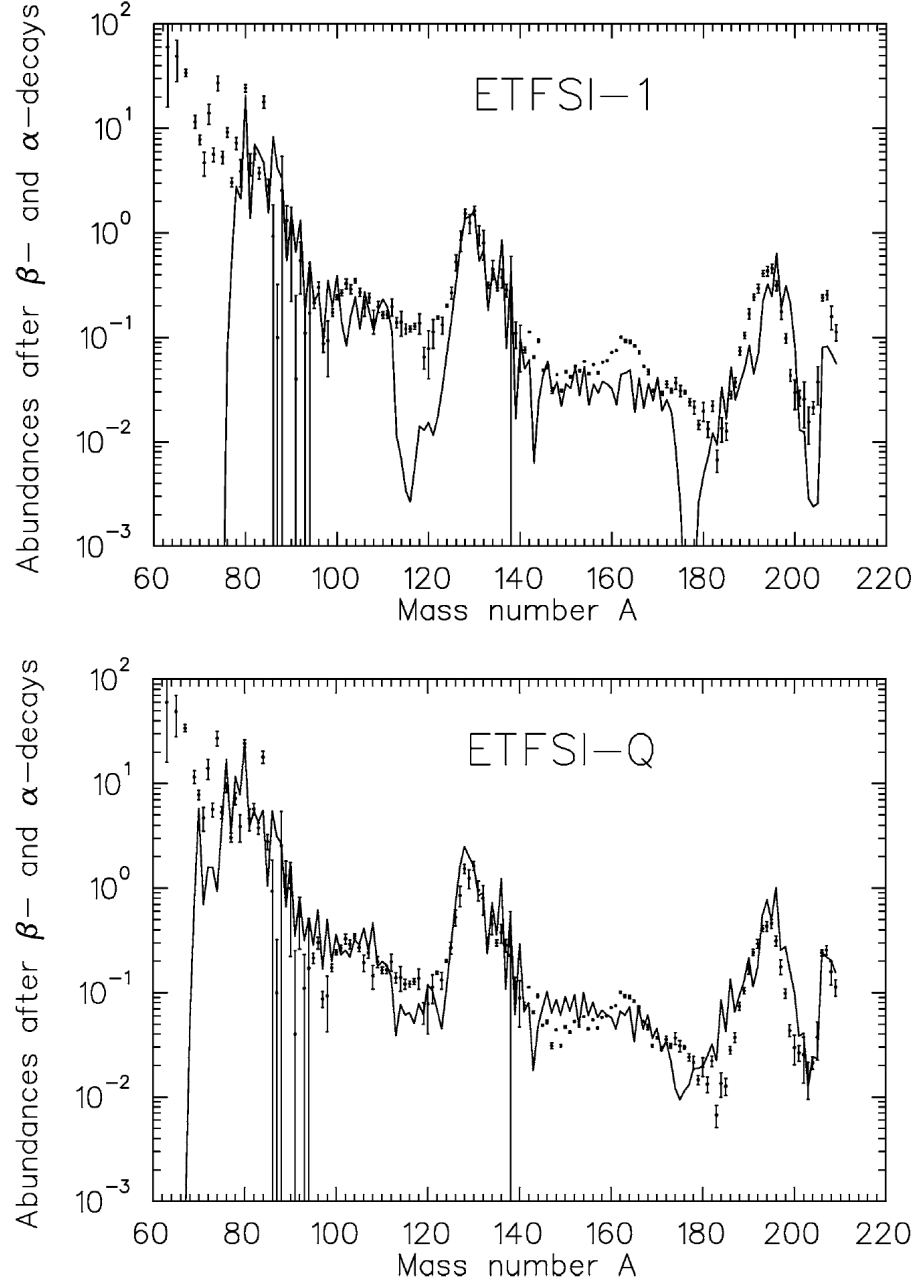
Figure 1.5: Theoretical predictions (lines) for the observed r-process solar abundances (points) for a pronounced shell structure (ETFSI-1 [Abo95]) and a quenched shell structure (ETFSI-Q [Pea96]). Figure adopted from Ref. [Pfe01]

that arise when predicting elemental abundances if a pronounced shell structure is assumed similar to the levels in Fig. 1.3, which is the ETFSI-1 mass model [Abo95]. A different mass model based on the assumption that the shell structure is quenched (ETFSI-Q [Pea96]) is able to better represent the observation compared to the pronounced shell structure; however, does not accurately represent the peak at mass A=80. A schematic showing the differences between the pronounced and quenched (diffuse) shell structures is shown in Fig. 1.6. Although the quenched shell structure more accurately represents the observed r-process abundances than the pronounced shell structure, the theoretical models could be better constrained from experiment, especially in the vicinity of closed neutron shells.
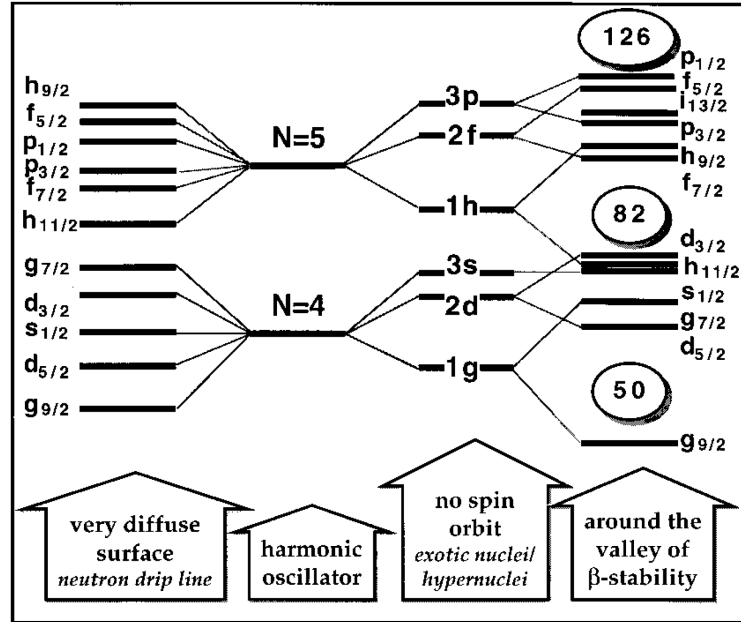
Figure 1.6: Different single-particle levels for a chosen potential, showing the differences between a quenched mass model (diffuse surface) and a pronounced shell model around the valley of β-stability. Figure adopted from Ref. [Dob96]

Network calculations to reproduce the observed r-process abundances are sensitive to the nuclear physics inputs such as nuclear masses, β-decay rates and neutron capture rates. Studies have shown that a small variation in the neutron capture rates, especially at waiting points, can greatly affect the final composition of elements

that were formed in this process [Sur09; Sur14; Mum16]; therefore, it is important to understand the underlying nuclear physics at these particular points in the r-process path. The specific region of focus in this research is the shell closure at neutron number equal to 50, which has been shown to be a very important region of the nuclear chart for predicting final abundances of nuclei relevant to the so-called "weak" r-process [Sur14]. Although neutron capture is difficult, if not impossible to measure on very short-lived nuclei in a laboratory, neutron transfer reactions, such as (d, p), can be very useful in this sense to provide information such as spectroscopic factors to infer direct neutron capture rates for neutron-rich nuclei.

There are three major mechanisms for neutron capture, which include compound nuclear, direct, and semidirect [Chi08]. Typically compound nuclear capture (CN) is the dominant mechanism which involves the formation of a highly-excited unbound system described as a statistical process through a high density of states [Hau52]. In neutron-rich nuclei, the neutron separation energy is much lower than in nuclei near stability causing nuclear level density to diminish. The low level density causes the direct capture processes to dominate which populates these discrete bound states. This takeover of direct capture from statistical Hauser-Feshbach (HF) models [Hau52] describing compound capture is made clear in the tin isotopes around doubly magic ^{132}Sn shown in Fig. 1.7.

The direct neutron capture process is the dominant process for nuclei near closed shells and is sensitive to the excitation energies, spins, parities, electromagnetic transition probabilities, and single-particle spectroscopic factors [Kra96; Rau98]. Most of these parameters necessary to infer neutron capture rates can be extracted experimentally through (d, p) reaction measurements, especially for the low-lying, low-spin states. Therefore, experimental data from (d, p) reaction measurements are necessary to constrain these theoretical models to strengthen their predictive power toward the unfamiliar regions of the nuclear landscape.
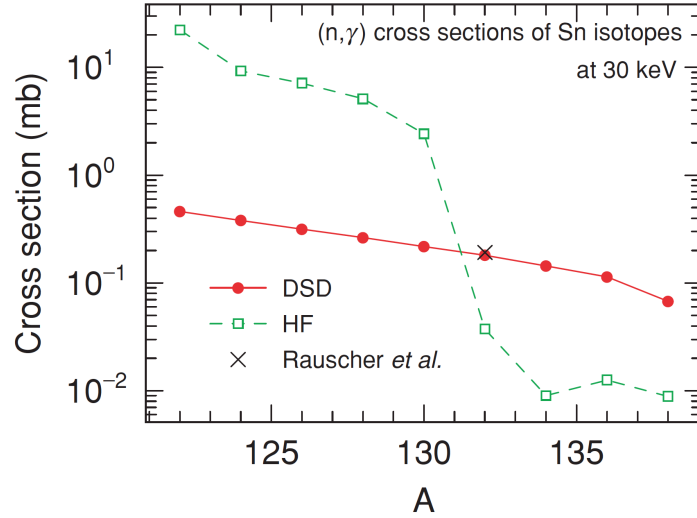
Figure 1.7: Calculated neutron capture cross sections for direct-semidirect (DSD) and compound (HF) capture for the Sn isotopes near doubly magic ^{132}Sn. Point by Rauscher *et al.* [Rau98] is best estimate for direct (n, γ) cross section of ^{132}Sn. Figure adopted from Ref. [Chi08]

1.4 Goals of this study

The goal of this research is to investigate new methods for single-particle transfer reactions using fast beams ($\sim$40 MeV/u) to extract spectroscopic information for nuclei far from stability. As more exotic nuclei become available with new radioactive ion beam facilities, it is important to develop new experimental techniques for precision measurements to strengthen theoretical predictions.

The focus of this work is in using combined measurements of neutron transfer reactions at two different energies to provide a constraint on the final bound-state potential and, therefore, constrain spectroscopic factors for low-lying states in neutron-rich nuclei relevant to r-process nucleosynthesis. The neutron bound-state potential can be constrained by extracting previously undetermined single-particle asymptotic normalization coefficients by combining transfer reaction measurements at different beam energies. The single-particle normalization coefficients are properties of the

shape of the bound-state potential, which is largely unknown in nuclei far from stability and also for many stable nuclei. The spectroscopic factor is a measure of the single-particle nature of a nuclear state and is heavily dependent on the single-particle ANC; therefore, by constraining the single-particle ANC, the spectroscopic factor is also constrained. This method will help inform theoretical models for predicting properties of neutron-rich nuclei. Although this method has been addressed previously (*e.g.* [McC14; Muk08]), there is still an open question as to whether this method is valid, and in which mass regions (see Section 2.3.1).

The majority of this work is focused on the stable beam experiment studying the ^{86}Kr$(d, p)^{87}$Kr reaction as a proof of principle for the combined measurement method in this mass region. There are many experimental challenges that arise as the nuclei of interest are more neutron rich, such as low beam rates, low purities, and inverse kinematics. In order to mimic the conditions of a radioactive ion beam, the ^{86}Kr(d, p) reaction was performed in inverse kinematics with a beam of ^{86}Kr impinging on a deuterated polyethylene target. The incident beam was also attenuated to rates that are similar to radioactive ion beams ($< 10^6$ pps), rather than the typical high intensities of stable beams ($\sim 10^8$ pps). Neutron transfer reactions are traditionally performed at beam energies less than $\sim$15 MeV/u. The combined method requires these measurements to also be performed at $>$30 MeV/u, which brings new experimental challenges. Another goal of this research is to address some of the required experimental techniques needed to do spectroscopy on neutron-rich nuclei with fast beams in inverse kinematics. These new techniques were recently implemented in the radioactive ion beam experiment to study the ^{84}Se$(d, p)^{85}$Se reaction, with preliminary results presented in this work.

1.5 Structure of the dissertation

The structure of the dissertation is as follows:

Chapter 2 provides an introduction to the theoretical formalism used to extract spectroscopic information from reactions on atomic nuclei. This chapter provides information about the optical model approach to deuteron stripping reactions and experimentally extracting spectrosopic factors.

Chapter 3 gives an overview of the experimental components necessary to measure single-particle transfer reactions, including the radioactive ion beam production, targets and different types of radiation detectors.

Chapter 4 describes the details of the d(^{86}Kr,p)^{87}Kr experiment at 35 MeV/u and also the results from the combined analysis of the transfer reaction for constraining the bound state potential in ^{87}Kr.

Chapter 5 details the experiment preparation and design of the d(^{84}Se,p)^{85}Se at 45 MeV/u. Preliminary results for the ^{84}Se neutron transfer reaction at 45 MeV/u are presented. Also included in this chapter is a re-analysis of the previously published low-energy measurement to extract the ANC within the adiabatic wave approximation.

In chapter 6, the results and outcomes from this dissertation are summarized. Also presented in this chapter is an outlook to future methods using transfer reactions with fast radioactive ion beams.

Chapter 2

Theory

Single-particle transfer reactions provide a way to extract spectroscopic information on exotic nuclei. However, the experimental measurement requires a theoretical interpretation in order to assign spins and parities and spectroscopic strengths to the states observed in an experiment. This chapter provides an overview of the relevant components in the nuclear reaction formalism needed to interpret these experimental results.

2.1 Reaction Theory

The theory of direct reactions aims to describe a given process when two particles collide. Although there are many different outcomes from this process, the focus in this work is when there are two particles in the entrance channel and two particles in the exit channel. The standard notation for nuclear reactions is $A(a, b)B$, where A is the target, a is the projectile, B is the recoil, and b is the ejectile. The entrance channel refers to $A + a$ and the exit channel refers to $B + b$, where the particles may populate different configurations of excited states; one possible exit channel being elastic scattering.

2.1.1 Overview of direct reaction theory

The entrance and exit channels are described as waves scattered by a nuclear potential. The interaction potential for a reaction such as $A(a, b)B$, can be split into two parts,

$V(r) = V_1(r) + V_2(r)$, where $V_1(r)$ is the distorting potential that describes the elastic scattering channel and is used to generate the distorted waves through the Schrödinger equation. $V_2(r)$ is the interaction of interest with a relatively small effect, treated as a perturbation to the original solution with $V_1(r)$. This is the essence of the Distorted Wave Born Approximation (DWBA), where the dominant interaction is the elastic scattering and the perturbation is truncated to linear order in $V_2(r)$. The transition amplitude for this reaction that describes the inelastic channel has the form shown in eq. 2.1.

$$T_{DWBA} = \iint \chi_f^{(-)}(\mathbf{k}_f, \mathbf{r}_f)^* \langle b, B|V_2|a, A\rangle \chi_i^{(+)}(\mathbf{k}_i, \mathbf{r}_i) d^3 r_i d^3 r_f \qquad (2.1)$$

where $\chi^{(\pm)}$ are the incoming and outgoing distorted waves, i and f are the entrance (incoming) and exit (final) channels, respectively, and V_2 is the interaction potential that causes the non-elastic transitions, the form of which is dependent on the type of reaction and the model chosen to describe it [Sat83]. The choice of V_2 is important because the differential cross section, $\frac{d\sigma}{d\Omega}$ (see eq 2.2), is proportional to the square of the transition amplitude, $|T_{DWBA}|^2$. The differential cross section is calculated for a given channel (i) from experimental observables by eq. 2.2,

$$\frac{d\sigma_i}{d\Omega} = \frac{N_i}{I_0 \ n \ \Delta\Omega} \qquad (2.2)$$

where N_i is the number of scattered particles from a given channel i, I_0 is the incident flux of beam particles, n is the number density of target particles that overlap with the incident beam, and $\Delta\Omega$ is the solid angle the particles scatter into [Sat83].

2.1.2 Optical Model

The choice of interaction potential between target and projectile has to not only model the small contributions from inelastic scattering, but also the large contribution from

elastic scattering. These potentials are usually chosen to be optical model potentials, which account for the elastic scattering in a general way in the presence of absorptive effects. These types of potentials are constructed to simplify the complicated many-body interactions of every nucleon in colliding nuclei. The optical model washes out the many-body degrees of freedom in a nucleus and replaces the nucleus with a mean field plus any valence nucleons relevant to the reaction, which is shown pictorially in Fig. 2.1.
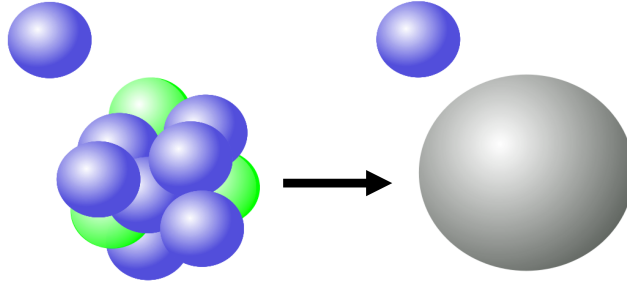
Figure 2.1: Internal nucleon degrees of freedom are replaced by a mean field in the optical model

This simplification of the complicated many-body problem comes with a price. The real interaction potential picks up a complex component in order to account for absorption, which is represented in a general form in eq. 2.3,

$$U(r) = V(r) + iW(r) \tag{2.3}$$

where $V(r)$ and $W(r)$ are real functions that give the potential the correct radial dependence. The real part of eq. 2.3, $V(r)$, describes the elastic scattering and the imaginary part, $W(r)$, describes the absorption [Kra98]. As shown in eq. 2.4, a full form of the optical model potential includes Coulomb (V_c), volume (V), spin-orbit (V_{so}), imaginary volume (W), and imaginary surface terms (W_D) [Per76].

$$U(r) = V_c - V f(x_0) + \left(\frac{\hbar}{m_\pi c}\right)^2 V_{so}(\sigma \cdot \ell)\frac{1}{r}\frac{d}{dr}f(x_{so})$$

$$- i[(W f(x_W) - 4W_D\frac{d}{dx_D}f(x_D)] \quad (2.4)$$

where,

$$V_c = ZZ'e^2/r, \quad \text{for} \quad r \geq R_c$$

$$= (ZZ'e^2/2R_c)(3 - r^2/R_c^2) \quad \text{for} \quad r < R_c$$

$$R_c = r_c A^{1/3}$$

$$f(x_i) = (1 + e^{x_i})^{-1} \quad \text{where} \quad x_i = (r - r_i A^{1/3})/a_i$$

Typically, the form of each potential used is a Woods-Saxon shape given by eq. 1.2 and by $f(x_i)$ in eq. 2.4. The constants (*e.g.* V, r_i, a_i) are adjusted to fit elastic scattering data on a given nucleus. Large sets of elastic scattering data that have been compiled for particular mass and energy ranges, are used to deduce global optical model parameterizations (*e.g.* [Var91; Dae80; Loh74; Men71; Kon03]). Example sets of parameters for the entrance and exit channels are shown in Tables 2.1 and 2.2 respectively. These global sets can be extrapolated for potentials of nuclei where elastic scattering has not been measured. Global sets are also very useful because the multi-parameter fit to elastic scattering on a single nucleus may have multiple χ^2 minima, and the larger sets of data reduces the chances of large variations in potential parameters. The main optical model parameterization used in this study is that of Koning-Delaroche [Kon03] shown in Table 2.3 using an adiabatic treatment as discussed in section 2.1.3. These phenomenological optical model potentials are based on elastic scattering of protons and neutrons with incident energies from 1 keV to 200 MeV and for a mass range of 24 $\leq$A$\leq$209.

Table 2.1: Example global optical model parameterizations for incoming deuteron channel (^{86}Kr $+ d$) of the ^{86}Kr$(d,p)^{87}$Kr ground state reaction

	V [MeV]	r_0 [fm]	a_0 [fm]	W [MeV]	r_W [fm]	a_W [fm]	W_s [MeV]	r_{ws} [fm]	a_{ws} [fm]	V_{so} [MeV]	r_{so} [fm]	a_{so} [fm]	W_{so} [MeV]	r_{soi} [fm]	a_{soi} [fm]
[Dae80]	92.817	1.170	0.728	0.150	1.325	0.799	12.336	1.325	0.799	3.506	1.070	0.660	0.000	1.000	1.000
[Loh74]	109.073	1.050	0.860	0.000	1.430	0.753	11.189	1.430	0.753	3.500	0.75	0.500	0.000	1.000	1.000

Table 2.2: Example global optical model parameterizations for outgoing proton channel (^{87}Kr $+ p$) of the ^{86}Kr$(d,p)^{87}$Kr ground state reaction

	V [MeV]	r_0 [fm]	a_0 [fm]	W [MeV]	r_W [fm]	a_W [fm]	W_s [MeV]	r_{ws} [fm]	a_{ws} [fm]	V_{so} [MeV]	r_{so} [fm]	a_{so} [fm]	W_{so} [MeV]	r_{soi} [fm]	a_{soi} [fm]
[Var91]	54.229	1.200	0.690	0.935	1.235	0.690	9.286	1.235	0.690	5.900	1.069	0.630	0.000	1.000	1.000
[Kon03]	56.244	1.212	0.665	1.025	1.212	0.665	9.128	1.272	0.564	5.676	1.039	0.590	-0.055	1.039	0.590

Table 2.3: Koning-Delaroche global optical model parameters [Kon03] used for the exit channel for the ground state reaction of ^{86}Kr$(d,p)^{87}$Kr and to construct the adiabatic potentials for the deuteron using the adiabatic treatment of Johnson-Tandy [Joh74] as discussed in section 2.1.3

	V [MeV]	r_0 [fm]	a_0 [fm]	W [MeV]	r_W [fm]	a_W [fm]	W_s [MeV]	r_{ws} [fm]	a_{ws} [fm]	V_{so} [MeV]	r_{so} [fm]	a_{so} [fm]	W_{so} [MeV]	r_{soi} [fm]	a_{soi} [fm]
n	39.467	1.212	0.665	2.924	1.212	0.665	4.987	1.272	0.530	5.224	1.039	0.590	-0.200	1.039	0.590
p	48.423	1.212	0.665	3.103	1.212	0.665	7.156	1.272	0.563	5.262	1.039	0.590	-0.184	1.039	0.590
^{87}Kr+p	36.055	1.212	0.665	7.288	1.212	0.665	3.514	1.272	0.564	4.566	1.039	0.590	-0.568	1.039	0.590

2.1.3   Adiabatic Wave Approximation

In a traditional DWBA approach describing the single-particle transfer process, the deuteron is treated as a single wavefunction in the interaction. However, since the deuteron is weakly bound (2.2 MeV), the breakup should be treated as an intermediate step in the transfer process, especially at higher beam energies (*e.g.* >10 MeV). An adiabatic model to treat the breakup of the deuteron was introduced by Johnson and Soper [Joh70], where the wavefunction for the deuteron-target system is split into a three-body wave function for the neutron, proton and target nucleus. A new distorting optical potential can then be used as the sum of the neutron-target and proton-target optical potentials, where this is referred to as the adiabatic potential. Johnson and Soper proposed a zero-range version of the ADiabatic Wave Approximation (ADWA) formalism for deuteron-induced stripping reactions. This approximation assumes that the relative distance between the proton and neutron is zero ($\mathbf{r} = r_p - r_n = 0$), which means they are at the same coordinate relative to the center of mass of the target-nucleus system ($R = \frac{1}{2}(r_n + r_p) \neq 0$), and do not separate in the time it takes the deuteron to transit the nucleus. For example, the (d, p) stripping amplitude is given by,

$$T_{d,p} = \langle \chi_p^{(-)} \, \Phi_n | V_{np} | \Psi^{ad}(\mathbf{r}, R) \rangle \tag{2.5}$$

where, Φ_n is the neutron-core bound state wave function, $\chi_p^{(-)}$ is the outgoing proton distorted wave, V_{np} is the neutron-proton interaction potential, and $\Psi^{ad}(\mathbf{r}, R)$ is the three-body wave function representing the n+p+A system assuming A is in its ground state [Ngu10; Pan13]. The zero-range version of ADWA is then solved in the limit that the proton and neutron potentials are at the same location, which is contained in the three body wave function $\Psi^{ad}(0, R)$. This assumption is based on the the short range nature of V_{np} which reduces the calculation to an effective two-body

problem.

A finite-range version of the adiabatic model was proposed by Johnson and Tandy [Joh74], where the sum of the potentials is averaged over the neutron-proton inter-action, and the n-p spectrum is discretized by expanding Ψ^{ad} in terms of discrete n-p states represented by a complete set of Weinberg eigenstates. The Weinberg states are chosen as a basis because they form a complete set of functions of r within the range of V_{np} [Lai93; Pan13]. The Finite-Range ADiabatic Wave Approximation (FR-ADWA) potential is then defined by,

$$V_{FR-ADWA} = \frac{\langle \phi_d | V_{np}(V_n + V_p) | \phi_d \rangle}{\langle \phi_d | V_{np} | \phi_d \rangle} \tag{2.6}$$

where V_p and V_n are the respective nucleon-core potentials [Ngu10]. This transfer process is shown pictorially in Fig. 2.2.
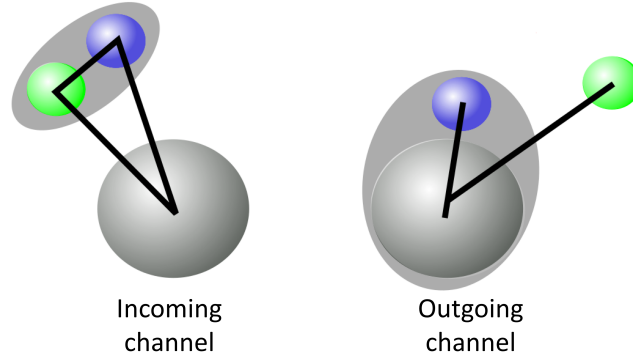
Figure 2.2: Representation of the incoming and outgoing channels of the neutron transfer reaction (d, p).

2.2 Asymptotic normalization coefficients and spectroscopic factors

The bound-state potential is also modeled by a Woods-Saxon shape, where the well depth is adjusted to reproduce the measured binding energy of the transferred particle.

The radius and diffuseness parameters, r_0 and a, are chosen based on the bound-state configurations of stable isotopes, unless more information is known about the shape of the bound-state potential. The bound-state potential is used to generate single-particle wave functions as shown in Figure 2.3. A small change in the radius parameter, r_0, while the diffuseness, a, remains constant will change the geometry of the Woods-Saxon potential, which also affects the single-particle wave function.
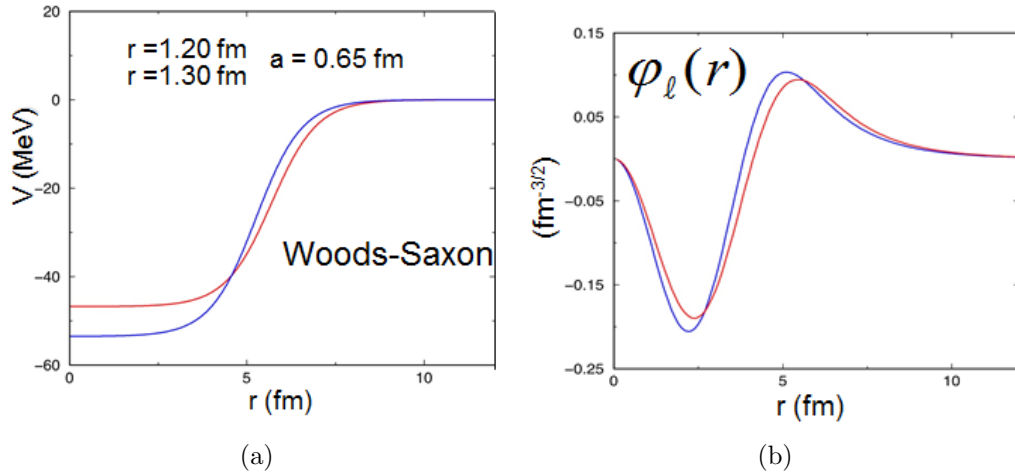
Figure 2.3: (a) Woods-Saxon potential as a function of radius for a fixed diffuseness of a=0.65 and two values for r_0. (b) Generated single-particle wave functions as a function of radius from the Woods-Saxon potentials in (a).

Asymptotic normalization coefficients (ANCs) are used to describe the amplitude of the tail of a wave function, either the single-particle wave function or the nuclear many-body wave function. These coefficients are an important quantity since they describe the peripheral region of a nucleus, which is the region where a nucleon would be interacting in a low-energy transfer reaction. The single-particle ANC ($b_{\ell j}$), defines the amplitude of the tail of the single-particle wave function, and its value depends on the shape of the potential, as shown in Figure 2.3. The asymptotic region is of interest because direct reactions, such as transfer, are peripheral reactions that proceed mainly through the tail of the wavefunction. Also, the interior of the many-body wave function is drastically different from the interior portion of the

single-particle wave function, making it complicated to compare the two. In contrast, their radial dependence is similar in the asymptotic region and differs only by a normalization factor. The asymptotic region of both the single-particle wave function and nuclear many-body wave function can be described by well known spherical Hankel functions, $h_\ell(ikr)$, as shown in Figure 2.4.
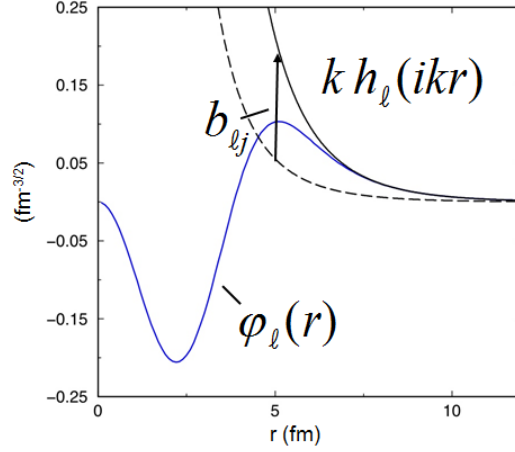
Figure 2.4: The single-particle wave function (blue) represented by a spherical Hankel function (dashed), normalized by the single-particle ANC (solid).

Single-particle states can be characterized by ANCs in the asymptotic region of the nucleus. However, nuclear states usually have more complicated wavefunctions because states with similar spins and parities can mix as the single-particle structure can be fragmented. The spectroscopic factor, S, is used to quantify the fragmentation of single-particle strength in a particular state. In transfer reactions, S by definition is the square of the norm of the overlap function between a bound state nucleus and a two body channel of a nucleus plus a nucleon [Muk01]. For the reaction $A(a,b)B$, the overlap function is defined by,

$$\phi_{A\ell j}^B = \langle \phi_{\ell j}^A(\xi_A) | \phi_{\ell j}^B(\xi_A, \mathbf{r}) \rangle \qquad (2.7)$$

where $\phi_{\ell j}^A(\xi_A)$ is the wave function of the core, $\phi_{\ell j}^B(\xi_A, \mathbf{r})$ is the composite core + particle wave function, ξ_A refers to the internal A coordinates, and $(\xi_A, \mathbf{r})$ is the

composite core + particle coordinates [Tho09]. The spectroscopic factor is a measure of the single-particle strength in a nuclear state. Its value determines how much the composite nucleus looks like a core + particle. S equal to unity would mean the nucleus has a pure single-particle configuration. A spectroscopic factor much less than unity would indicate heavy fragmentation of the single-particle strength. The definition of the spectroscopic factor used in this study is given by the normalization of the overlap function (eq. 2.7), which can be written as the sum of spectroscopic amplitudes times the normalized single-particle wave functions given by,

$$\phi_{A\ell j}^{B} = \sum_{\ell j} A_{\ell j} \varphi_{A\ell j}^{B} \tag{2.8}$$

where $\varphi_{A\ell j}^{B}$ is a single-particle wave function. The amplitude, $A_{\ell j}$, defines the spectroscopic factor by the following equation [Tho09].

$$S_{\ell j}^{A.B} = |A_{\ell j}|^2 \tag{2.9}$$

This quantity is not an observable, but we can use approximations in the radial asymptotic region to infer the value of this amplitude using experimental values. In the asymptotic region, the overlap function, $\phi_{A\ell j}^{B}$, for a single neutron transfer can be expressed by the following Hankel functions,

$$\phi_{A\ell j}^{B} \rightarrow C_{\ell j} k h_\ell(ikr) = S_{\ell j}^{1/2} b_{\ell j} k h_\ell(ikr) \tag{2.10}$$

where the left hand side is the nuclear many-body wave function, and the right hand side is the single-particle wave function, and $C_{\ell j}$ and $b_{\ell j}$ are the respective normalization coefficients [Muk05]. This can be a good assumption for the asymptotic region, but does not guarantee the correct form of $\phi_{A\ell j}^{B}$ in the interior region of the nucleus. The spectroscopic factor can be defined (using eq. 2.10) in the asymptotic region as the ratio between the nuclear ANC, $C_{\ell j}$ and the single-particle ANC, $b_{\ell j}$,

given by,

$$S_{\ell j} \;=\; \frac{C_{\ell j}^2}{b_{\ell j}^2} \tag{2.11}$$

where the nuclear ANC can be extracted experimentally from a peripheral reaction, but the single-particle ANC cannot [Muk05]. The single-particle ANC is dependent on the shape of the Woods-Saxon potential with parameters such as the radius, r_0, and the diffuseness, a. Thus, the spectroscopic factor is a model-dependent quantity through the single-particle ANC. This dependence on the single-particle parameters is discussed in more detail in the following sections.

Most DWBA calculations assume a unit normalization (eq. 2.9) as the definition of the spectroscopic factor for single-particle transfer reactions and therefore, S can be obtained by normalizing the experimental cross sections to the DWBA calculated cross section to give the single-particle strength of the experimentally measured distribution, i.e.,

$$\frac{d\sigma^{exp}}{d\Omega} \;=\; S^{exp}\frac{d\sigma^{DWBA}}{d\Omega} \tag{2.12}$$

This definition shows that the spectroscopic factor is directly dependent on the reaction theory. The region where the DWBA calculation is the most robust is at forward angles in the center of mass (c.m.) ($\theta_{cm} \lesssim 30°$) because the cross section is largest in this region and the approximation is typically truncated to leading order terms, neglecting higher order terms that contribute to the larger scattering angles; therefore the normalization is usually with respect to the first peak of the differential cross section distribution, $\frac{d\sigma}{d\Omega}(\theta)$.

2.3   Combined Method

The spectroscopic factor, S, is a measure of the nuclear wave function that is sensitive to both the interior as well as the asymptotic region. Therefore, deducing S is subject to many sources of uncertainty when extracted using experimental measurements. Some of the main sources of uncertainty include the global optical potentials, the DWBA/ADWA theoretical framework, and the bound-state potential. Most of the global optical potentials are based on models that are fit to data on stable nuclei and not the exotic neutron-rich nuclei requiring extrapolation to unstable nuclei, which could create large uncertainties in the extracted value for S. Some of the effects of the choice of optical potential on the extracted S were addressed by Liu *et al.* [Liu04]. The current work addresses the dependence on the bound-state potential through the parameters, radius (r_0) and diffuseness (a), that affect the single-particle ANC, $b_{\ell j}$.

The DWBA calculated cross sections are strongly dependent on the parameters chosen for the single-particle potentials. As shown in Figure 2.3, a small change in the geometry of the potential can greatly affect the value of the single-particle ANC, which directly affects the extracted spectroscopic factor that is proportional to $b_{\ell j}$. Reasonable choices for the potential parameters in the DWBA analysis that are based on known stable isotopes can lead to large differences in cross sections and spectroscopic factors differing by 25% [Sat83]. In most DWBA calculations, the geometry of the bound state potential is fixed and the potential well depth is varied to reproduce the measured binding energy. However, the normalization of the overlap function is sensitive to these parameters, which greatly affects the single-particle ANC and therefore the spectroscopic factor. This issue of an unknown bound-state potential is accentuated in the neutron-rich region where not much information is know about the nucleus, and the potential is predicted to become more diffuse [Dob96].

One way to help constrain the single-particle ANC is to measure a reaction at low

and high energies and combine the results, since the spectroscopic factor is a property of a given state in the nucleus and is independent of the energy of the probe. Low-energy transfer reactions ($<\approx$ 10 MeV/A) only probe the tail of the nuclear wave function and can be thought of as being strictly peripheral reactions. With these peripheral reactions, the many-body ANC, $C_{\ell j}$, is not as dependent on the shape of the bound-state potential and can be reliably extracted. Higher energy reactions ($>\approx$ 30 MeV/A) may probe deeper into the nucleus and are therefore sensitive to both the interior and exterior of the wave function of the nucleus, see Fig. 2.5.
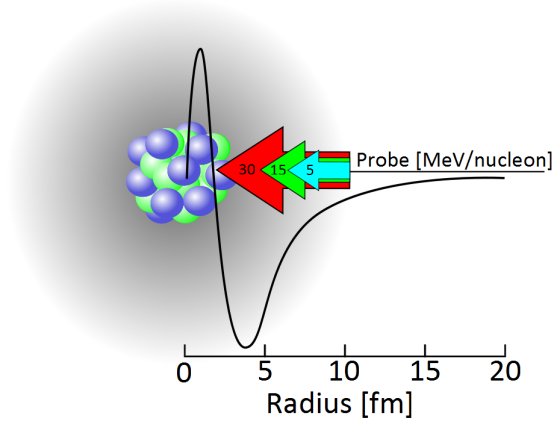
Figure 2.5: Relative beam energies probing the interior wave function of arbitrary nucleus. Figure adopted from [Tho09]

This method of measuring a reaction at two different energies was proposed by Mukhamedzhanov and Nunes [Muk05], and is referred to in this study as the combined method. The main advantage of the combined method for extracting spectroscopic factors is that the nuclear ANC is reliably extracted with a low-energy, peripheral reaction. As explained by Mukhamedzhanov *et al.* [Muk01], the many-body ANC, $C_{\ell j}$, obtained using the low-energy reaction can be used in the analysis of an independent measurement because it is a property of the state of the nucleus and should be independent of the energy of the probe. The external portion of the interaction is constrained with the low-energy measurement, and is used in combination with the

measurement of the less-peripheral reaction to extract a spectroscopic factor consistent with the many-body ANC. This procedure should constrain the single-particle ANC, $b_{\ell j}$ and therefore the shape of the bound-state potential.

2.3.1 Previous Studies

One of the first demonstrations of this combined method was an analysis using previously published data performed by Mukhamedzhanov, Nunes, and Mohr [Muk08], who compared ^{48}Ca(d, p) cross sections at various energies with neutron capture, ^{48}Ca(n, γ), cross sections. The authors were able to show the sensitivity of S and $C_{\ell j}$ to the single-particle ANC (spANC), $b_{\ell j}$, at low and high energies. The combined analysis using ADWA formalism at both energies indicates a constrained region for the spANC for both the ground- and first-excited states populated in the ^{48}Ca$(d, p)^{49}$Ca reaction. From this result, the authors suggested that measurements at $\sim$30 MeV/u have an interior contribution similar to (n, γ), and both the ANC and spectroscopic factor are important in calculating (n, γ) cross sections. Pang, Nunes, and Mukhamedzhanov [Pan07] pointed out the inconsistencies between the extracted ANC and spectroscopic factor arising from the choice of bound state parameters r_0 and a through DWBA and also ADWA. Reference [Pan07] also found it necessary to first fix the ANC with a peripheral measurement, then extract the spectroscopic factor using non-peripheral reactions.

A subsequent test of the combined method by McClesky *et al.* [McC14] involved the ^{14}C(d, p) reaction in inverse kinematics to deduce properties of the weakly bound ^{15}C. This work indicated that the combined method does yield a constrained region of single-particle ANC for the first excited state of ^{15}C using ADWA. However, this constraint resulted in an unphysical spectroscopic factor ($>$1.0), which may be attributed to the lack of representative single-nucleon optical potentials for light nuclei such as ^{14}C.

Following the combined method study on states in ^{15}C, Pang and Mukhamedzhanov [Pan14] tested the combined method for deuteron stripping reactions in three different mass regions and also using three different approaches, DWBA, ADWA and Continuum Discritized Coupled Channels (CDCC). The authors revealed inconsistencies between the ANC and spectroscopic factor, namely the spectroscopic factors from the combined method were much lower in comparison to previous results. Reference [Pan14] attributed this to a flaw in the reaction formalism in the treatment of the interior region of the nucleus. Consequently, the question remains open as to whether the combined method works generally and can provide consistent spectroscopic factors and ANCs, especially for the heavier nuclei important for the r-process. Additionally, it is also important to provide further tests of the method on nuclei for which global optical models are better constrained (e.g. A>24 [Loh74; Var91; Kon03]).

2.4   Reaction codes

Tremendous resources for the experimentalist are computer codes developed by nuclear reaction theorists, made available to calculate cross sections through both DWBA and ADWA formalisms. Common codes used for deuteron stripping reactions are TWOFNR [Tos14] and FRESCO [Tho88]. In this work, both TWOFNR and FRESCO are used for the reaction calculations. An example calculation using TWOFNR is shown in Fig. 2.6 showing predicted cross sections for $d(^{86}$Kr,$p)^{87}$Kr at 35 MeV/A and $d(^{84}$Se,$p)^{85}$Se at 45 MeV/A inverse kinematics reactions using ADWA and global optical potentials.

Traditionally, (d,p) reactions are performed at peripheral energies ($<$10 MeV/u). In this work, the same reactions are performed at non-peripheral energies ($>$35 MeV/u) to extract spectroscopic information that will be constrained by the low
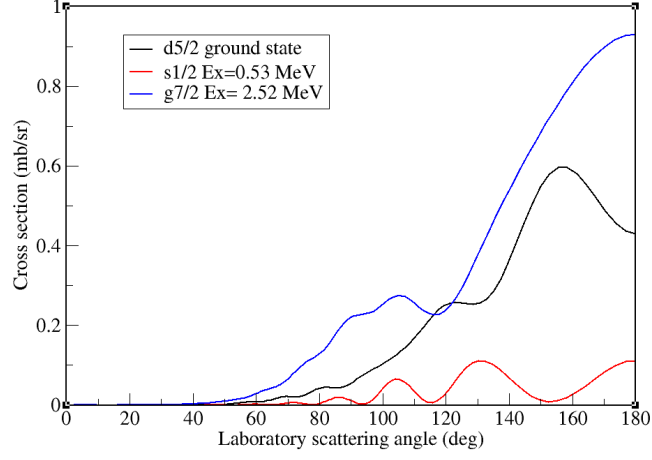
(a)
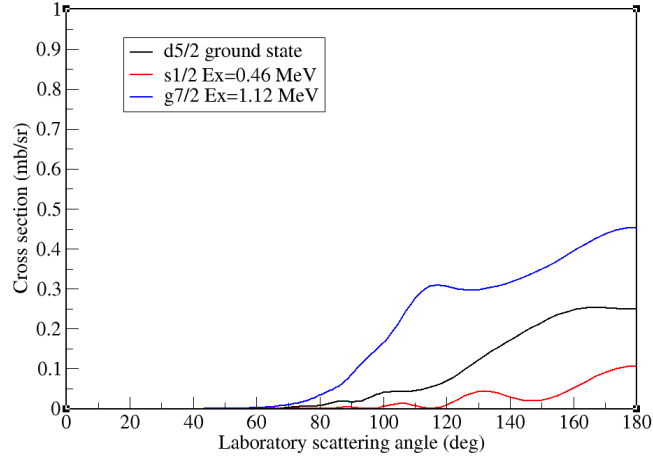
(b)

Figure 2.6: FR-ADWA calculations in the laboratory frame for (a) $d(^{86}\text{Kr}, p)^{87}\text{Kr}$ with 35 MeV/A ^{86}Kr beams and (b) $d(^{84}\text{Se}, p)^{85}\text{Se}$ with 45 MeV/A ^{84}Se beams showing calculated cross sections for transfer to the ground state (ℓ=2 transfer) (black), 1st excited state (ℓ=0 transfer) (red), and a state with ℓ=4 transfer (blue). Excitation energies (Ex) of each state are displayed. Unit spectroscopic factors are assumed.

energy measurements. These higher energy (d, p) reactions exhibit more experimental challenges than the low-energy counterparts. The calculations in Fig 2.6 display a few characteristic features to be expected with transfer reactions at non-peripheral energies. First, the cross sections are overall very low ($<$1 mb/sr) and greatly favor backward angles in the laboratory. Typically, reaction cross sections are peaked at backward angles due to the inverse kinematics, while forward peaked in the center of mass (see section 2.5). As the beam energies increase, the cross sections drop off faster and are significantly lower than the peak of the distribution towards 90° in the laboratory. Another feature of these specific transfer reactions at higher energies is favoring the higher angular momentum (ℓ) transfer, for example the ℓ=4 transfer shown in Fig. 2.6.

2.5   Inverse Kinematics

Transfer reactions involving radioactive nuclei are unique because of the short-lived nature of the species of interest. A stationary target cannot be made with an isotope that will decay away; therefore, these measurements have to be performed using inverse kinematics where the accelerated beam species is the radioactive, heavy isotope and the target is the light-mass particle. In this situation, the center of mass of the system is moving at a rate similar to the beam velocity, which leads to specific energy-angle systematics of the ejectile particle for different final states, such as elastic scattering, stripping reactions (*e.g.* (d, p)), and pick-up reactions (*e.g.* (p, d)). The main aspect of these reactions contributing to the inverse kinematics is the change in mass of the target-like particle. The mass of the target-like particle remains the same for the elastic scattering case, but the mass is decreased for the (d, p) stripping reaction from A=2 to A=1, and the opposite is true for the pick-up reaction (p, d).

The velocities of the two particles are inversely proportional to their mass, so the

target-like particle has a velocity that is much greater than the beam-like particle in the center of mass (c.m.) frame. For the elastic scattering case, since the target is initially at rest, the velocity of the center of mass is roughly equal and opposite to the initial velocity of the target in the center of mass frame, resulting in scattering angles close to 90° in the laboratory frame. A schematic of this elastic scattering case is shown in Fig. 2.7a.
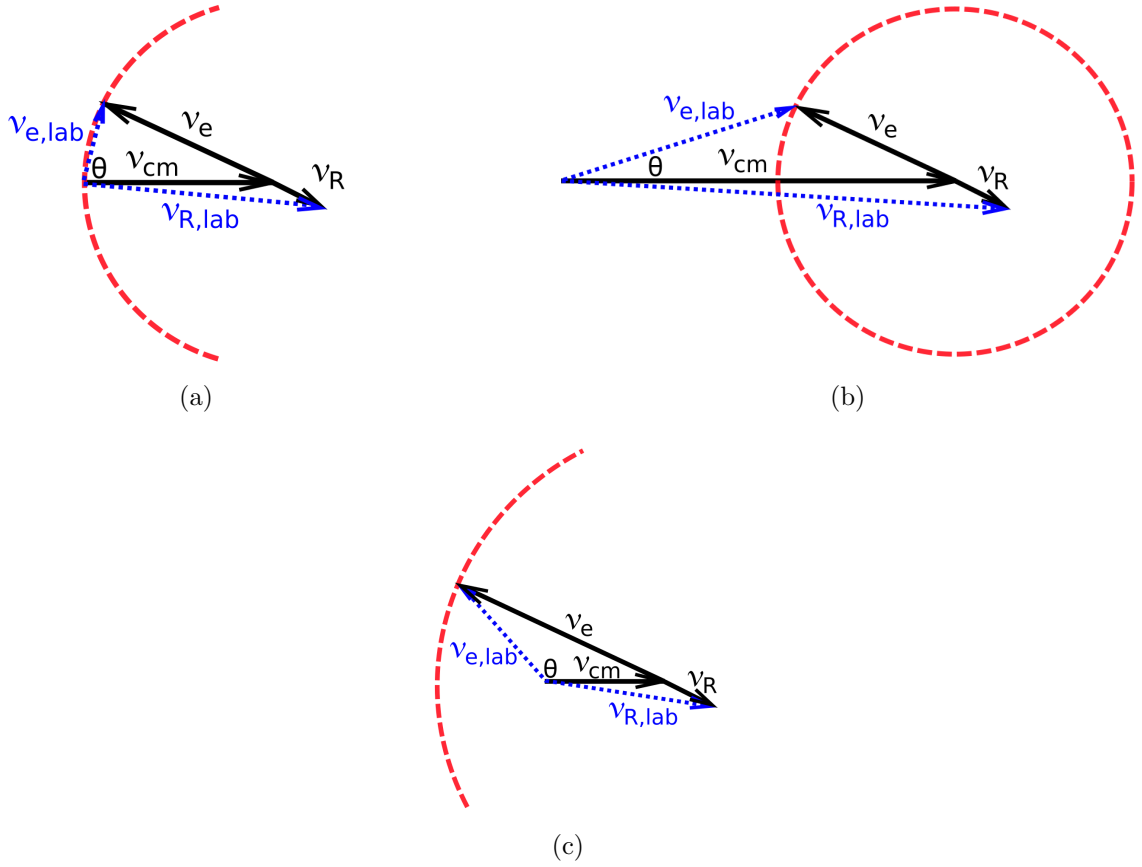
Figure 2.7: Velocity addition diagrams of two-body inverse kinematics for non-relativistic energies. Subscripts, R and e, are for the recoil (heavy particle) and ejectile (light particle) respectively. Black arrows indicate center of mass frame velocities and blue dotted lines represent the laboratory frame velocities. Angle, θ, is the laboratory scattering angle with respect to the beam axis. (a) Elastic scattering, (b) pick-up reaction such as (p, d), (c) stripping reactions such as (d, p). Figures adapted from Ref. [Cat02]

The relationship between the ejectile velocity, v_e, and the center of mass velocity, $v_{c.m.}$, is different for each of the cases shown in Fig. 2.7 mostly due to the mass

difference of the target-like particle. The schematics and equations presented in this section are only for non-relativistic cases for simplicity in showing the overall velocity relationships for typical transfer reactions. The relationship between v_e and $v_{c.m.}$ is shown in eq. 2.13 [Cat02].

$$\frac{v_e}{v_{c.m.}} = \left(q\frac{M_T}{M_e}\frac{M_R}{M_P}\right)^{1/2} \approx \sqrt{q\frac{M_T}{M_e}} \text{ if } M_R \approx M_P \qquad (2.13)$$

where M_T, M_P, M_e, M_R are the masses of the target, projectile, ejectile and recoil respectively. q is given by $q = 1 + Q_{tot}/E_{c.m.}$, with $Q_{tot} = (Q_{g.s.} - E_x)$ being the Q value for populating a state at excitation energy E_x in the recoil nucleus, and $E_{c.m.}$ being the center of mass collision energy. The value for q is close to unity for fast beams (e.g. $E_{beam} > 30$ MeV/u) as $E_{c.m.}$ is much larger than the Q-value for the transfer reaction. In (p, d) reactions (Fig. 2.7b), the ejectile deuteron is forward focused in the laboratory frame because the ejectile velocity in the center of mass frame is less than the center of mass velocity by a factor of $\sim \sqrt{1/2}$. In the case of (d, p) reactions (Fig. 2.7c), the ejectile proton will be detected at backwards angles ($> 90°$) in the laboratory because the ejectile velocity is larger than the center of mass velocity by a factor of $\sim \sqrt{2}$. Examples of the ejectile energies with respect to scattering angle for each of these cases are shown in Fig. 2.8, where the p_0 and p_1 represent population of the ground state and excited state respectively.

In this study, the (d, p) neutron transfer reaction using fast beams (e.g. > 30 MeV/u) with inverse kinematics presents many experimental challenges because the ejectile protons of interest are focused at very backward angles in the laboratory and rapidly increase in energy approaching $90°$.
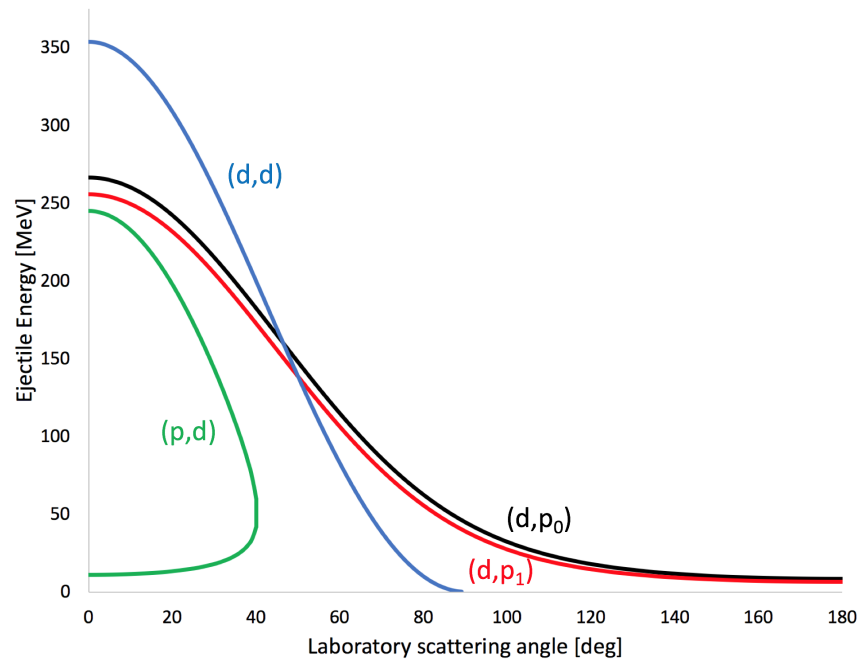
Figure 2.8: Kinematics calculations for deuteron stripping (d,p), elastic (d,d) and pickup (p,d) reactions showing ejectile energy as a function of laboratory scattering angle.

Chapter 3

Experimental Techniques

This chapter gives an overview of the techniques and detection systems used for the neutron transfer experiments $d(^{86}\mathrm{Kr},p)^{87}\mathrm{Kr}$ at 35 MeV/u and $d(^{84}\mathrm{Se},p)^{85}\mathrm{Se}$ at 45 MeV/u. Although the detector configurations and some techniques are slightly different for each of these experiments, each experiment used the same beam facility, similar targets, silicon detectors and calibration techniques. Differences between each experiment are made apparent in the subsequent sections, and the specific details are discussed in Chapters 4 and 5. The neutron detectors described in section 3.5 were not used in the neutron transfer experiments, but are important for single-particle transfer reactions such as (d, n), where the detected neutron provides information on the single-proton states in the final nucleus.

3.1 Beam Production

The National Superconducting Cyclotron Laboratory at Michigan State University uses a coupled-cyclotron system to produce rare-isotope beams for experimental studies. The coupled cyclotrons consist of a K500 and a K1200 system that produced first beams in 2000 [Mar01]. The beam production starts with a superconducting electron cyclotron resonance (SCECR) injector into the K500 cyclotron. The K500 can accelerate a handful of primary beam species to the transfer line of the K1200 cyclotron at 10's of MeV/A [Wu99]. The K1200 then further accelerates the beam species to 100 - 200 MeV/A.

The primary beam impinges on a production target which, in the ^{84}Se case, is a wedge of beryllium. The reaction products after the production target are guided to the A1900 fragment separator to select the radioactive isotope of interest. The A1900 has a maximum magnetic rigidity of 6 Tm, a momentum acceptance of $\Delta p/p = 5$ %, and a solid angle acceptance of $\Delta \Omega = 8$ msr [Sto05].

As shown in Figure 3.1, the isotope of interest is then directed toward the experiment target chamber and then to the focal plane of the S800 magnetic spectrograph (see section 3.2.3).
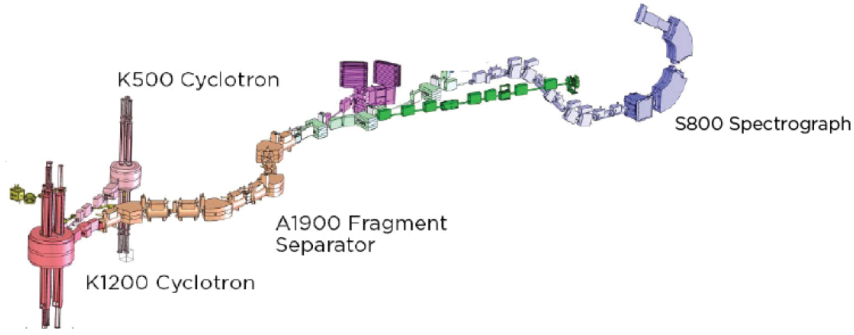
Figure 3.1: S800 beam line at the National Superconducting Cyclotron Laboratory [NSC18]

3.2   Detectors

At the target location of the S800 is the array of silicon strip detectors for detecting the reaction proton. There is also a pair of position-sensitive micro channel plates (MCPs) upstream of the target location for tracking the beam onto the target. The MCPs were only used in the ^{84}Se radioactive ion beam experiment, not in the ^{86}Kr stable beam experiment. Figure 3.2 shows the detector configuration for the $d(^{84}\mathrm{Se},p)^{85}\mathrm{Se}$ experiment. The Oak Ridge Rutgers University Barrel Array (ORRUBA) [Pai07; Pai09] is made up of 24 telescopes of silicon strip detectors of various types (see section 3.2.1) The SIlicon Detector Array (SIDAR) [Bar01] is an annular array that covers

the most backward angles in the laboratory. The two MCPs are located immediately upstream of the main scattering chamber for tracking the beam onto the target.
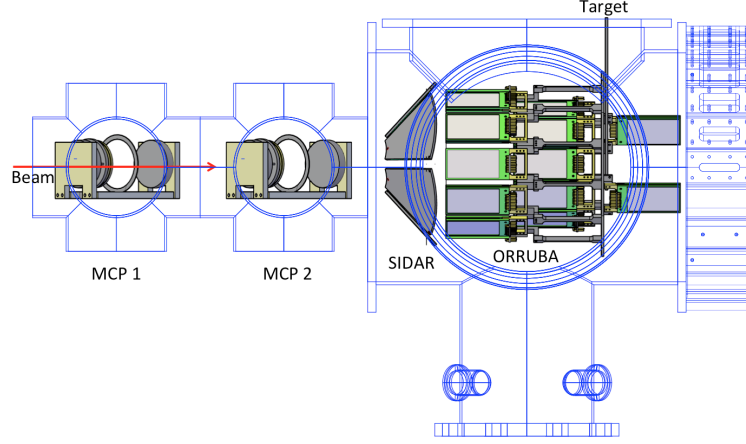
Figure 3.2: Schematic of the entire detector configuration used in the $d(^{84}\text{Se}, p)^{85}\text{Se}$ experiment at the NSCL.

3.2.1 Silicon detectors

Silicon detectors are commonly used for measuring charged particles in low-energy nuclear reactions. The different thicknesses and shapes provide flexibility for specific angular coverage and different energy regimes of charged particles. These semiconductors have a band gap of 1.115 eV at room temperature [Kno00], which is suitable for measuring light charged particles like protons and alphas without the need for cryogenic cooling. Figure 3.3 shows the front side of the typical silicon detectors that make up the barrel of the ORRUBA silicon array. All of the detectors used for ORRUBA are from Micron Semiconductor, Ltd [Mic18]. Figure 3.3a is an X3 type detector with resistive strips on the front side and a single backside readout channel. Also used in the barrel configuration are SuperX3 (SX3) detectors that are similar to the X3 detectors, but have 4 strips on the backside of the detector that are perpendicular to the front side strips. The active area for each of these detectors is 40 mm by 75 mm with different choices of thicknesses such as 500 μm and 1000 μm.

Shown in Figure 3.3b is the non-resistive BB10 style detector with 8 total strips on the front side and a single backside signal readout. The thin ($\sim$60 μm) BB10 style detectors are typically used as the ΔE layer in a stack of detectors, referred to as a telescope. The YY1 style, non-resistive, wedge shape detectors (Fig. 3.4) make up the annular SIDAR array. The active area of a SIDAR detector is around 8 cm in the radial direction and sweeps and angle of around 42°, making it possible to fit 8 SIDAR detectors in a flat circular configuration.

(a)   (b)
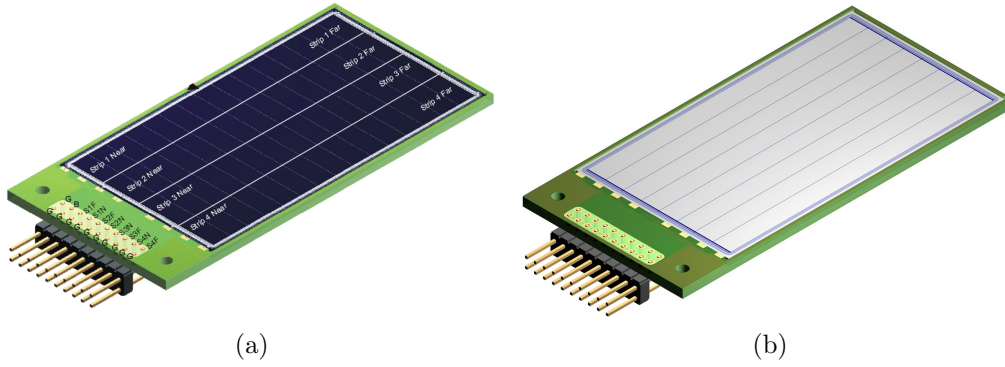
Figure 3.3: (a) Front side of X3 type resistive strip silicon detector. (b) Front side of the BB10 style detector. Figures from Micron Semiconductor, Ltd. [Mic18]
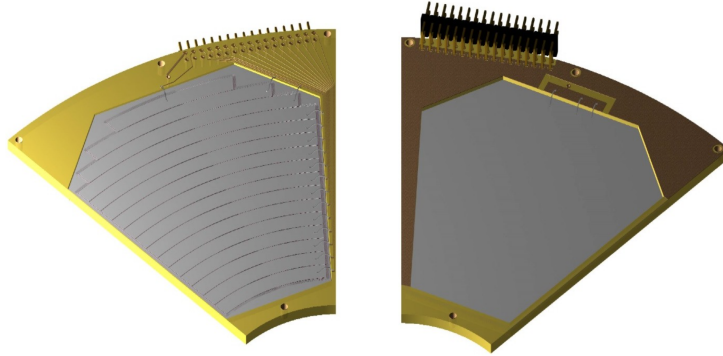
Figure 3.4: Front and back sides of a MSL-type YY1 wedge detector that make up the SIDAR array. Figure from Micron Semiconductor, Ltd. [Mic18]

Both energy and angle information are required to resolve kinematic lines for transfer reactions such as (d, p). The energy comes from the charge integration of the pulse created when a charged particle interacts with the semiconductor. Different

alpha sources such as [241]Am and [244]Cm are typically used as calibration sources, which have alpha energies around 5 MeV. The source used in the [84]Se experiment was a triple alpha source containing [241]Am, [244]Cm, and [239]Pu with alpha energies and intensities displayed in Table 3.1.

Table 3.1: Alpha energies from the triple alpha source [Joh15]

Isotope	alpha energy [MeV]	Intensity
[241]Am	5.486	84.8%
[241]Am	5.443	13.1%
[244]Cm	5.805	76.9%
[244]Cm	5.763	23.1%
[239]Pu	5.157	70.77%
[239]Pu	5.144	17.11%
[239]Pu	5.106	11.94%

The [86]Kr experiment used a [232]U calibration source which emits a large range of alpha particles from the entire decay chain. The alpha particles from the [232]U source and daughter products have energies and intensities shown in Table 3.2.

Table 3.2: Alpha energies from [232]U source and daughter products [Joh15]

Isotope	alpha energy [MeV]	Intensity
[232]U	5.320	68.15%
[228]Th	5.423	73.4%
[224]Ra	5.685	94.92%
[220]Rn	6.288	99.9%
[216]Po	6.778	99.998%
[212]Po	8.785	100%

Figure 3.5 shows a typical response of a single, resistive strip in an ORRUBA detector to a [232]U alpha source. The alpha energies from the decay of [232]U and [228]Th are too close in energy to resolve with the front-side, resistive strips of the silicon detectors so the peaks were not used for the calibration. Typically, total energy is recorded using the back-side, non-resistive strips which can have a full width half maximum (FWHM) of $\sim$ 30 keV at an alpha energy of $\sim$ 5 MeV. The front-side resistive strips may not be able to achieve this same energy resolution, and both sides are subject

to the resolution obtainable through the specific electronics setup (see Section 3.4). The peaks correspond to a known alpha energy, so a conversion between analog-to-digital conversion (ADC) channel number and energy can be achieved, assuming the response is linear in this energy range.
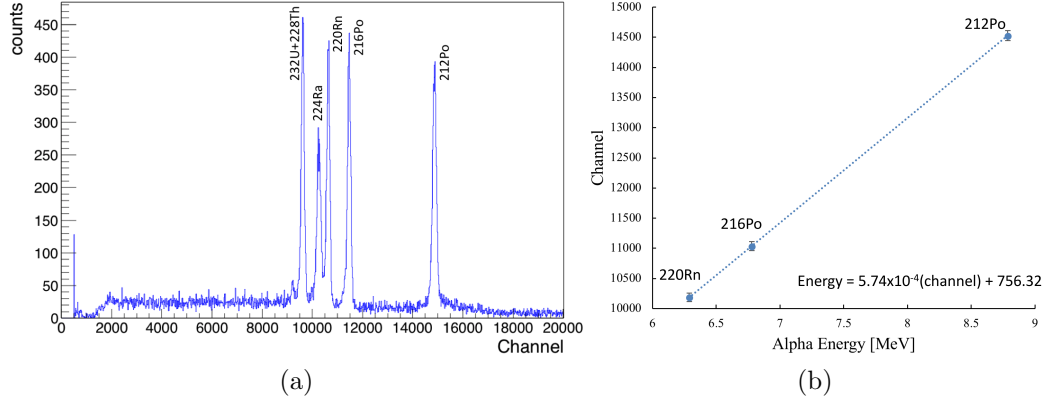
Figure 3.5: (a) Un-calibrated response of a single strip of an ORRUBA detector to alpha particles from a ^{232}U source. (b) Calibration parameters for the total energy deposited on the strip, using three alpha peaks for the conversion from channel to energy

The polar detection angle of a particle can be extracted from the interaction position of a particle on the detector. In a non-resistive silicon strip detector, the different strips cover a discrete angular range when oriented in the correct position and an angle can be assigned based on a specific strip. In a resistive strip detector, the angular information can be extracted by comparing the charge distributed to each end of the strip. The comparison of charge on each end of the strip to the total charge will provide information on the interaction point of the charged particle. Figure 3.6 shows the response of one end of a resistive strip as a function of the other end of the strip for a ^{232}U alpha source. Each strip end will have a slightly different response to the same energy deposited; therefore it is necessary to gain match each end of the strip. Once each end of the strip is properly gain matched, the total response (sum of each end of the strip) can be calibrated to convert the ADC channel to energy.

The interaction position along the strip is given by the ratio of charge collected at
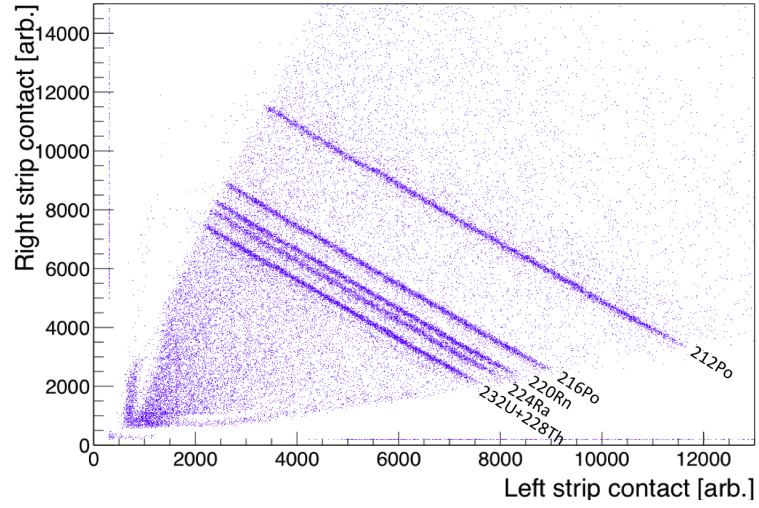
Figure 3.6: Un-calibrated response of a single resistive strip of an ORRUBA detector to alpha particles from a ^{232}U source.

each end, left (L) and right (R) by (L-R)/(L+R). Figure 3.7 shows the uncalibrated energy as a function of the end versus end charge distribution for a single resistive strip. The position is shifted by a factor in Fig. 3.7, which is why the bounds on the x-axis are not from -1 to 1.
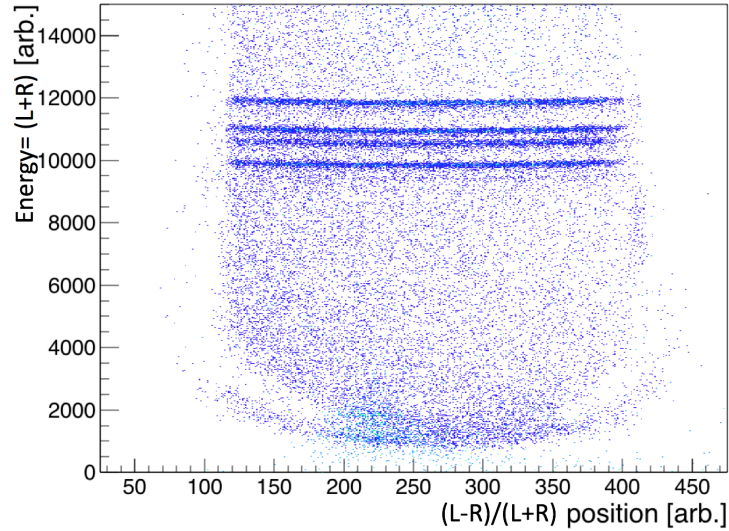
Figure 3.7: Uncalibrated charge balance of a resistive strip of an ORRUBA detector to alpha particles from a ^{232}U source.

The physical edges of the strip correspond to where the alpha lines end in Fig. 3.7. The known dimensions of the array and the length of the strip as compared to the

edges of the alpha lines provides a conversion to an angle relative to the target position in an experimental setup. The projection of Fig. 3.7 to the charge balance axis (x-axis) is shown in Fig. 3.8. The ends of the distribution are fitted with a half Gaussian and the value at the full-width half maximum (FWHM) give the channel of the end of the strip. Typical position resolution is about 1 mm, which is corresponds to an angular resolution of around 1 degree depending on the detector configuration.
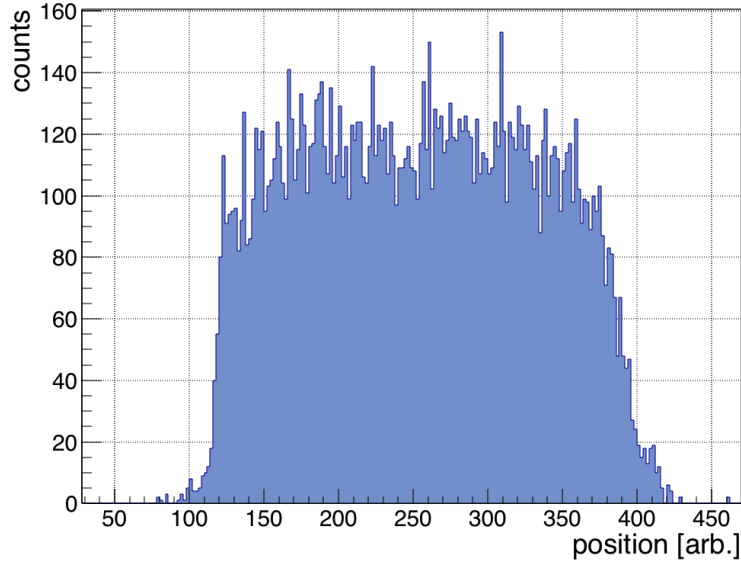
Figure 3.8: Projection of the charge balance of a resistive strip to locate the ends of each strip.

3.2.2   Beam tracking

Many rare isotope beam facilities rely on projectile fragmentation, and the isotope of interest is isolated using fragment separators. These secondary beams typically have broad momentum distributions from scattering and straggling from production targets and degraders. However, precise spectroscopic measurements require high-resolution in energy and position in order to resolve kinematic loci of final states populated in the reaction of interest. Typical beam spot sizes of radioactive nuclei produced by fragmentation can be on the order of centimeters; therefore, a precise

tracking system with position resolution on the order of millimeters is necessary to extract differential cross sections.

A system of two micro-channel plate (MCP) assemblies were used for timing and also tracking the incoming beam onto the target for the $d(^{84}\text{Se},p)^{85}\text{Se}$ experiment. Similar to previous tracking efforts [Sha00; Rog15], we employ MCP assemblies upstream of the target position to extract a two dimensional position with respect to the beam axis. As shown in Figure 3.9, an (x,y) position can be extracted as well as timing information from each MCP location. The two particle positions will provide a particle track to a precision within the position resolution of the MCPs, which with this size and configuration should be ~ 2 mm. The MCP used in this assembly are the 40 mm diameter, 3394A model from Quantar Technology, Inc. [Qua18]. The magnets used at each end of the assembly are 2.5 inch diameter permanent neodymium magnets from K&J magnetics, Inc. with a quoted surface field of 2451 Gauss [KJ18].

The incident beam particles pass through a 0.001 mil thick aluminized mylar foil. The accelerated beam produces electrons through ionization of the foil, which are directed toward the face of the MCP detector by an electric field. The foil is held at -1000 V and the front face of the MCP is held very close to ground. Once the electrons interact with the face of the MCP, a cascade of electrons is created through the chevron stacked micro-channel plates and directed to the resistive anode with a successive potential difference between plates within the MCP. As previously mentioned, the front face is held close to ground and each plate has a voltage that is assigned by the voltage divider circuit shown in Fig. 3.11. The plate furthest away from the foil has a voltage around +2000 V with an input high voltage (HV_{in}) of +2100 V.

The resistive anode has four contacts on each corner of the resistive anode plate that provide the position information of the incident electrons through charge integration of the signal. The charge integration of the signal was performed using
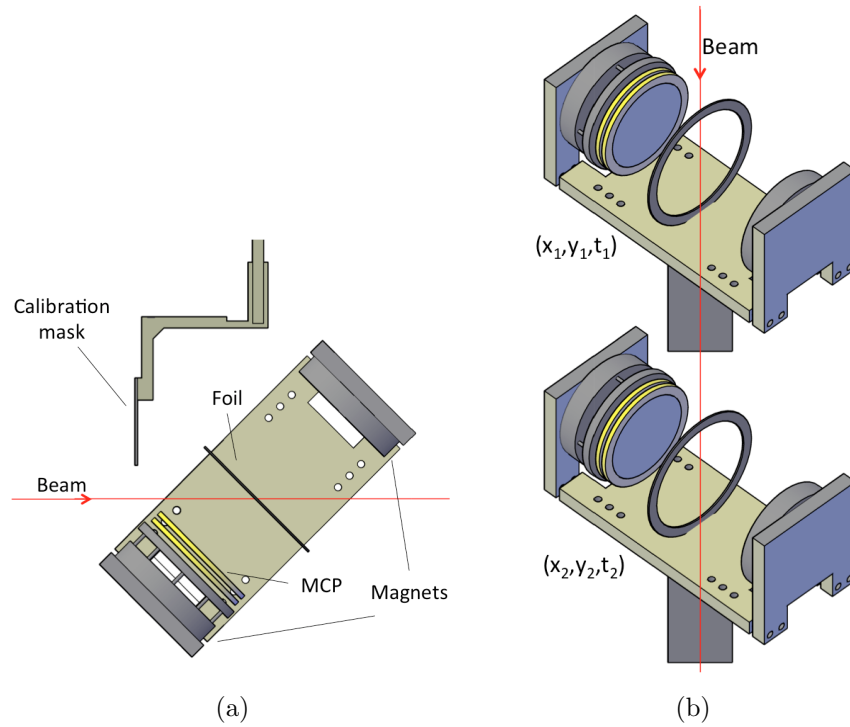
Figure 3.9: Schematic of the MCP assemblies used in the ^{84}Se(d,p)^{85}Se experiment for beam tracking. Top view (a) labels individual components and shows the orientation of the assembly with respect to the beam. Angle view (b) of both MCP assemblies as configured for tracking the beam particles onto the target.
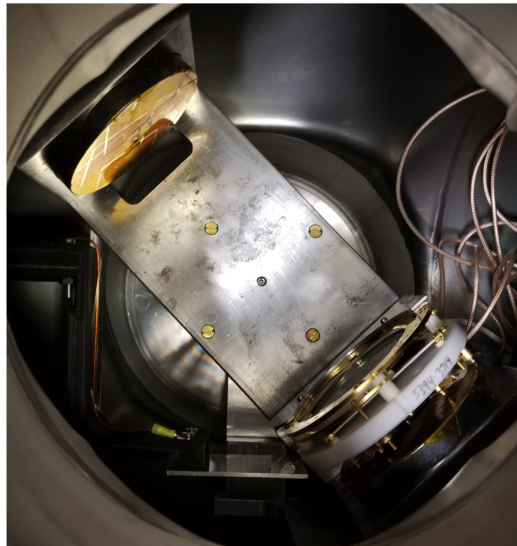
Figure 3.10: Photo of one MCP assembly from a top down view. Aluminized mylar foil is not visible. MCP is located on the bottom right hand side of photo.
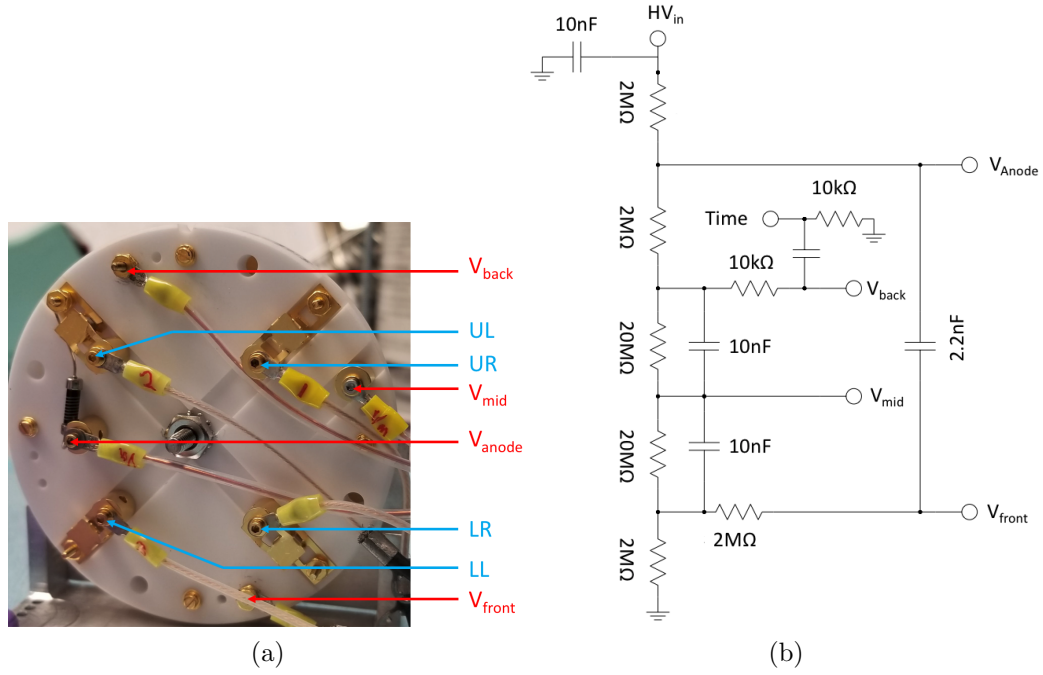
Figure 3.11: (a) Backside view of MCP showing the pin positions for signals and high voltage. (b) Voltage divider circuit for distributing bias to each plate of the MCP. [Fam17]

either a Charge-to-Digital Conversion (QDC) module (CAEN V792 [CAE18]) or a Mesytec MPD4 module [Mes18]. Similar to the charge balance in the resistive strip silicon detectors, the reconstructed X and Y position of the incident position is given by Eq. 3.1 and Eq. 3.2 with the signals from each corner of the resistive anode (i.e. upper left (UL), upper right (UR), lower left (LL), lower right (LR)).

$$X = \frac{(UL + LL) - (UR + LR)}{(UL + UR + LL + LR)} \tag{3.1}$$

$$Y = \frac{(UL + UR) - (LL + LR)}{(UL + UR + LL + LR)} \tag{3.2}$$

The reconstructed X and Y position of the incident electrons has to be calibrated to reconstruct the actual beam position along the beam axis. This is achieved by placing a sufficiently thick aluminum mask with known hole pattern in the beam line, perpendicular to the beam axis, directly in front of the foil. A schematic of

a calibration mask is shown in Fig. 3.12. The known position and hole dimensions provide a reference point for the position calibration of the MCP. The notch in the pattern preserves the chirality of the the reconstructed image. The raw (uncalibrated) reconstructed image of the mask is also shown in Fig. 3.12.

(a)   (b)
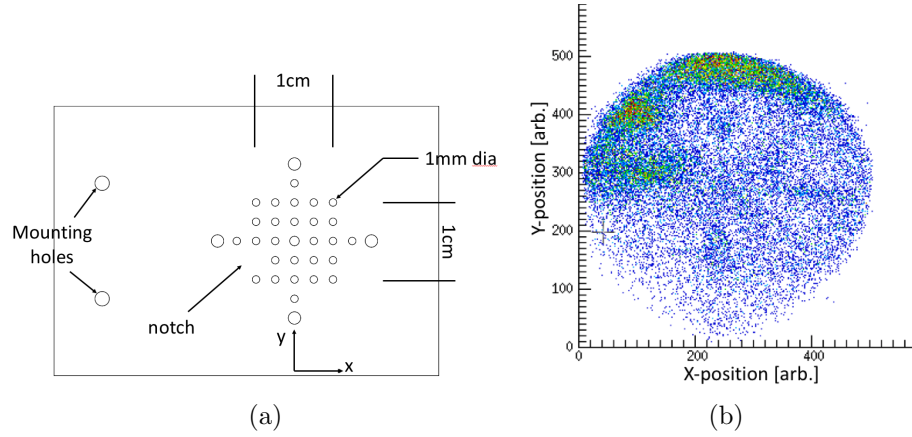
Figure 3.12: (a) Schematic of a calibration mask. (b) Raw reconstruction of mask image using a Mesytec MPD4 module

The mask image is poorly reconstructed due to a few reasons, possibly including the placement of the mask relative to the foil, the strength of the magnetic field, and also the dimensions of the return yoke. First, the mask should have been placed as close as possible to the foil to mitigate the opening angle of particles that go through each hole in the mask. The mask could have also been placed directly on the foil, although the reconstructed position would have to account for the angle of the foil with respect to the beam axis. Next, the magnetic field strength was not fine tuned for the dimensions of the MCP assembly. Ideally, the electrons produced in the interaction of the beam with the foil would undergo an integer number of orbits as they travel toward the MCP face from the cyclotron motion induced by the magnetic field. This precession preserves the original location that the electrons left the foil. In the case of the reconstructed image in Fig. 3.12, the magnetic field strength was set by the permanent magnets in a fixed position. The ability to tune the magnetic

field strength would have helped focus the image had the magnets been free to move along the axis of the MCP assembly. Last, the return yoke that holds the magnets in place and directs the fringe fields away from interacting with the surrounding material may have needed different dimensions. The compact geometry of the assembly may have decreased the total magnetic field between the magnets and also created a non-uniform magnetic field along the axis of the MCP assembly. The magnets were very close to the return yoke, and also recessed into the steel housing, which may have caused much of the magnetic field to return to the yoke, rather than the opposing pole. A better design would keep the magnets as far away from the return yoke as possible while preserving the structural integrity of keeping the strong magnets a set distance apart, although this would require a significant amount of space inside a large vacuum chamber.

Although the position reconstruction was unsuccessful in this commissioning experiment with ^{84}Se beams, the MCPs are nearly 100% efficient at detecting beam particles that pass through the foils. The timing signals were used for time of flight measurements between different detectors in the beam line such as the focal plane of the S800 and the RF signal from the cyclotron. Also the MCPs are used to measure the incoming beam rate, which is used to normalize the differential cross section.

After the commissioning experiment, the MCP position reconstruction was tested by the response to alpha particles directly incident on the face of of the MCP. This test was to make sure that the original issues in the reconstruction were not due to a faulty detector, but rather due to the issues discussed in detail above. Figure 3.13 shows the raw position reconstruction of the calibration mask in a vertical position, oriented by the notch (see Fig. 3.12). Although the spectrum is not calibrated and each of the corners of the anode are not well gain matched, the mask image is clearly visible, confirming that the detector was not faulty and the issues with the position reconstruction during the experiment were from other sources. These tests could

not have been performed prior to beam time because the new MCP assemblies were shipped and received very close to the start of the experiment, and were first mounted at the experiment.
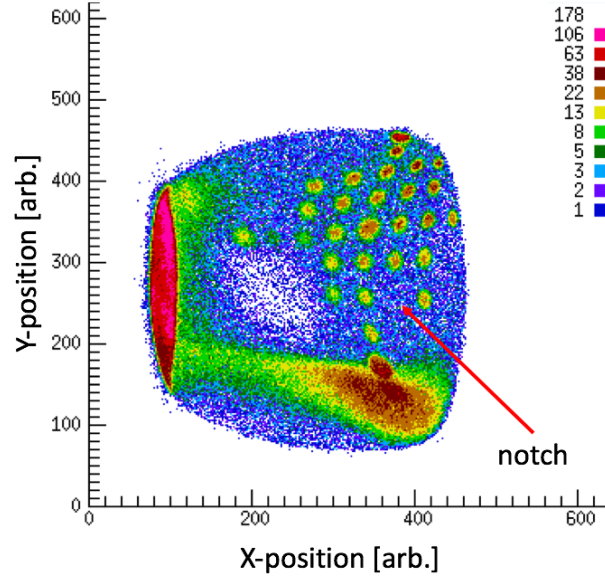
Figure 3.13: Raw reconstruction of mask image placed vertically directly in front of an MCP instrumented with an MPD4 module. Alpha particles from a ^{244}Cm source were directly incident on face of MCP.

3.2.3 S800 spectrograph

The S800 spectrograph [Baz03] is a high-resolution, large-acceptance device used in this work for the detection of the heavy recoil in coincidence with the proton from the (d, p) reaction measurement. The coincidence measurement is essential to clean up the background of charged particles (*e.g.* fusion evaporation products from the carbon in the target) detected by the silicon detector array. The S800 is a three story tall spectrograph that directs beam particles to the focal plane after the target location by a quadrupole doublet and two dipole magnets. Figure 3.14 shows a schematic of the S800 with respect to the target focal point where the main reaction scattering chamber is placed.
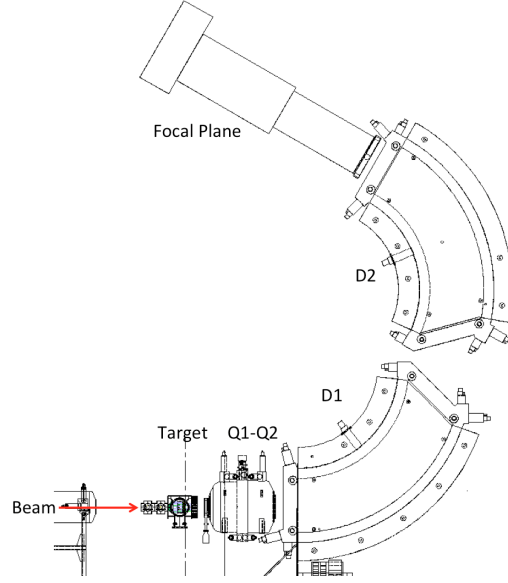
Figure 3.14: Schematic of the S800 with respect to the target position

The focal plane of the S800, shown in Figure 3.15, consists of two, position sensitive Cathode Readout Drift Chambers (CRDCs), an ion chamber, and scintillator detectors [Yur99].

The CRDCs provide a position and angle measurement of incoming particles (see Fig. 3.16). They are separated by a distance of 1 m with an active area of 30 cm (non-dispersive direction) x 56 cm (dispersive direction) and each with a thickness of 1.5 cm. Each detector is filled with a gas pressure of 40 Torr with 80% CF_4 and 20% C_4H_{10} due to the low aging characteristics and high drift velocity [Yur99]. The CRDCs rely on the ionization of gas along the particle track to provide the readout signals. Although the gas mixture is chosen based on the high drift velocity, the electron drift time constrains the maximum counting rate of the entire focal plane, which is typically less than $\sim$5000 pps.

The drift time of the electrons in the CRDCs depend on the position of the interaction, the pressure of the gas, and the voltage applied to drift the electrons to the cathode; therefore, the interaction position of the incoming beam needs to be calibrated. Similar to the calibration procedure of the MCPs in section 3.2.2
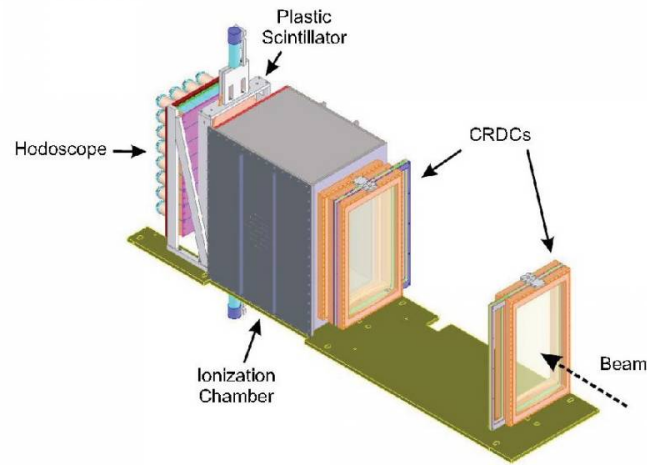
Figure 3.15: S800 focal plane detectors [S8018]
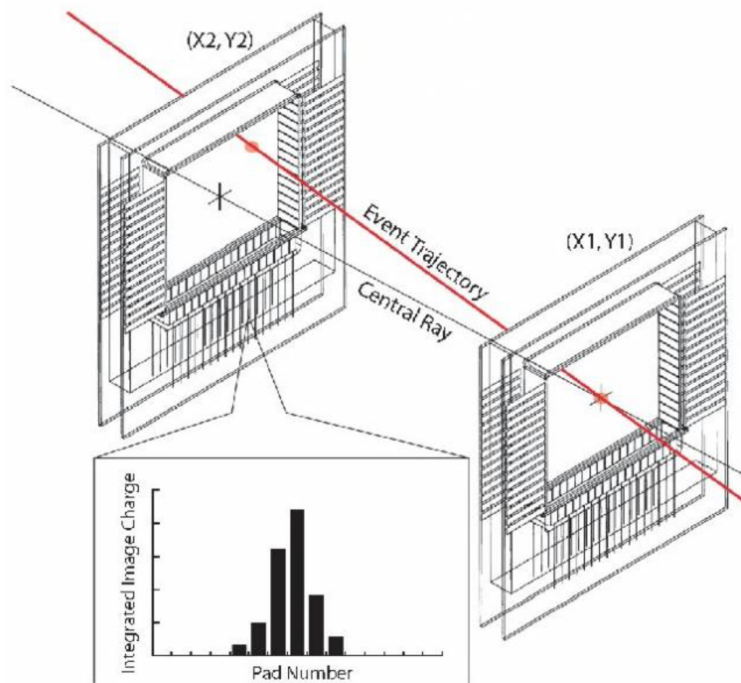
Figure 3.16: Schematic of the two cathode readout drift chambers used to reconstruct the trajectory of the incoming particles [S8018]

this calibration procedure involes a mask in front of each CRDC with a known hole pattern. The known location of the holes with respect to the beam axis allows the electron drift times to be converted to positions. A typical masked spectrum is shown in Fig. 3.17. The particle trajectory through the CRDCs can then be tracked back to the target position by using an inverse map of the spectrograph's magnetic field through the ion-optics code COSY infinity [Ber93; Ber90].
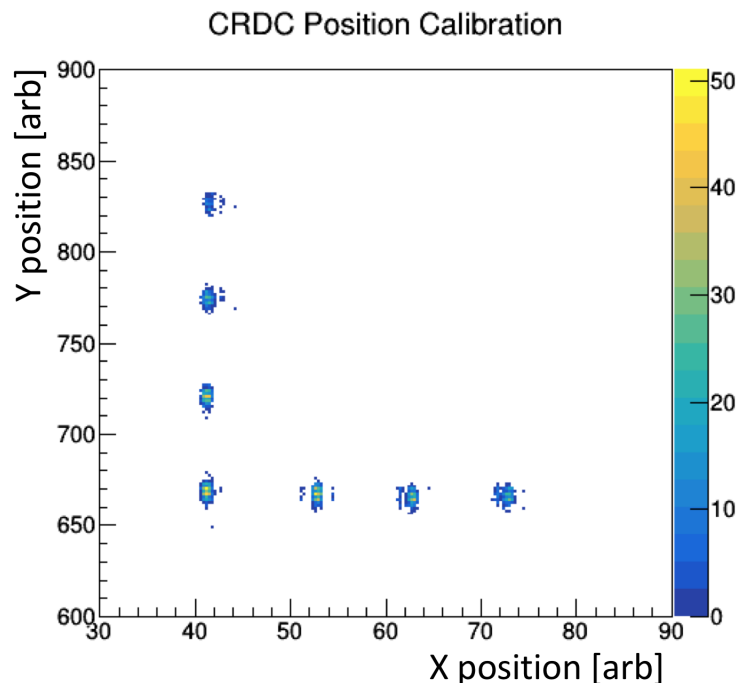
Figure 3.17: A typical CRDC mask calibration spectrum to calibrate the x-y interaction point of particles with respect to the beam axis.

The ionization chamber is directly downstream of the CRDCs, and provides particle identification using the energy loss in combination with a time of flight. The chamber has 16 anode segments and is filled with P10 (90% argon, 10% methane) gas at a typical pressure of 300 Torr. Each anode segment will have a different gain, and therefore needs to be calibrated. Figure 3.18 shows the response of each anode to incoming particles for the calibrated and un-calibrated cases.

The energy loss through the ion chamber depends on the mass and charge of the
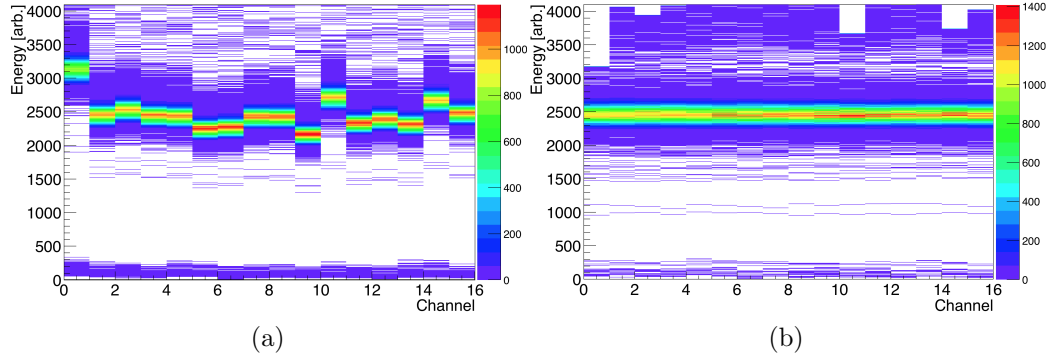
Figure 3.18: (a) Un-calibrated and (b) calibrated energy deposited in the ionization chamber as a function of each anode or channel.

particles, which helps to distinguish different beam species that make it to the focal plane. A typical particle identification technique combines the energy loss seen in the ionization chamber and the time of flight of the incoming particles.

The E1 scintillator is downstream of the ionization chamber and provides a trigger and a stop time for time-of-flight measurements relative to a given start signal. The start signal can come from a variety of places upstream, including the XFP scintillator (furthest upstream), the obect (OBJ) scintillator, the RF signal from the cyclotron, and also from the MCPs at the target location. The final detector in the focal plane is an array of 32 CsI(Na) scintillators that provide a timing signal as well as energy or total energy measurements.

3.3 Targets

Transfer reaction measurements such as (d, p), (d, n), (d, t), etc traditionally use deuterated polyethylene (C_2D_4) as the source of deuterium in a self-supporting target. Although there exists cryogenic targets capable of producing relatively pure deuterium targets [Gil13], large infrastructure is required to sustain the targets under constant energy deposited by the radioactive ion beam. Polyethylene is a suitable choice for targets because of their durability and high aerial density of deuterium.

Also the low Z of the "contaminants" (i.e. carbon and hydrogen) do not cause significant energy loss within the target. Larger mass contaminants would broaden the energy distribution of the ejectile particle of interest (protons in this case), causing some kinematic loci to be indistinguishable.

Deuterated polyethylene targets of various thicknesses were prepared following the method described in detail in Ref. [Feb17]. One of the main differences used in this study from the traditional methods of making C_2D_4 films is annealing. This step significantly increased the durability of the films, making it much easier to mount very thin films (~ 30 $\mu g/cm^2$) on target frames. Annealed targets were also more transparent, which is attributed to the C_2D_4 polymer chains relaxing into a preferred configuration while being heated.

The different thicknesses of targets are attempted during the initial mixing phase; however, due to uncontrollable material loss through the entire process, a more precise determination of the thicknesses should be measured with energy loss of particles through the target. For targets with thicknesses ≤ 1 mg/cm^2, a common alpha source such as ^{244}Cm is sufficient to measure the energy loss through the target. The target thickness is extracted using the following equation,

$$\Delta E = -\frac{dE}{dx} \cdot x \tag{3.3}$$

where the stopping power, $\frac{dE}{dx}$, of alpha particles for polyethylene is well known [Ber05]. For thicker targets (> 1 mg/cm^2), the straggling in the measured energy loss of a 5-MeV alpha particle becomes significant. In this case, it is desirable to measure energy loss through the target with an accelerated beam of particles with higher energy for a more accurate measurement of the thickness of the film.

Figure 3.19 shows the target ladder for the $^{86}Kr(d,p)$ measurement. The beam spot damage is highlighted on one of the C_2D_4 targets. The phosphor beam viewer shows a bright spot whenever the accelerated beam is incident on the viewer, which

is used for beam tuning. The polypropylene (C_3H_6) target is used to ascertain the background events from reactions on carbon and hydrogen that are present in the C_2D_4 target measurements.
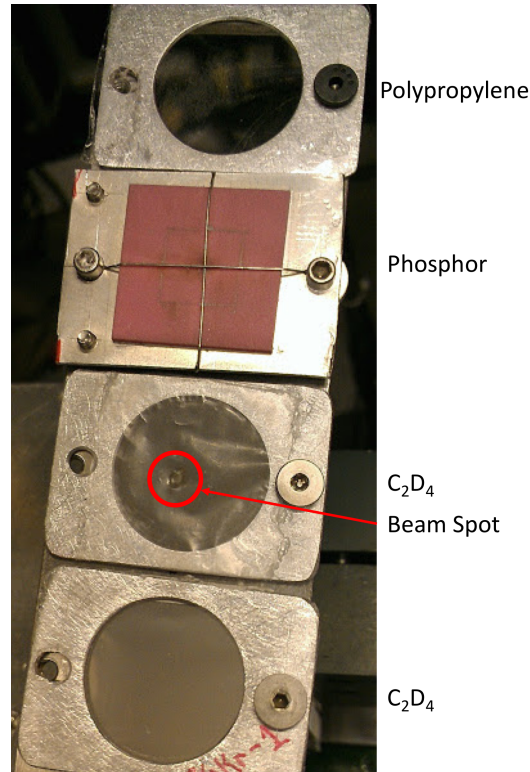
Figure 3.19: Target ladder with C_2D_4 targets, phosphor viewer, and polypropylene target from [86]Kr beam measurement. Beam damage visible on second target from the bottom

3.4 Electronics

When a charged particle interacts with a silicon detector, an electrical current pulse is produced. This pulse needs to be converted to a readable signal in the data acquisition system. In a typical electronics setup, the current created by a charged particle interacting with the silicon is integrated by a preamplifier to produce a voltage pulse with an amplitude that is directly proportional to the energy deposited in the detector. The preamplified signal has an amplitude of a few hundred mV and could also have

a long decay time on the order of $\sim$ 10s of μs. A shaping amplifier is used to both amplify the signal and ensures a quick decay time so subsequent signals do not overlap. A discriminator is then needed to reject the low amplitude electronic noise and to create a trigger signal which will be used to create a gate, which puts the analog-to-digital converter (ADC) in peak detection and hold mode. While the ADC processes signals, the trigger module will send out a busy signal to veto any additional signals from being processed. The trigger signals from multiple detectors are organized by a logic OR module that will reject new trigger events based on the busy signal from the VME. A schematic of the signal logic for a typical analog electronics acquisition system is shown in Fig. 3.20.
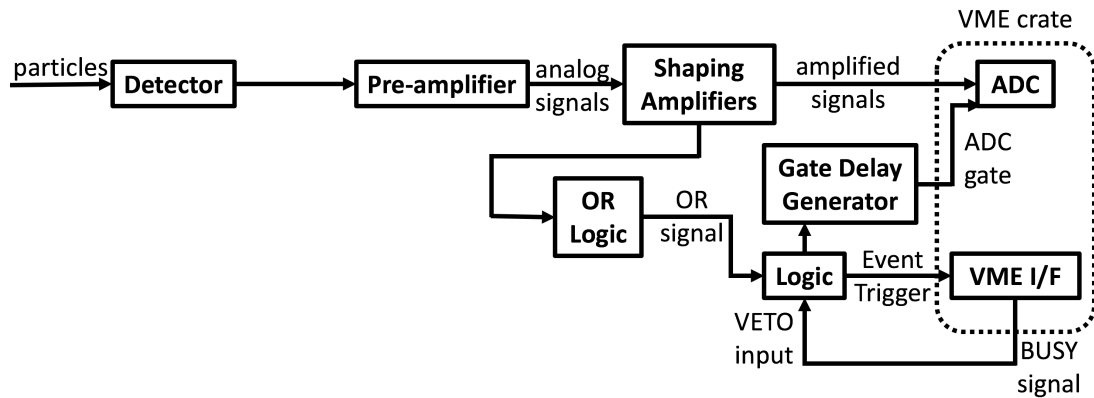
Figure 3.20: Schematic of the analog signal logic. Figure adapted from [Ahn13]

Common to both the ^{86}Kr and ^{84}Se experiments are the signal feed-through boards and preamplifier boxes containing the charge sensitive preamplifiers. The electronics systems used after the initial preamplification were slightly different in each experiment, and will be discussed in the subsequent sections.

Feed-through boards were used to direct the front and back side signals to the preamp boxes in a compact geometry. Each feed-through board can take the signals from up to six superX3 type detectors. Other feed-through boards designed for the BB10 type detectors can handle signals from eight BB10 detectors. Simple feedthrough pins were used for the SIDAR detector signals.

Each of the feed-through boards direct signals from the detectors through two 40-pin high-density cables to the preamp boxes. Each signal is amplified through charge-sensitive preamplifier chips. Each preamp chip has an associated gain (e.g. 15 mV/MeV, 27 mV/MeV, 60 mV/MeV) that can be changed depending on the desired signal gain.

3.4.1 Conventional electronics setup

For the d,(^{84}Se,p)^{85}Se experiment in Dec 2017, the preamplified signals were sent through 16-channel Mesytec MSCF-16 shaping amplifiers [Mes18], which is a standard analog electronics acquisition system shown by the schematic in Fig. 3.20. Each Mesytec shaping amplifier handles up to 16 preamplified signals from the silicon detectors and contains constant fraction discriminators (CFD) for the trigger signal. The trigger signal from each MSCF-16 module is input to a logic fan-in/fan-out unit and then sent to trigger the acquisition system. The master trigger is then handled by an ORNL trigger module that takes in the master trigger and sends out a busy signal while the ADCs are being read. This electronics setup can achieve ~ 30 keV energy resolution with a 1000 μm silicon detector, and can store up to 10 kHz data rate in a single crate.

The shaped signals, using a shaping time of 0.25 μs, are read in the data acquisition system through an array of 32-channel CAEN V785 peak sensing ADCs [CAE18]. The signals from the ADC are then read out through an MVME 5500 computer in the VME crate and transmitted to the acquisition computer via Ethernet.

3.4.2 ASICs

An Application Specific Integrated Circuit system (ASICs) was implemented for the d,(^{86}Kr,p)^{87}Kr experiment in March 2014. This system was designed to support a large number of channels while reducing the size and cost of readout electronics

[Wal07]. The ASICs chips were developed at Washington University - St. Louis, and can each handle 16 channels of electronics. Each ASICs chip board houses charge sensing amplifiers (CSAs), shaping amplifiers, positive/negative polarity peak sensors, and constant fraction discriminators (CFDs) [Eng07]. This electonics setup is limited to a data rate of ~ 1 kHz and can achieve an energy resolution of roughly 60 keV with a 1000 μm silicon detector. A schematic of the signal logic for the ASICs system is shown in Fig. 3.21, and a photo of the chipboards and motherboards is shown in Fig. 3.22.
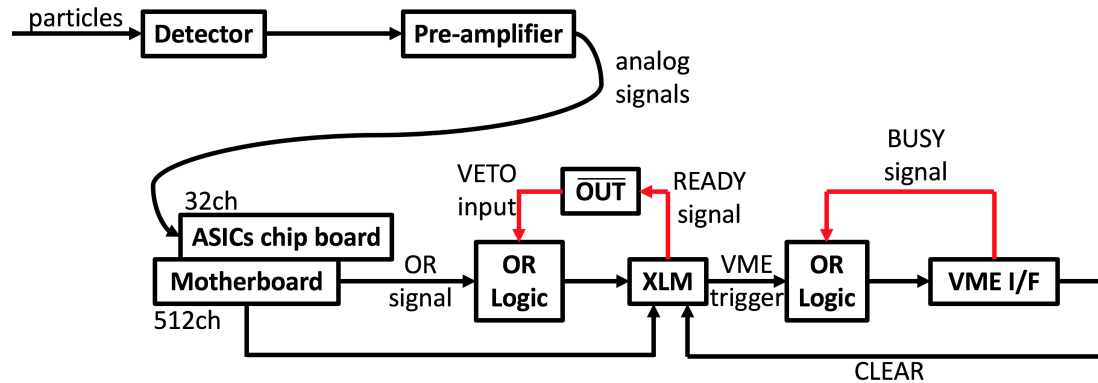
Figure 3.21: Schematic of the signal logic for the ASIC system. Figure adapted from [Ahn13]

Signals from the motherboard of the ASICs system are controlled by the FPGA on board a JTEC XLMXXV universal logic module (XLM). The XLM also contains the ADC to read voltages from the ASICs chip boards and 16 MByte of memory to store digitized data from the ADC. A VME I/F module (VMUSB) then handles the data from the XLM, and sends it to the acquisition computer via Ethernet.
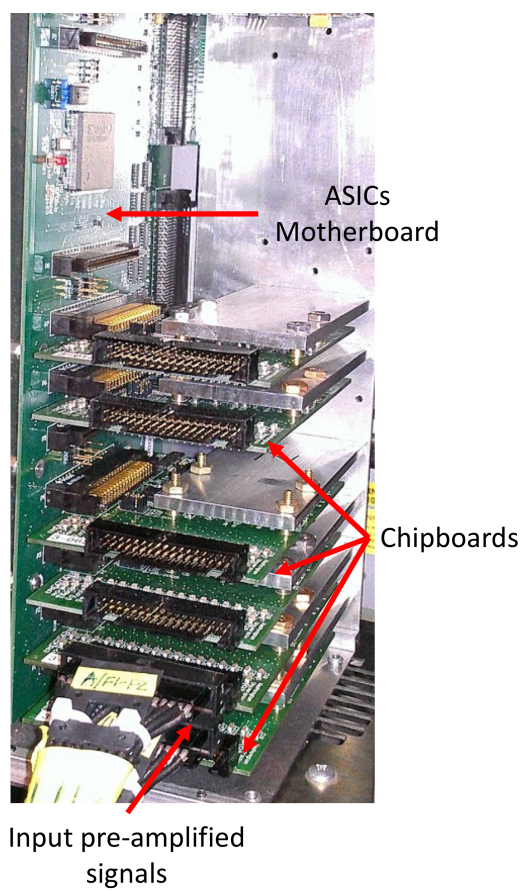
Figure 3.22: Photo of the input signal cables to the chip boards that are connected to the ASICs motherboard.

3.5 Neutron detection with liquid scintillators

Inverse kinematic reactions with radioactive ion beams on light targets have made it possible to investigate weakly-bound nuclei relevant to nucleosynthesis. Similar to single-neutron transfer reactions like (d,p), proton transfer reactions like (d,n) can provide insight into the single-proton states of nuclei, albeit with different experimental challenges. For example, neutron detection efficiencies are typically on the order of 30%, while silicon detectors are about 100%. Neutrons do not deposit their full energy, so time-of-flight measurements or spectrum unfolding techniques are necessary to measure the energy. It is also very difficult to achieve 1 mm position resolution as with silicon strip detectors, so typically larger arrays are placed farther away, which helps with the energy resolution when using time-of-flight, but significantly reduces the geometric efficiency. In addition, expected beam intensities are low (10^5 pps) requiring highly efficient arrays to achieve reasonable counting statistics in typical 1 week experiments. Also, reactions using inverse kinematics suffer from compression of the kinematic loci at backward angles in the laboratory, requiring sufficient energy and position resolution to distinguish the different nuclear states. For (d,n) studies, precise measurements of the neutron energy as well as the emission angle are essential to provide spectroscopic information of the final nucleus. Neutron energies can range from hundreds of keV to tens of MeV for radioactive ion beam energies of $\sim$5-10 MeV/A, which are typical beam energies for these single particle transfer reactions. In addition, high gamma ray background environments from in-flight production and the decay of stopped radioactive beams can saturate the neutron signals needed for precision measurements.

Fast neutrons can be detected indirectly using scintillation-type detectors coupled to photo-multiplier tubes (PMT) [Kno00]. Liquid scintillators, in particular, have been used for nuclear physics applications for decades [Ber73; Ver68; Bir72].

Traditionally, neutrons are detected using a time of flight technique to measure the energy of the neutron using the following equation:

$$E = \frac{1}{2}m(\frac{d^2}{\Delta t^2}) \tag{3.4}$$

where the energy (E) depends on the length of the flight path (d) and time of flight (Δt). The energy resolution achievable with this method depends on the measurement of the flight path, detector thickness, and uncertainty in the timing of the start and stop signals. Energy resolution improves proportionally with the square of the path length used, requiring long distances for high resolution measurements. For RIB experiments, this is a tradeoff between energy resolution and detection efficiency, as longer path lengths reduce the geometric acceptance and thus the total efficiency of the detector.

A new liquid scintillator array has been constructed at Oak Ridge National Laboratory (ORNL) for reactions studies. SABRE (Scintillation Array of Bars for Reaction Experiments) [Feb18a] consists of five bar-type detectors with a PMT coupled to each end, that contain custom-made liquid scintillator developed at ORNL. Figure 3.23 shows one of the SABRE detectors.

Figure 3.23: SABRE bar type liquid scintillator used for neutron detection in reaction studies.

These bar type detectors are unique because of the position resolution capabilities. A standard "can" type detector with a single PMT is limited in the spatial resolution

by the physical geometry of the detector. A bar-type detector collects light at each end, allowing the position of interaction to be reconstructed through timing and also light balance. Figure 3.24 shows the position resolution of a SABRE detector using the light balance of the left and right PMT (e.g. (L-R)/(L+R)), similar to the charge division in a resistive strip detector. A collimated ^{137}Cs source was positioned a fixed distance from the detector and moved parallel to the bar at 1-inch increments to produce the different peaks in Fig. 3.24.
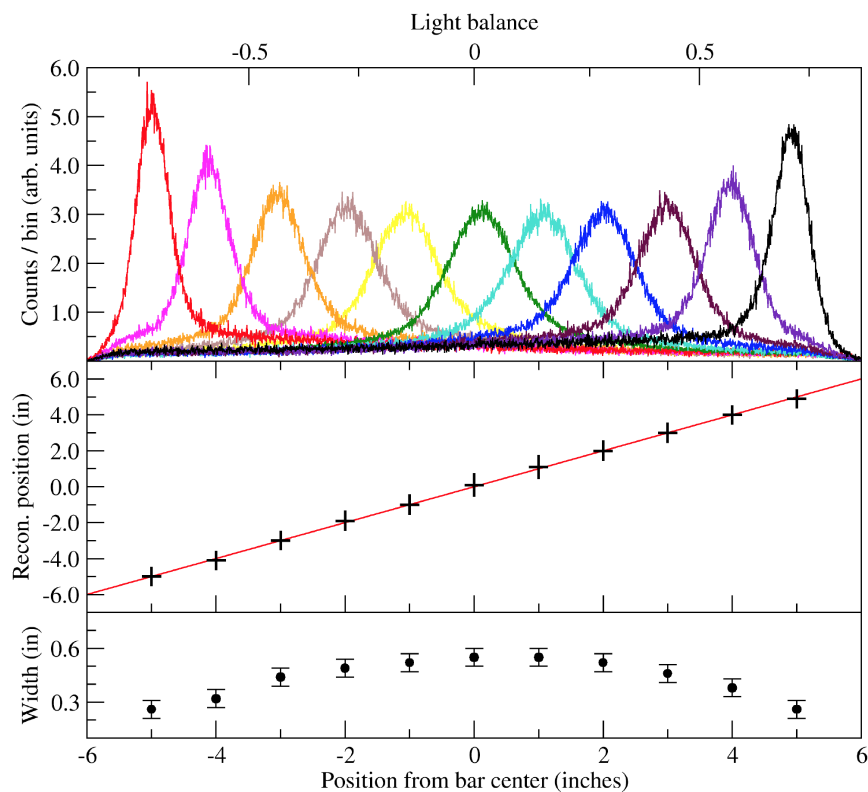
Figure 3.24: Position resolution of a SABRE bar in response to a collimated ^{137}Cs source moved along the bar at 1 inch increments

The position resolution depends on the reconstruction method, either timing or light balance. Different PMTs will have a faster timing response and therefore are better suited for using the time difference to reconstruct position. In the case of the SABRE detectors, the PMTs used are Hamamatsu R6231-100 with a rise time of 8.5 ns and a transit time of 48 ns, compared to the Hamamatsu R7724 PMT with

a rise time of 2.1 ns and a transit time of 1.2 ns [Ham18]. Therefore, the SABRE detectors are better suited for the light balance method for position reconstruction. These specific PMTs were chosen based on the excellent light response, which gives better pulse shape discrimination.

3.5.1   Pulse shape discrimination

In order to distinguish between a gamma ray and a neutron interaction inside the scintillator, we rely on the timing characteristics of the scintillation light, which is manifested as shorter or longer tails of a voltage pulse output by a photo-multiplier tube. The ratio of the integrated tail of the pulse to the total is used to discriminate between gamma-ray interactions and neutron interactions.

Ionization tracks in liquid scintillators produce many excited singlet and triplet states along the track. Recoil proton events, initiated by neutron interactions, create a high density of excited states. In contrast, electron recoils from gamma ray interactions produce a lower density of singlet and triplet states along the particle track. Excited singlet states can decay through fluorescence, on a time scale of a few ns. Triplet-triplet annihilation will eventually decay through fluorescence, but at a longer time scale than fluorescence, known as delayed fluorescence (Fig. 3.25). Triplet-triplet annihilation occurs more often in a region of higher density of triplet states (e.g. proton tracks) which contribute to the tail of a voltage pulse measured in the photo-multiplier tubes. This ratio of the tail of the pulse to the total integral of the pulse is known as the pulse shape discrimination (PSD) parameter. This ratio helps distinguish between events with a small and large amount of triplet-triplet annihilation (e.g recoil electrons and recoil protons, respectively).

The timing contributions to the light output of the fluorescence and delayed fluorescence components are shown in Fig. 3.26. Each component of the pulse contributes to pulse shape discrimination shown in the lower plot in Fig. 3.26. The spontaneous
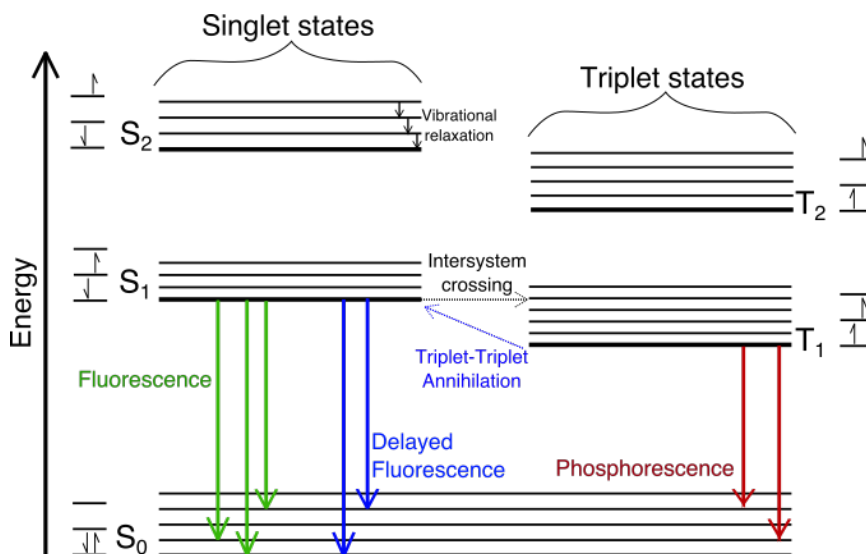
Figure 3.25: Jablonski diagram showing the excited singlet and triplet states

fission source, ^{252}Cf is useful to test the PSD capabilities of different scintillator mixtures because the fission process emits neutrons in addition to gamma rays emitted by the excited fission products. Figure 3.27 shows the PSD parameter as a function of total light output for a standard scintillator mixture, as described in Section 3.5.2.

Since PSD is a ratio of the tail of the pulse to the total, the longer tail events have a higher PSD parameter. These events are recoil protons from neutron interactions, and the lower PSD events are recoil electrons from gamma-ray interactions.

3.5.2 Liquid scintillator ingredients

Organic liquid scintillators typically have three components: solvent, initial fluor and wavelength shifter. The typical solvents used are generally aromatic compounds, which have characteristic planar benzene rings with alternating single and double bond structures. This molecular structure is essential for efficient energy transfer from the initial ionization track to detectable photons. The alternating single and double bonds create de-localized π-bond electrons that are out-of-the-plane of the molecule. This de-localization permits the electrons excited by ionizing particles to freely access excited singlet and triplet states, without losing energy to collective
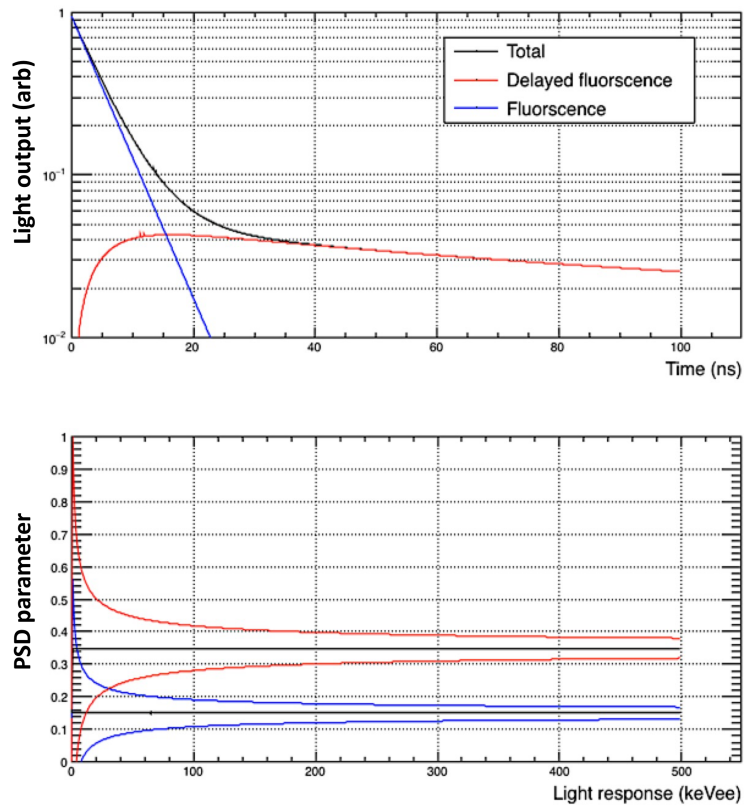
Figure 3.26: Diagram of the characteristic light output from an interaction within the scintillator. The total pulse is divided into the short and long components from fluorescence and delayed fluorescence that make up the entire pulse. Each component to the pulse is shown in the lower plot as its contribution to the pulse shape discrimination parameter.[Feb18b]
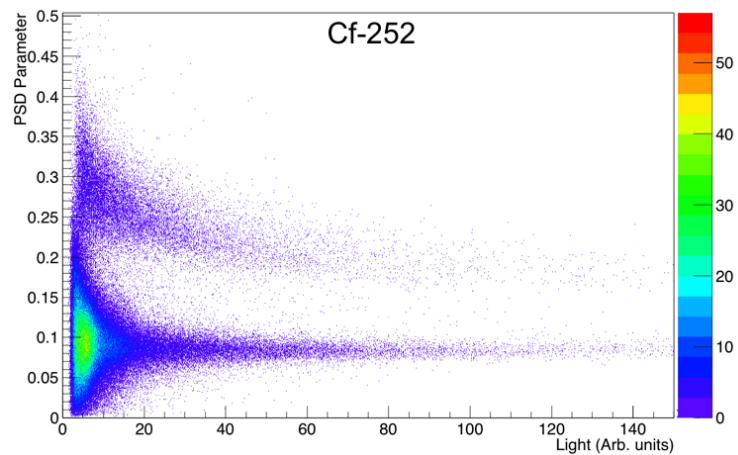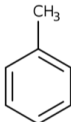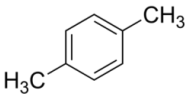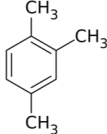
Figure 3.27: Pulse shape discrimination parameter as a function of total light output of a liquid scintillator. The band with the larger PSD parameter are proton recoil events from a neutron interaction. The lower band are electron recoil events from gamma ray interactions.

excitation modes of the entire molecule that produce heat. Some examples of solvents used are shown in Table 3.3.

Table 3.3: Physical properties of traditional solvents used for liquid scintillator solvents [Ran09]

solvent	compound	flash point [°C]	boiling point [°C]	density [g/mL]
toluene		4	110	0.865
p-xylene		25	138	0.861
1,2,4-trimethylbenzene		48	168	0.880

The mixture used in the SABRE array is based off of a standard recipe from Refs. [Hor70; Bir72], which contain 2,5-diphenyloxazole (PPO), 1,4-bis(5-phenyloxazol-2-yl) benzene (POPOP), and naphthalene with p-xylene as the solvent. The initial excitation energy caused from an ionizing particle track is transferred to the primary fluor, which in this case is 2,5-diphenyloxazole (PPO). The energy transfer mechanism is referred to as Förster Resonance Energy Transfer (FRET) [Kla09], where the electronic excitation states of the solvent and also naphthalene overlap with the absorption spectrum of the primary fluor, PPO (Fig. 3.28). Naphthalene is added in the mixture because it is known to enhance the pulse shape discrimination [Ver68]. The excited fluor de-excites via photon emission around 350 nm wavelength. The wavelength shifter 1,4-bis(5-phenyloxazol-2-yl) benzene (POPOP) absorbs photons in this wavelength and emits photons around 420 nm wavelength (Fig. 3.29), where the PMT is most sensitive [Nak10].

In order to maximize the detectable energy range of neutrons, the PSD threshold
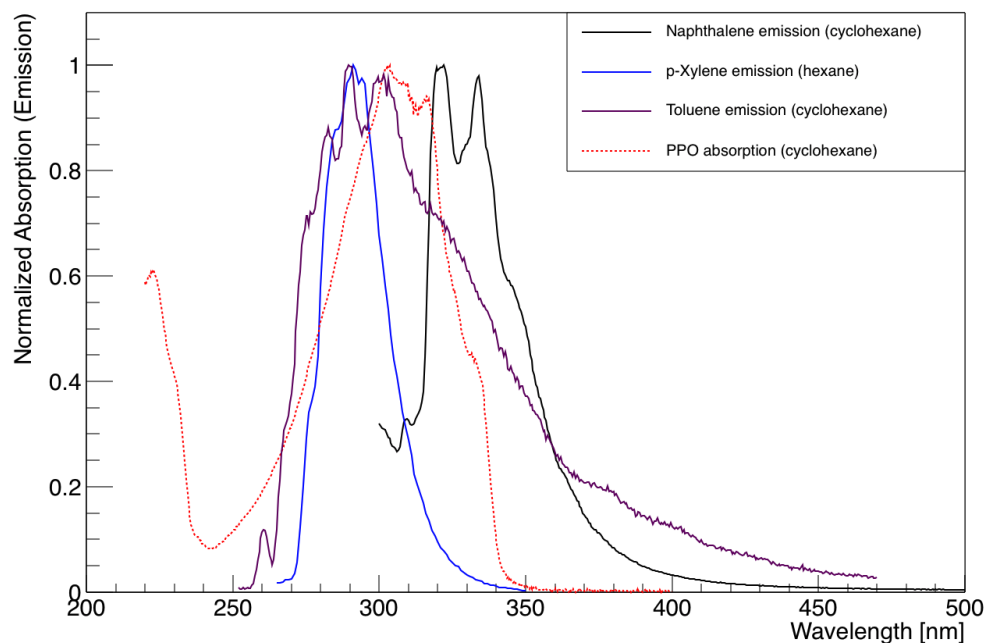
Figure 3.28: Overlap between the emission spectrum of the solvents p-xylene and toluene with the absorption spectra of PPO [Tan17]
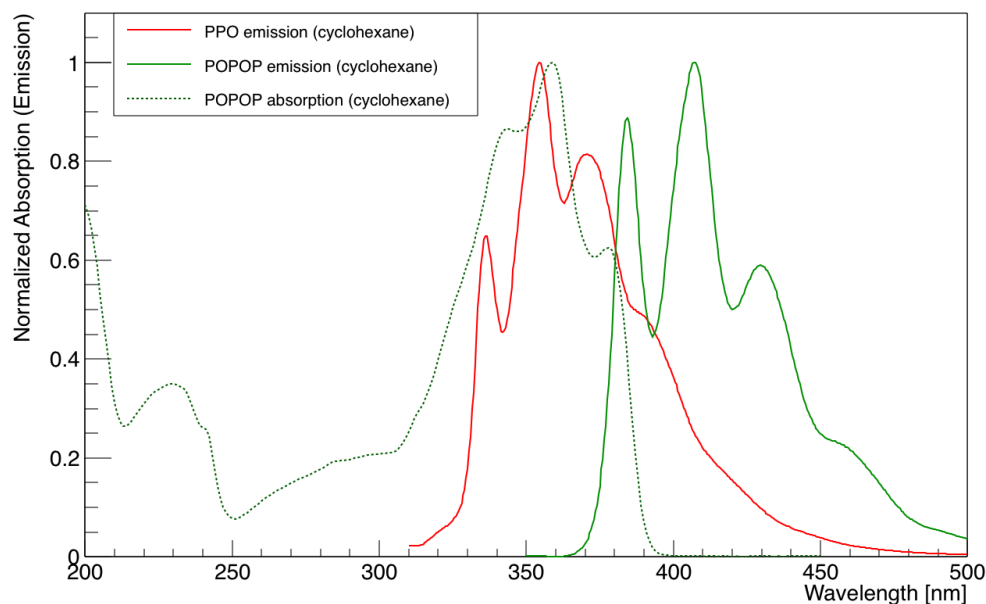
Figure 3.29: Emission spectra of the primary fluor PPO overlapping with the absorption spectrum of the wavelength shifter POPOP. Also the emission spectra of POPOP [Tan17]

to distinguish between gammas and neutrons at low incident neutron energies ($\sim$100 keV) can be improved by purification of the ingredients. Solvents, like p-xylene, can be distilled to remove contaminants like water. Other ingredients, like naphthalene, can be recrystallized in methanol and then further purified through sublimation [Arm13]. The effects of the purification can be seen in Figure 3.30.
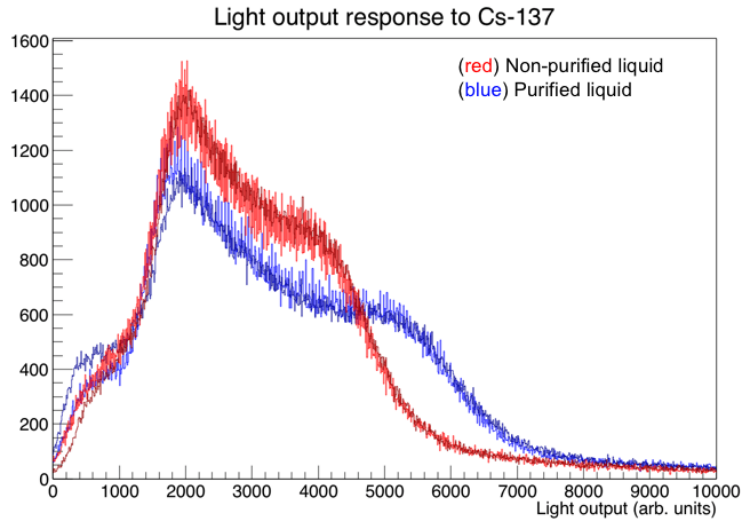
Figure 3.30: Comparison of the response to a ^{137}Cs source of un-purified and purified liquid scintillator mixtures

The Compton edge of gamma rays from the ^{137}Cs source shift to higher light output with the purified liquid scintillator. Figure 3.30 shows a higher light output for the same incident energy gamma ray (i.e. E_γ= 662 keV).

Chapter 4
$^{86}\mathbf{Kr}(d,p)^{87}\mathbf{Kr}$

In the present study, the (d,p) neutron-transfer reaction on ^{86}Kr is used to verify the combined method of extracting spectroscopic information in a mass region well suited for global optical models. ^{86}Kr has a closed N=50 neutron shell; therefore, the low-lying excitations in ^{87}Kr are expected to be single-neutron excitations. Also, global optical parameters have been well characterized in this mass region. The low-energy analysis is based on published studies of the ^{86}Kr(d,p) reaction in normal kinematics at 5.5 MeV/u by Haravu *et al*. [Har70]. This analysis was combined with a measurement of the (d,p) reaction with a 35 MeV/u ^{86}Kr beam at the National Superconducting Cyclotron Laboratory (NSCL) using the Oak Ridge Rutgers University Barrel Array (ORRUBA) coupled to the S800 magnetic spectrograph.

4.1   d(^{86}Kr,p)^{87}Kr at 35 MeV/u

The $d(^{86}$Kr$,p)^{87}$Kr reaction at 35 MeV/u was measured using inverse kinematics at the NSCL. An array of position-sensitive silicon strip detectors was coupled to the S800 magnetic spectrograph to measure charged particles in coincidence with heavy recoils. SIDAR (SIlicon Detector Array) [Bar01] and ORRUBA (Oak Ridge Rutgers University Barrel Array) [Pai09] were arranged as shown by the schematic in Fig. 4.1, and covered an angular range between 60° and 165° in the laboratory frame as shown by the ungated charged particle spectrum in Fig. 4.2. Elastically scattered products were detected at angles forward of 90° and were used for beam normalization. The

^{86}Kr beam impinged on a thin ($\sim$0.8 mg/cm^2) C$_2$D$_4$ foil. The ejectile protons of interest were detected at backward angles ($>90°$) in the laboratory in coincidence with heavy recoils in the S800.
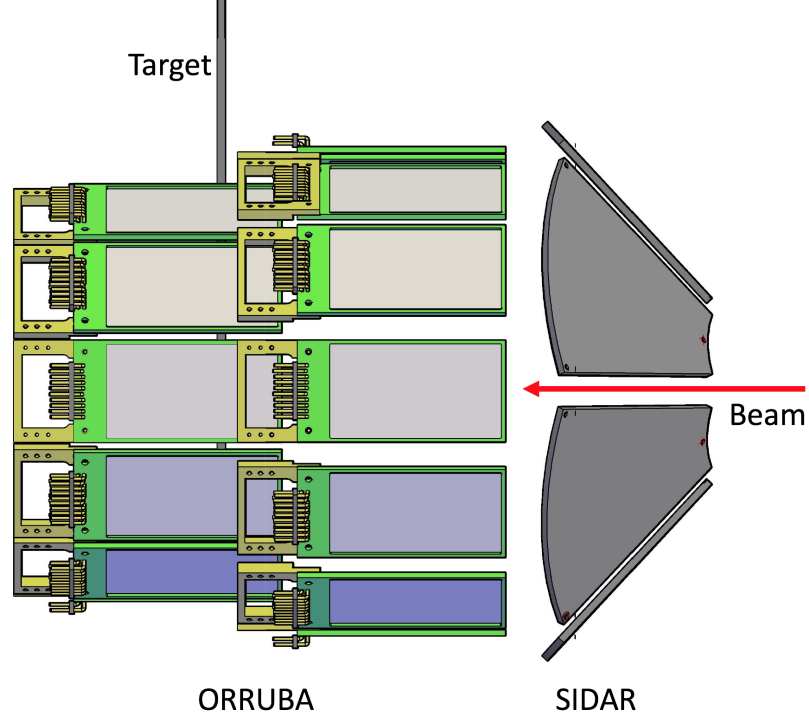
Figure 4.1: Schematic of ORRUBA and SIDAR arrays as configured for the measurement of the $d(^{86}$Kr,$p)^{87}$Kr reaction at 35 MeV/u at the NSCL.

The stable ^{86}Kr beam delivered from the cyclotron at 140 MeV/u was degraded in energy to 35 MeV/u with an average beam rate of $\sim 10^6$ pps. The total beam rate was limited by the acceptance rate of the S800. (d, p)-reaction protons of interest were detected at angles >90 degrees in the laboratory. The upstream and downstream ORRUBA barrels covered angles from 110° - 140° and 65° - 110°, respectively. The ORRUBA detectors are resistive-strip detectors with a position resolution of $\sim$1 mm, which in the current configuration is approximately $\sim 1°$ in the laboratory. SIDAR in a lampshade configuration consisted of 6 wedge-shaped annular detectors which covered angles between 150° - 170°. Each SIDAR detector has 16 strips with 5-mm pitch; in this configuration, each strip covered roughly $\sim$1.5° in the laboratory frame.

The detectors were calibrated using alpha particles from a ^{232}U source. The alpha particles from the calibration source were sufficiently energetic that ^{232}U daughter products exited the sealed source into the main scattering chamber. The resulting alpha decays were present during the experiment, as shown by the horizontal lines in Fig. 4.2. The data shown in Fig. 4.2 are only charged particle singles events detected in the silicon array, which is meant to show the angular coverage and particle energies; background events come from fusion evaporation of the beam and C_2D_4 target.
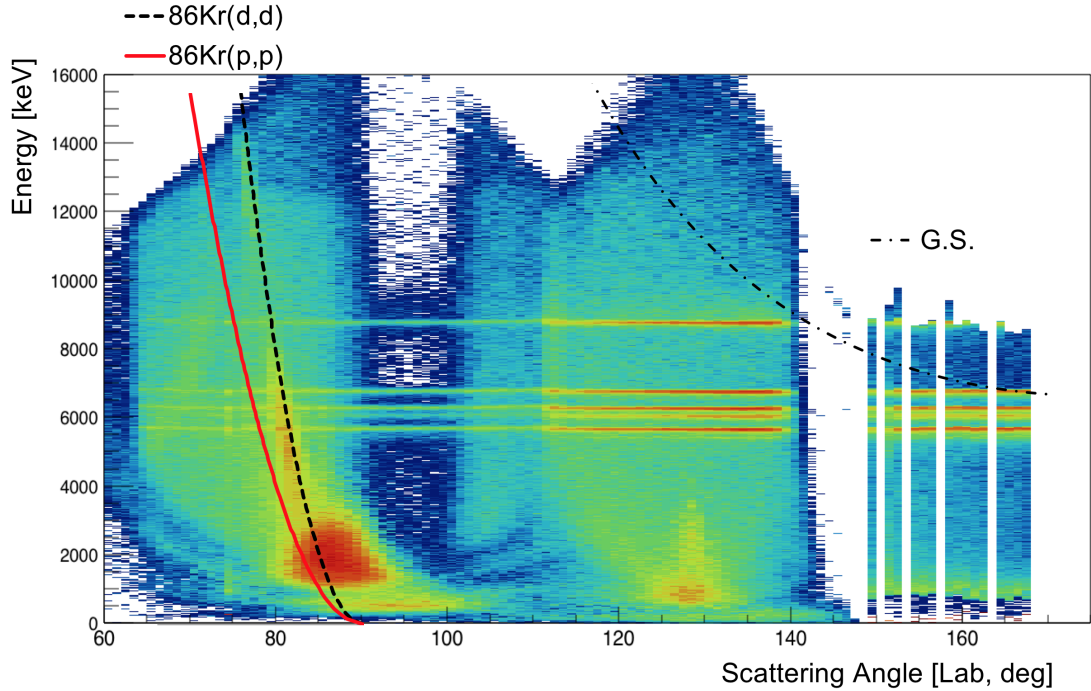
Figure 4.2: Particle energy as a function of laboratory angle for singles events in the silicon detector arrays. Overlayed lines are kinematics calculations for elastic scattering of deuterons and protons in the C_2D_4 target and for the population of the ground state in ^{87}Kr. The gap in data at 90° is shadow from the target ladder. Horizontal lines are from the daughter products from the ^{232}U calibration sealed source that contaminated the inner walls of the scattering chamber.

A challenge in the present measurement came from complications in merging two separate data acquisition systems during the experiment, namely the NSCLDAQ for the S800 and the NSCL version of the ASICs (Application Specific Integrated Circuits) system that was developed to handle a large number of readout channels by

collaborators at Washington University - St. Louis group [Eng07; Wal07]. As mentioned above, the alpha decays from the daughter products of the ^{232}U calibration source were visible throughout the experiment, which unfortunately overlapped the region where the ejectile protons from the (d, p) reaction would be observed at the most backward angles. The random alpha events should have been significantly suppressed by requiring coincidence events between the ejectile proton and the heavy recoil in the S800; however, due to the complications in merging the two data acquisition systems, the coincidence settings were shifted during the experiment which resulted in a significant loss of coincident events. This was due to a bug in the firmware of the VM-USB module that resulted in a complete hang of the system when specific numbers of words were dumped from the buffer, which was dynamically set depending on the number of channels reading out data during an event. The workaround during the experiment was to fix the number of words read out for each event, which had to be set to a large value to not miss any usable data from any channels. This quickly implemented workaround during the experiment turned out to be detrimental to the coincidence events with the S800 because the busy signal sent by the acquisition system is set by the amount of time needed to read out the large number of words, and the coincidence events were therefore vetoed. This bug in the firmware of the VM-USB module which caused the instabilities was found to be set by default in the NSCLDAQ readout code. Updated versions of the NSCLDAQ (>v10.2) do not have this setting as default and the VM-USB firmware has since been fixed.

Charged particle singles events were recorded during the entire experiment. Figure 4.3 shows a Q-value spectrum from a small subset of the data where reliable coincidence events between ORRUBA and the S800 were recorded.

The Q-value spectrum shown in Fig. 4.3 is fit for the states of ^{87}Kr at the energies adopted from Ref. [Har70]. The excitation energies of states in ^{87}Kr measured in
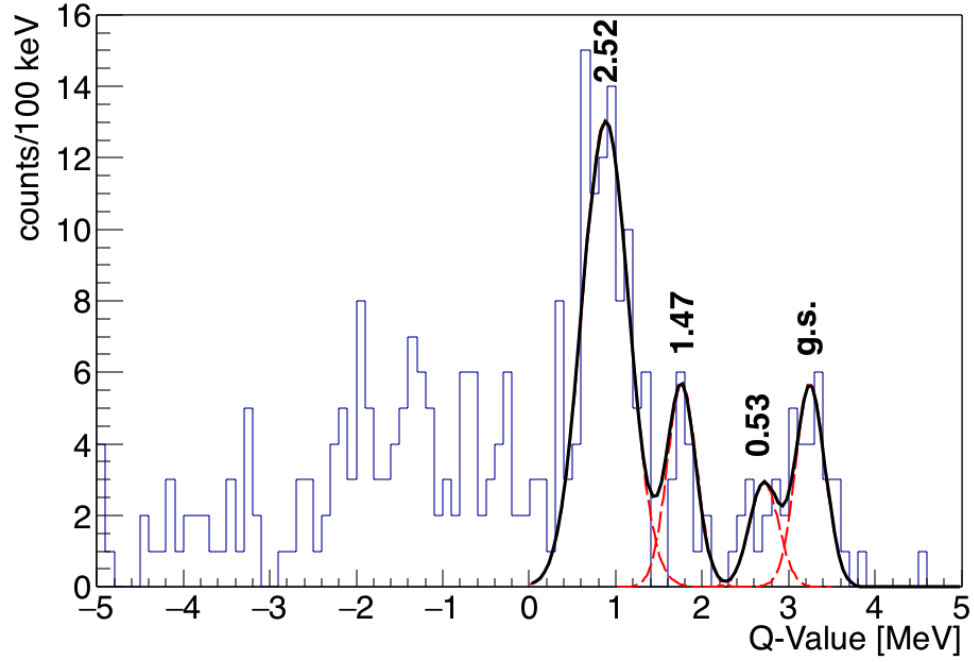
Figure 4.3: Q-value spectrum from a subset of the data. Ground state Q-value is 3.29 MeV. Excited state energies are labeled above the fitted peak. Background is mitigated by excluding the alpha contamination events as well as gating on coincidence events in the S800 magnetic spectrograph.

this work were consistent with those of previous measurements. The center of mass energy resolution is $\Delta E_{c.m.} \approx 400$ keV; therefore, the ground- and first-excited states (E_x=0.53 keV) are not well resolved. The energy resolution shown in Fig. 4.3 suffers from the beam spot size ($\sim$ 3mm), and the thickness of the target used (*e.g.* $\sim$0.8 mg/cm^2). The target thickness was chosen to mimic the conditions expected when using radioactive ion beams, with low beam intensities ($\sim$10^4-10^5 pps) and low cross sections ($<\approx$ mb).

The bulk of the data available for analysis were the charged-particle singles events, with no S800 heavy recoil gating that would have served to reduce background from fusion evaporation and the contaminant alphas. Therefore, the analysis was focused on the ground-state and 2.5 MeV excited state assumed to be the $7/2^+$ state observed in previous work [Har70; Sas65]. Differential cross sections were extracted for proton energies and angles where the alpha energies did not interfere and the fusion

evaporation background was sufficiently flat.

Angular distributions were extracted for the ground- and 2.5 MeV states (Fig. 4.4). Charged-particle counts for each excited state were summed in a given angular range. The (d, d) elastic scattering rate was used to ascertain the incident beam rate and normalize charged particle counts for a given angular bin. The incident beam rate can be extracted as a function of the (d, d) elastic scattering rate by using a cross calibration between different detectors in the A1900 Fragment Separator (see Fig. 3.1). First, (d, d) elastic scattering rate was compared to the rate seen by the XFP scintillator at the focal plane of the A1900. Since the XFP scintillator is rate limited, beam attenuators of 1000x and 10x were used separately for a two point cross calibration to the elastic scattering rate. Then, the rate was measured for the 36^+ charge state of the ^{86}Kr beam in the Z030 Faraday cup located upstream of the XFP scintillator for both the 10x and 1000x beam attenuators. The current reading in the Z030 Faraday cup was cross calibrated by using the reference rate measured in the XFP scintillator. This provided a two point conversion between the rate seen by the Z030 Faraday cup and the XFP scintillator and therefore the elastic scattering rate. The attenuators were then taken out, and the full beam current is measured in the Z030 Faraday cup. This total beam rate is then known as a function of (d, d) elastic scattering rate. The same cross-calibration procedure was performed multiple times during the experiment to ensure a correct conversion from elastic scattering rate to incident beam rate. The extracted cross sections were normalized using this elastic scattering rate. The extracted angular cross sections are shown in Fig. 4.4; the uncertainties in the cross sections shown are purely statistical.
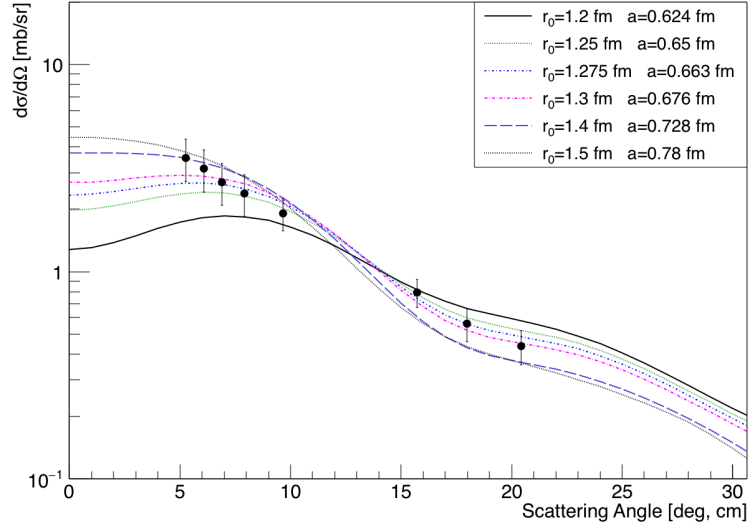
(a)
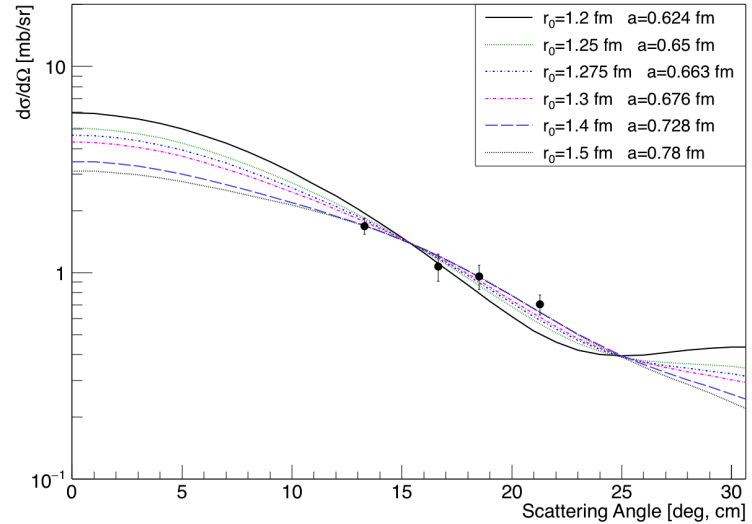
(b)

Figure 4.4: Differential cross sections as a function of center-of-mass angle for the (d, p) reaction with 35 MeV/u ^{86}Kr beams and compared to FR-ADWA calculations (lines) described in section 4.2. The theoretical cross sections for each (r_0, a) pair were scaled using a least squares fit to the data points to deduce S for each state. (a) $5/2^+$ ground state of ^{87}Kr (points). FR-ADWA calculations assume $\ell=2$, $2d_{5/2}$ transfer and varied radius and diffuseness parameters for the neutron bound state. (b) $7/2^+$ 2.5 MeV state of ^{87}Kr (points). FR-ADWA calculations assumed $\ell=4$, $1g_{7/2}$ transfer and varied radius and diffuseness parameters for the neutron bound state.

4.2   Analysis details

The Finite-Range ADiabatic Wave Approximation (FR-ADWA) [Joh74] was used to analyze the ^{86}Kr(d,p) reactions at both energies. This approach takes into account the breakup of the deuteron and has been shown to perform well for deuteron energies >10 MeV [Nun11]. Also, the finite range correction to ADWA has been shown to have significant effects on the calculated cross section, especially at higher beam energies (>20 MeV/u) [Ngu10], and therefore should be included in the reaction formalism in this analysis. Modern global optical parameterizations of Koning-Delaroche (KD) [Kon03] were used for the nucleon-target potential at both the low and high energy, together with the Reid soft-core potential [Rei68] for the nucleon-nucleon interaction. Optical model parameters used in this work are summarized in Table 2.3. The Chapel-Hill global parameterization [Var91] was also tested using ADWA to compare to the results using the more modern Koning-Delaroche parameterization. The neutron bound state parameters were varied over the range r_0= 1.2 - 1.5 fm and a= 0.624 - 0.78 fm to span single-particle ANCs (spANC) as shown in Table 4.1. The geometry of the real central interaction was also used for the bound state spin-orbit geometry. TWOFNR [Tos14] was used to generate the theoretical cross sections, which only introduces a finite-range correction. FRESCO [Tho88] was used to verify the calculated cross sections, which incorporates a full treatment of the finite-range transfer and was found to produce the same cross sections as TWOFNR in the angular range of interest; therefore the analysis was performed using only TWOFNR for ease of use. The same range of bound-state configurations, and therefore same spANC values, were used in the analysis of both the low- and high-energy measurements of the ^{86}Kr$(d,p)^{87}$Kr reaction. Table 4.1 summarizes the choice of bound-state parameters and the corresponding values for the single-particle ANC $b_{\ell j}$.

Table 4.1: Values of single-particle ANC, $b_{\ell j}$, for each choice of radius and diffuseness values for three final states in ^{87}Kr

r_0 [fm]	a [fm]	$b_{d5/2}$ [fm^{-1}] G.S.	$b_{s1/2}$ [fm^{-1}] Ex=0.53 MeV	$b_{g7/2}$ [fm^{-1}] Ex=2.52 MeV
1.2	0.624	5.35	11.06	0.134
1.225	0.637	5.70	11.62	0.146
1.25	0.65	6.08	11.90	0.158
1.275	0.663	6.45	12.83	0.172
1.3	0.676	6.90	13.48	0.185
1.325	0.689	7.35	14.16	0.200
1.35	0.702	7.82	14.87	0.216
1.375	0.715	8.32	15.62	0.233
1.4	0.728	8.85	16.41	0.251
1.45	0.754	10.0	18.10	0.290
1.5	0.78	11.27	19.96	0.334

4.3 Extracting the ANC: ^{86}Kr$(d, p)^{87}$Kr at 5.5 MeV/u

The ^{86}Kr(d, p) reaction was previously measured with 11 MeV deuteron beams. Angular distributions reported by Haravu *et al.* [Har70] were used to extract the nuclear ANC $C_{\ell j}$ and constrain the asymptotic behavior of the wavefunctions. This peripheral reaction was measured in normal kinematics with an 11 MeV deuteron beam impinging on a gas cell of 98.5% isotopically enriched ^{86}Kr gas at approximately 0.025 atm in pressure. Reaction protons were measured using two movable 2 mm thick lithium-drifted silicon detectors, cooled to dry-ice temperatures.

The 2d$_{5/2}$ ground-state and 1g$_{7/2}$ excited-state differential cross sections are shown in Figs. 4.5a and 4.5b, respectively. Each angular distribution is overlaid with FR-ADWA calculated cross sections for the different bound-state configurations as described in Table 4.1. To be consistent with the high energy analysis, each FR-ADWA calculated cross section was normalized to the data by a least squares minimization for center of mass (c.m.) angles <90°. The angular cutoff was chosen to constrain the region where ADWA is more robust (i.e. low center of mass angles, excluding higher order effects) and to provide a more stringent constraint to the data rather

than normalizing to the data in the first peak only.

Table 4.2 summarizes the extracted $C^2_{\ell j}$ values from the present FR-ADWA analysis for the ground- ($2d_{5/2}$), first-excited ($3s_{1/2}$) and 2.5-MeV ($1g_{7/2}$) states measured at 5.5 MeV/u in Ref. [Har70]. The spectroscopic factors reported in Ref. [Har70] were deduced from optical-model parameters based on a fit to elastic scattering and a traditional Distorted Wave Born Approximation (DWBA) approach, which does not account for deuteron breakup. The nuclear ANC $C_{\ell j}$ values in Table 4.2 for these states were deduced from the the present FR-ADWA analysis. Uncertainties come from the least squares fit to the data ($\sim$1 %), a total systematic error adopted from Ref. [Har70] (6%), and an assumed error for the FR-ADWA calculation (10%).

Table 4.2: Summary of spectroscopic properties of excitations in ^{87}Kr from the present analysis and the measurements by Haravu and collaborators at 5.5 MeV/u [Har70]. The excitation energies and J^π assignments are adopted values [Joh15]. Spectroscopic factors, S, from Ref. [Har70] as well as nuclear ANCs $C_{\ell j}{}^2$ from this work, are tabulated. Ref. [Har70] did not quote uncertainties on S values; typically $\sim$25% uncertainties come from DWBA calculations

E_x [MeV]	J^π	single-particle configuration	S [Har70]	$C_{\ell j}{}^2$ $[fm^{-1}]$
0.0	$5/2^+$	2d5/2	0.56	18(2)
0.53	$1/2^+$	3s1/2	0.46	89(10)
2.52	$7/2^+$	1g7/2	0.49	0.012(1)
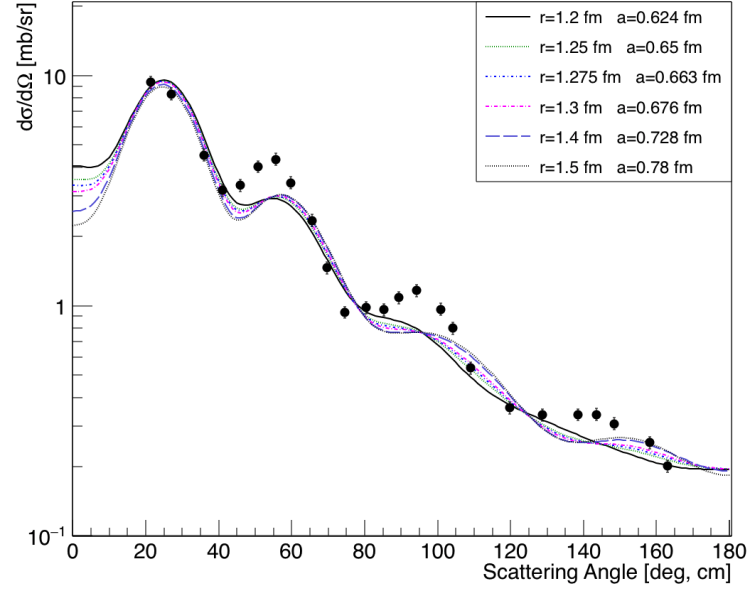
(a)
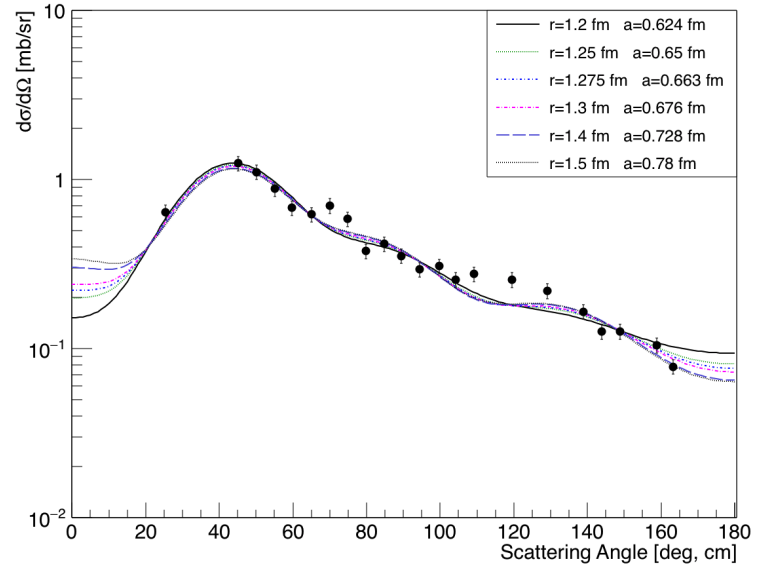
(b)

Figure 4.5: Differential cross sections from the 5.5 MeV/u ^{86}Kr(d,p) reaction measurement in Ref. [Har70] as a function of center of mass angle and compared to FR-ADWA calculations (lines). (a) $5/2^+$ ground state of ^{87}Kr (points). FR-ADWA calculations assume $\ell=2$, $2d_{5/2}$ transfer. (b) $7/2^+$ excited state of ^{87}Kr (points). FR-ADWA calculations assume $\ell=4$, $1g_{7/2}$ transfer. Each of the calculated cross sections varied parameters (r_0,a) for the neutron bound state. The theoretical cross section were scaled using a least squares fit to the data points for c.m. angles $<90°$ to deduce S for each (r_0,a) pair.

4.4 Determination of the spectroscopic factor from combined measurements

To constrain the bound-state potential and deduce spectroscopic factors with uncertainties dominated by experimental uncertainties, the following procedure was used. First, a spectroscopic factor was obtained through eq. 2.12 by normalizing the FR-ADWA prediction to the experimental cross section for each spANC $b_{\ell j}$ summarized in Table 4.1. The corresponding nuclear ANC ($C_{\ell j}$) was deduced from the relation in eq. 2.11. The results from the FR-ADWA analysis of both the low- and high-energy measurements for the extracted spectroscopic factors and nuclear ANCs for the ground state of ^{87}Kr are shown in Fig 4.6. For the low-energy results, the spectroscopic factor varies by about a factor of four as the bound-state potential geometry changes with increasing spANC. The ANC is relatively constant over the range of $b_{\ell j}$, consistent with the expectation that the reaction is peripheral at 5.5 MeV/u. In contrast, the ANC is not constant over the range of $b_{\ell j}$ for the higher energy results.

Since $C_{\ell j}$ and S are properties of a nuclear state, independent of the reaction by which they are determined, the correct bound-state potential geometry should yield consistent $C_{\ell j}$ and S values from measurements at different energies. Therefore, the crossing in Fig. 4.6 constrains the single-particle ANC to $b_{2d5/2}$=6.46 $^{+1.12}_{-0.57}$ fm. Adopting these values for the bound-state configuration for the ground-state reaction yields a spectroscopic factor of S=0.44 $^{+0.09}_{-0.13}$, where the uncertainty comes from the least squares fit to the data ($\sim$7 %), a total systematic uncertainty of 10% in normalization across all $d\sigma/d\Omega$ data points (e.g. target thickness, beam normalization) and an estimated uncertainty for the FR-ADWA calculation (10%) for the reliability of the theory. Assuming the initial chosen set of bound-state parameters, (r_0, a), from Table 4.1, the constrained spANC corresponds to r_0=1.27 $^{+0.07}_{-0.04}$ fm and a=0.66 $^{+0.04}_{-0.02}$ fm,

which are similar to the typical adopted values of r_0=1.25 fm and a=0.65 fm. However, as will be discussed later in this section, the spANC does not correspond to a unique set of radius and diffuesness parameters.

(a) (b)
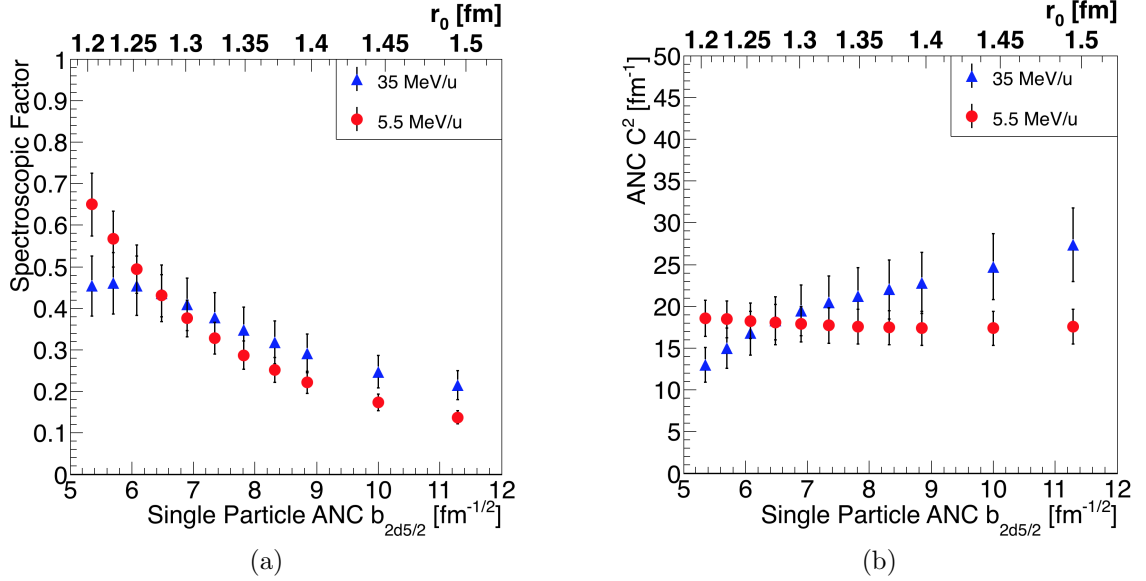
Figure 4.6: Results from the FR-ADWA analysis with KD optical model parameters for the ^{87}Kr ground-state measurements at 5.5 MeV/u (red) and 35 MeV/u (blue). (a) Spectroscopic factors as a function of single-particle ANC $b_{\ell j}$. (b) Nuclear ANC $C^2_{\ell j}$ values as a function of single-particle ANC $b_{\ell j}$. Error bars represent systematic uncertainties, uncertainty in FR-ADWA calculation, and also least squares fit to data with statistical uncertainties.

The global optical model parameterization of Chapel-Hill [Var91] was also used in order to confirm this constrained region for the single-particle ANC. The constrained value for the spANC using Chapel-Hill is listed for a comparison to the value using Koning-Delaroche in Table 4.3.

Table 4.3: Comparison of global optical models Koning-Delaroche and Chapel-Hill for the constrained single-particle ANC for the ground state reaction of ^{86}Kr$(d, p)^{87}$Kr

Global optical model	$b_{d5/2}$ [fm^{-1}]
Koning-Delaroche [Kon03]	6.46 $^{+1.12}_{-0.57}$
Chapel-Hill [Var91]	6.70 $^{+1.30}_{-0.63}$

Figure 4.7 summarizes the results for the dependences of both $C_{\ell j}$ and S as a
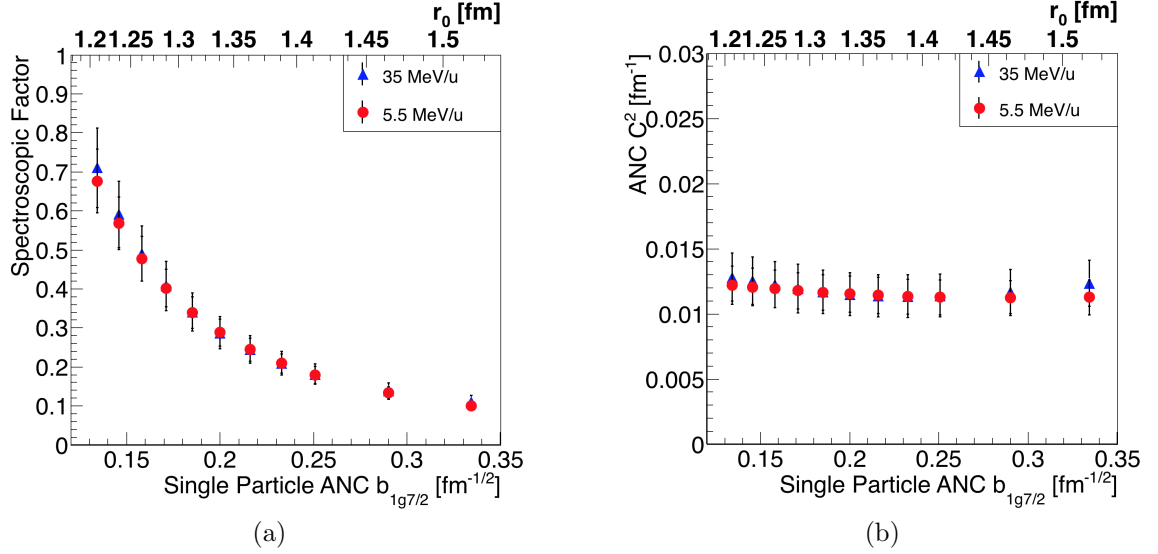
Figure 4.7: Results from the FR-ADWA analysis of the ^{87}Kr 2.5 MeV $1g_{7/2}$ state measurements at 5.5 MeV/u (red) and 35 MeV/u (blue). (a) Spectroscopic factors as a function of single-particle ANC $b_{\ell j}$. (b) Nuclear ANC $C_{\ell j}^2$ values as a function of single-particle ANC $b_{\ell j}$. Error bars represent systematic uncertainties, uncertainty in FR-ADWA calculation, and also least squares fit to data with statistical uncertainties.

function of $b_{\ell j}$ for the excited state at E=2.5 MeV, where an $\ell=4$, 1g7/2 transfer is assumed, based on previous studies. In contrast to the results for the ground-state $\ell=2$ transfer, both the low and higher energy measurements yield statistically identical results, including a relatively flat $C_{\ell j}$ which is a signature of a peripheral reaction even at 35 MeV/u. The apparent peripheral nature of the $\ell=4$ transfer in the NSCL data could be attributed to the larger angular momentum transfer, indicating that the centrifugal barrier has a significant effect, even at these higher energies. Also, the measured differential cross section covers only a small angular range, where the shapes of the FR-ADWA predictions for different (r_0,a) pairs are relatively similar. Data at smaller ($<10°$) and/or larger ($>25°$) c.m. angles, where the shapes of the FR-ADWA predictions are more distinctive for different (r_0,a) values, may have provided more constraint on the normalization of the ADWA curve and hence more significant differences in S as a function of (r_0,a) in the higher energy data and therefore a constraint on the bound-state potential. The spectroscopic factor for the 2.5 MeV

state in Table 4.4 was, therefore, calculated assuming the r_0 and a values deduced from the ground state. Ideally, a constrained region for the spANC is desired for every excited state because the effective mean field is not necessarily the same for different states if there are strong correlations.

Table 4.4: Summary of spectroscopic factors for the ground state and excited $J^\pi=7/2^+$ state of $^{86}Kr(d,p)^{87}Kr$ from the present analysis and previous measurements at lower beam energies.

Reference	Energy [MeV/u]	$S_{d5/2}$ (g.s)	$S_{g7/2}$ (E_x=2.5 MeV)
[Har70]	5.5	0.56	0.49
[Sas65]	7.5	0.66	-
[Sha13]	10	0.63 ± 0.16^a	0.58 ± 0.15^b
This work	35	$0.44^{+0.09}_{-0.13}$	$0.41^{+0.08}_{-0.12}$

[a]Adopted from the normalization factor for $J^\pi=5/2^+$
[b]Adopted from the normalization factor for $\ell=4$ transitions

The extracted spectroscopic factors are compared to previous measurements at different beam energies in Table 4.4. The values extracted from the present work are consistently lower than previous results, although Refs. [Har70; Sas65] did not quote uncertainties. The source of this discrepancy may be enshrouded in the number of differences between DWBA and ADWA. The beam energy in Ref. [Har70] is very close to the low-energy regime of ADWA (>10 MeV) as shown by Nunes and Del-tuva [Nun11], and therefore the ADWA analysis for the low-energy data may not be optimal. Pang *et al.* [Pan14] suggested this could be due to flaws in the treatment of the nuclear interior in the nuclear reaction theory. Bailey *et al.* [Bai16] pointed out the importance of introducing non-locality in the interaction potentials, which has been the focus of recent work in direct reaction theory (e.g. Refs. [Ros15; Tit16; Lov17]). Following the study by Bailey *et al.* [Bai16], Gómez-Ramos and Timo-feyuk [Góm18] compared ADWA to CDCC to point out the uncertainties with the adiabatic approximation. Although their focus was on nonlocal potentials, the authors of Ref. [Góm18] were able to show that ADWA consistently predicted larger

cross sections when using the Reid Soft-core description of the deuteron, as was used in the current analysis. The over-prediction was shown to have a greater effect at higher beam energies (E_d^{lab}=50 MeV), resulting in lower spectroscopic factors.

With all of these potential sources of uncertainty, it is striking that the previous analyses which have not constrained the asymptotic part of the wavefunction, extracted values that are not very far from those extracted in this work. It should also be noted that typical uncertainties attributed to DWBA calculations can be of the order of 20%-30% (*e.g.* Ref. [Tho07]).

The set of (r_0, a) values was chosen to span the single-particle ANC around realistic values for the radius and diffuseness. However, as mentioned previously, the value for the single-particle ANC is not unique to a given (r_0, a) pair. There are many combinations of (r_0, a) that can produce the same spANC values. Therefore, the combined method is not constraining a unique value for the radius and diffuessness parameters, rather a value for the single-particle ANC only. In order to illustrate this distinction, the original set of (r_0, a) pairs was expanded to span a larger parameter space. The radius parameter values were expanded to the range, r_0=0.1 - 2.0 fm in steps of 0.1 fm, and the diffuseness parameter was expanded to the range a=0.2 - 1.2 fm in steps of 0.1 fm. The method remains the same in that each calculated cross section is normalized to the experimental data to extract a spectroscopic factor for both the low- and high-energy data. Figure 4.8 shows the extracted spectroscopic factor and corresponding nuclear ANC as a function of a large range of (r_0, a) values, constrained to a more physical region (r_0=1.0 - 2.0 fm and a=0.4 - 0.9 fm). The original set of parameters from Table 4.1 are shown as the points overlayed on the surfaces. The region where the two surfaces cross would be the constrained region of spANC for the large range of (r_0, a) values. The crossing of the two surfaces is shown by the line in Fig. 4.8, indicating the range of (r_0, a) that provide a consistent analysis of both the high and low energy data.
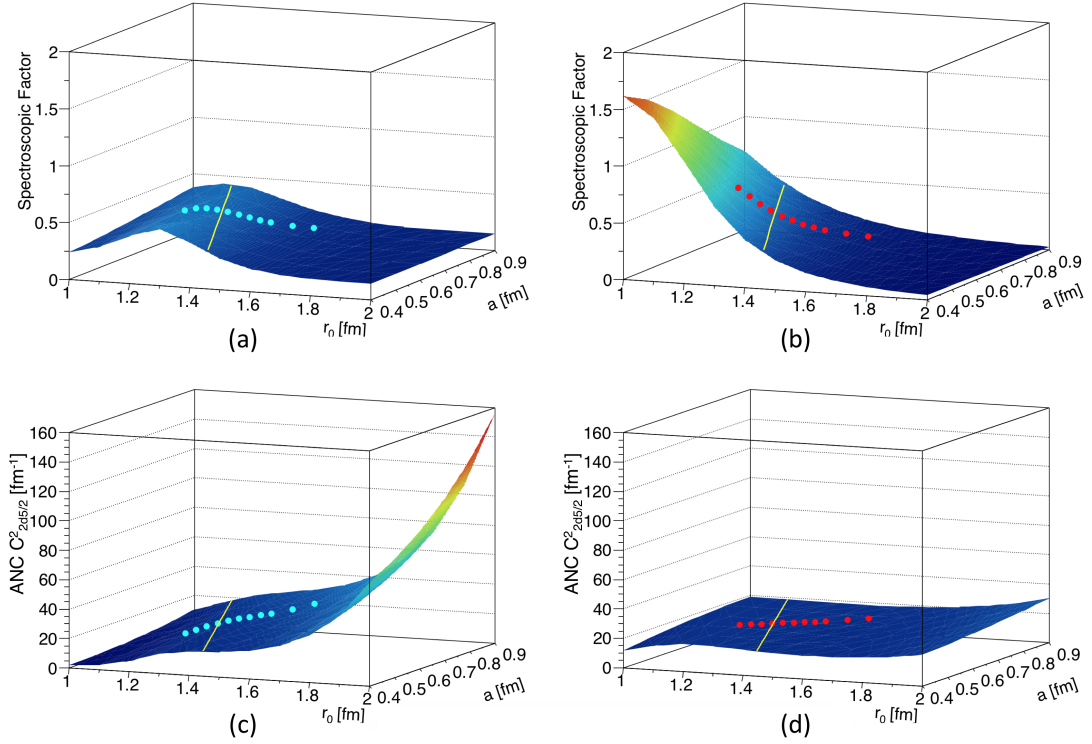
Figure 4.8: Spectroscopic factor and ANC, C^2, surfaces as function of both radius and diffuseness parameters for the ground state reaction of ^{86}Kr$(d, p)^{87}$Kr. (a) and (b) show the extracted spectroscopic factor from the high- and low-energy analyses, respectively. (c) and (d) are the extracted ANC from the high- and low-energy analyses, respectively. Points overlayed are the initial chosen set of parameters summarized in Table 4.1. Line on each plot marks where the low- and high-energy surfaces cross.

The crossing region is shown in a different parameter space by the shaded band in Fig. 4.9 in order to highlight the value for the constrained spANC. The uncertainty shown is produced by shifting the high-energy surface $\pm 10\%$, based on the assumed uncertainty for the FR-ADWA calculation, which is the dominant uncertainty. The total uncertainty would therefore be larger, as shown by the error bars on the constrained spANC value from this work using the parameters from Table 4.1.

Figure 4.9 shows the spANC as a function of the radius parameter r_0, overlayed with lines of constant diffuseness, a. The constrained value for the spANC extracted from the original set of parameters in Table 4.1 is shown, along with the region where the surfaces cross from Fig. 4.8. The crossing region of the surfaces confirms that the
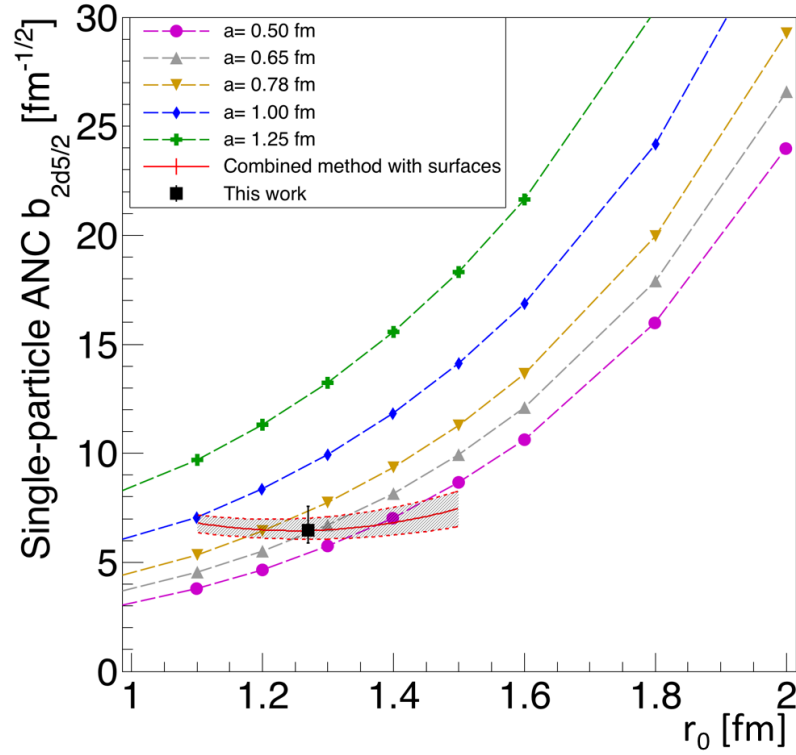
Figure 4.9: Single-particle ANC as a function of radius parameter overlayed with lines of constant diffuseness. Shaded region is combined method constrained region from the surface crossings with 10% uncertainty bands

combined method does constrain a value for the single-particle ANC, but there are many choices of (r_0, a) that lie within this constrained region.

The same result is also shown in a different parameter space in Fig. 4.10 to better show the values of (r_0, a) that produce the constrained spANC region. The point with the error box represents the constrained region from the original parameter set (Table 4.1) corresponding to $b_{2d5/2}=6.46 \, ^{+1.12}_{-0.57}$ fm, which when using this uncertainty and values from the original parameter set correspond to $r_0=1.27 \, ^{+0.07}_{-0.04}$ fm and $a=0.66 \, ^{+0.04}_{-0.02}$ fm when r_0 and a are scaled proportionally together. It is noteworthy that these parameter values are in good agreement with the canonical values of $r_0= 1.25$ fm and $a= 0.65$ fm. An additional scattering measurement (*e.g* total cross section and electron scattering [Tsu17]) would be required in order to precisely measure the actual values for the radius and diffuseness parameters, which should be
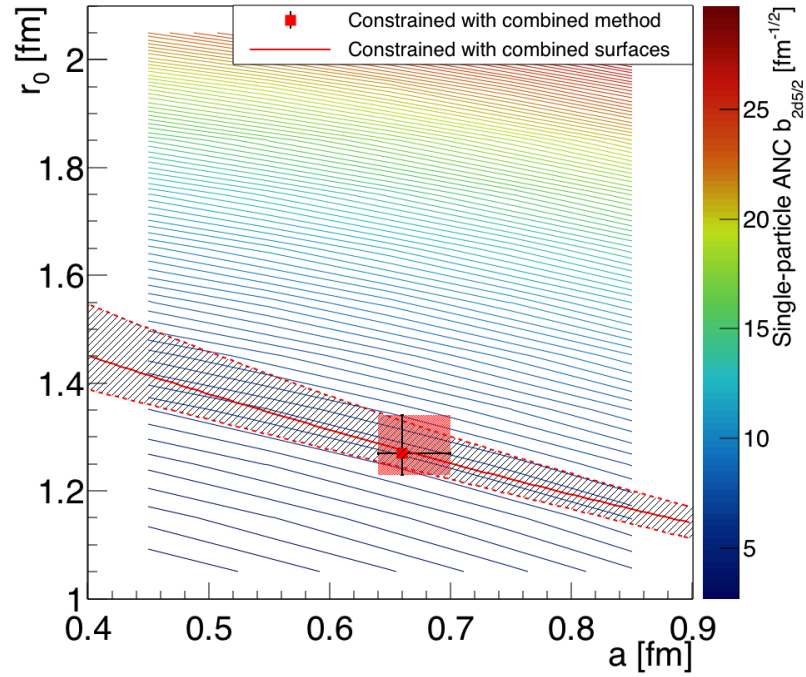
Figure 4.10: Single-particle ANC contours as a function of radius and diffuesness parameters overlayed with the initial chosen set of (r_0, a) pairs. Shaded region is combined method constrained region from the surface crossings with 10% uncertainty bands.

consistent with the constrained region of single-particle ANC extracted in this work.

Another interesting comparison is how well the theoretically calculated differential cross section fits the data using a χ^2 analysis. At higher energy, the bound-state potential affects both the magnitude and the shape of the differential cross section $(d\sigma/d\Omega)$ as can be seen in Fig. 4.4. Under the assumption that the optical model is correct, the shape of $d\sigma/d\Omega$ (reflected in the minimum χ^2 for each (r_0, a)) should reflect the shape of the bound-state potential. The χ^2 surface is calculated for the higher energy data set for the entire range of (r_0, a) from Fig. 4.8, and is shown in Fig. 4.11. The overlayed line is the approximate surface crossing from the combined method using the surfaces, and the point corresponds to the original constrained value for the (r_0, a) pair using the original parameter set from Table 4.1.

Interestingly, the surface crossing line falls within a valley of the χ^2 values suggesting that the calculated cross sections fit the measured data well, within a physical
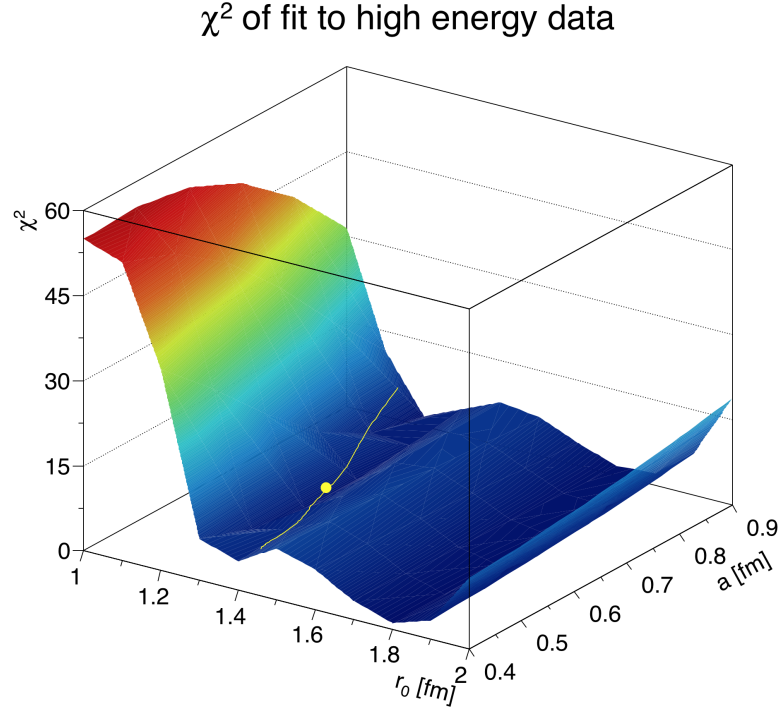
Figure 4.11: χ^2 fit to the data from the $d(^{86}\text{Kr},p)^{87}\text{Kr}$ reaction at 35 MeV/u. Yellow line shows the combined method constrained region of (r_0, a) deduced from the crossing of the surfaces in Fig. 4.8. The point is the crossing point from the combined method analysis using the original set of (r_0, a) shown in Table 4.1, and corresponds to $\chi^2 = 2.5$.

region of r_0 and a values. Though only tentative conclusions can be drawn from this, it is gratifying that the optimal region of (r_0, a) from both χ^2 and the combined method are compatable. Similar to the previous plots, the crossing point from the original (r_0, a) pairs is shown by the point in Fig. 4.11. There is another valley in the χ^2 surface at around r_0=1.8 fm. This is in an unphysical region, but is interesting how the cross section is a better fit to the data in this region. An example of the fits to the data from each of the mimimum χ^2 regions are shown in Fig 4.12. Other independent measurements of the nuclear radius (*e.g.* electron scattering) could confirm that the value for $r_0 \sim 1.8$ fm is completely unphysical in this mass region near stability.
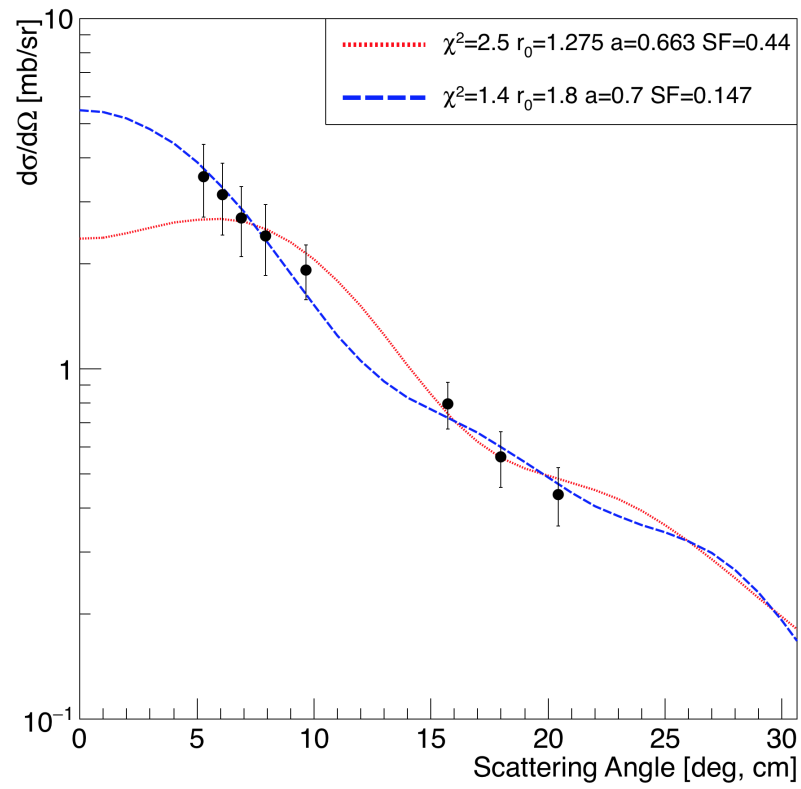
Figure 4.12: Example fits to the ground state of ^{87}Kr in valleys of the χ^2 surface from Fig. 4.11.

Chapter 5

$d(^{84}\mathbf{Se},p)^{85}\mathbf{Se}$

This chapter will discuss the $d(^{84}\text{Se}, p)\ ^{85}\text{Se}$ reaction used to test the combined method for radioactive nuclei in a similar mass region to the previous test with ^{86}Kr. The low-energy analysis, used to extract the many-body ANC, is completed using previously published results at 4.5 MeV/u. Only the experiment preparations and preliminary results will be shown for the high-energy measurement at 45 MeV/u that was completed in December 2017 and will be part of the dissertation of another student.

5.1   Extracting the ANC: $d(^{84}\mathbf{Se}, p)^{85}\mathbf{Se}$ at 4.5 MeV/u

The 4.5 MeV/u reaction was completed at the Holifield Radioactive Ion Beam Facility at Oak Ridge National Laboratory by Thomas *et al.* [Tho07], and was the first experiment to measure the (d, p) neutron transfer reaction on the radioactive nucleus ^{84}Se. Ref. [Tho07] extracted the many-body ANC, $\text{C}_{\ell j}$, for low lying states in ^{85}Se using the standard DWBA approach. In order to be consistent with the results obtained in Chapter 4, the differential cross sections are re-analyzed using the FR-ADWA approach with global optical parameterizations. The results of the current ANC analysis are summarized in Table 5.1, and compared to the previous values. The spectroscopic factors extracted by Thomas *et al.* [Tho07] assumed a neutron bound-state potential with r_0=1.25 fm and a=0.65 fm; therefore, the spectroscopic factors from this work presented in Table 5.1 assumed the same bound-state parameters for comparison.

Table 5.1: Summary of spectroscopic properties of excitations in ^{85}Se from the low-energy analysis and measurements by Thomas and collaborators at 4.5 MeV/u. The excitation energies and J$^\pi$ assignments are adopted values [Joh15]. Spectroscopic factors, S, and ANCs, $C_{\ell j}{}^2$ from Ref. [Tho07] and from this work are shown, S was calculated using the traditional r_0=1.25 fm and a=0.65 fm for the neutron bound-state potential.

		[Tho07]		This work	
E$_x$ [MeV]	J$^\pi$	S	$C_{\ell j}{}^2$ $[fm^{-1}]$	S	$C_{\ell j}{}^2$ $[fm^{-1}]$
0.0	5/2$^+$	0.33±0.10	6.11±1.43	0.19±0.06	3.3±1.0
0.462	1/2$^+$	0.30±0.09	25.3±5.9	0.17±0.05	14.4±4.3
1.115	(7/2$^+$)	0.77±0.27	0.049±0.012	0.93±0.28	0.040±0.012

The many-body ANC values are extracted using the same differential cross sections as measured by Thomas *et al.* The only difference is in using the traditional DWBA formalism (Ref. [Tho07]) and the more modern FR-ADWA formalism (this work). There is almost a factor of two difference in both the values for the ground- and first-excited states between DWBA and FR-ADWA. Figure 5.1 shows the measured differential cross sections from Ref [Tho07] for these two states compared to calculations.

The overall shape of the calculated cross sections between DWBA and ADWA look very similar; however, it is clear from the extracted ANCs in Table 5.1 that the overall normalization is very different. Similar to the results presented in section 4.4, the ADWA calculated cross sections predict a very large cross section for each of the states in Fig. 5.1, and therefore predict very low spectroscopic factors and ANCs when compared to the measured cross section.

In contrast to the extracted ANC values for the ground and first-excited states, the ANC extracted for the excited state at Ex=1.115 MeV that is assumed to be the J^π=7/2$^+$ state is very similar when extracted using DWBA vs. FR-ADWA. However, the data in Ref. [Tho07] only measured small center of mass angles where DWBA and ADWA predictions are similar. The DWBA and ADWA predictions diverge significantly at larger center of mass angles as shown in Fig. 5.2.

The measured cross section from Ref. [Tho07] only covers a small angular range in center of mass, where the two theoretical predictions are very similar. The measured data does not cover the predicted angular range of the first peak in the distribution and therefore, the normalization to the data yields similar values for the ANC. As was stated in the previous case, the FR-ADWA calculated cross sections are much larger than from DWBA predictions at this low beam energy.

Similar to the discussion in section 4.4, the current analysis shows that ADWA differs greatly from DWBA at the equivalent of deuteron beam energies of 9 MeV. In order to highlight some of the differences between different optical models for both DWBA and ADWA with this reaction, Fig. 5.3a shows a few calculations for the ground state reaction of ^{84}Se$(d,p)^{85}$Se assuming unit spectroscopic factors. The ADWA calculated cross sections shown in Fig. 5.3a predict a much larger cross section than DWBA at a beam energy of 4.5 MeV/u. Figure 5.3b shows the same global optical model calculations as shown in Figure 5.3a, but for a beam energy of 45 MeV/u. In contrast to the low beam energy counterpart, the ADWA calculations predict lower cross sections than DWBA at the peak of each distribution.

The lower cross sections predicted by ADWA could be attributed to the treatment of the breakup of the deuteron. It is expected that at higher beam energies, the deuteron breakup plays a larger role in the reaction and DWBA fails to address this aspect of the reaction. It is therefore essential that the $d(^{84}$Se$,p)^{85}$Se reaction be measured at an energy greater than 4.5 MeV/u in order to address the discrepancies between DWBA and ADWA for this reaction. Extracting a spectroscopic factor that is consistent with the ANC extracted with the peripheral measurement will shed some light on these discrepancies.
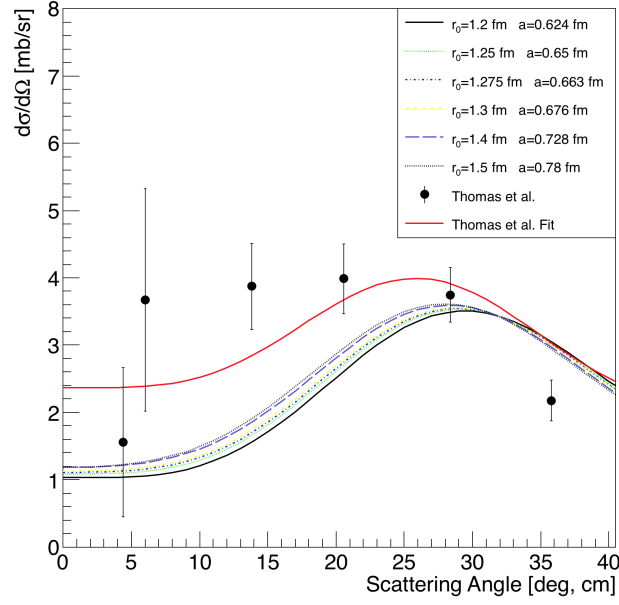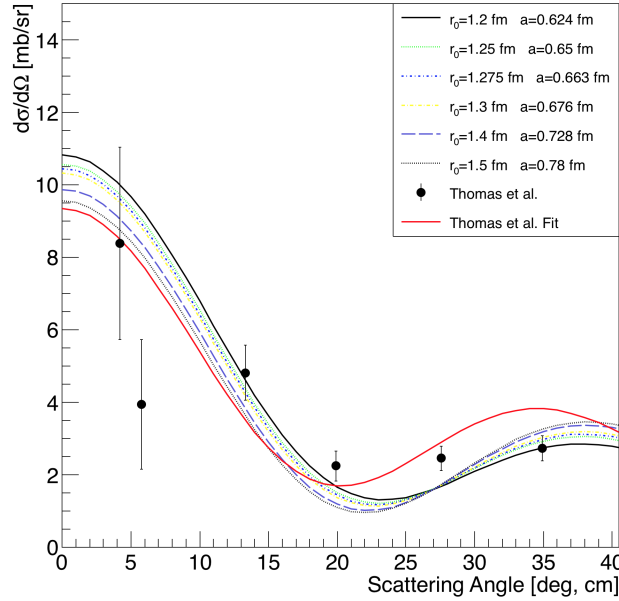
Figure 5.1: Differential cross sections from the 4.5 MeV/u ^{84}Se(d,p) reaction measurement in Ref. [Tho07] as a function of center of mass angle and compared to calculations (lines). Only the red line (Thomas *et al.* Fit) is calculated using DWBA, all other lines are using FR-ADWA. (a) $5/2^+$ ground state of ^{85}Se (points). FR-ADWA calculations assume $\ell=2$, $2d_{5/2}$ transfer. (b) $1/2^+$ first excited state of ^{85}Se (points). FR-ADWA calculations assume $\ell=0$, $3s_{1/2}$ transfer. Each of the calculated cross sections varied parameters (r_0,a) for the neutron bound state. Error bars represent statistical uncertainties.
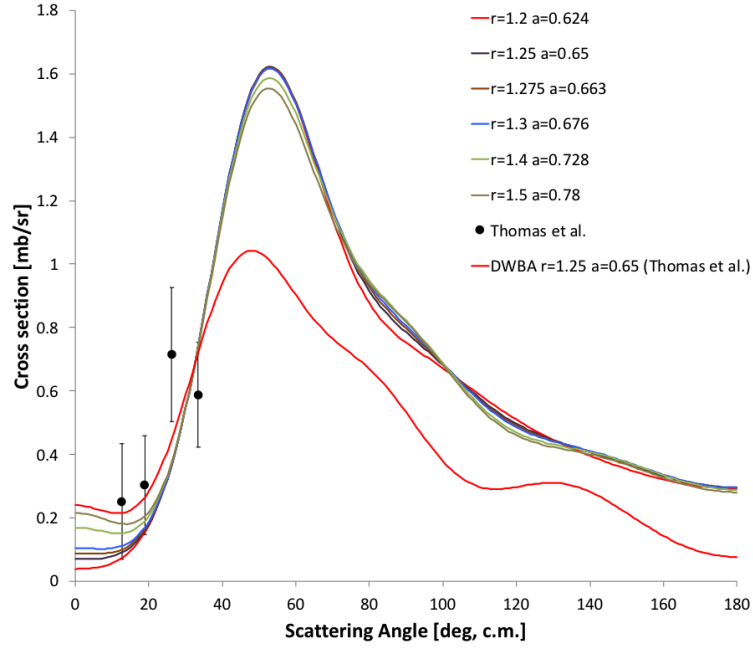
Figure 5.2: Differential cross sections from the 4.5 MeV/u ^{84}Se(d, p) reaction measurement in Ref. [Tho07] as a function of center of mass angle and compared to calculations (lines). Only the red line (Thomas *et al.* Fit) is calculated using DWBA; all other lines are using FR-ADWA. $7/2^+$ excited state at Ex=1.115 MeV of ^{85}Se (points). FR-ADWA calculations assume ℓ=4, $1g_{7/2}$ transfer. Each of the calculated cross sections varied parameters (r_0,a) for the neutron bound state. Error bars represent statistical uncertainties.
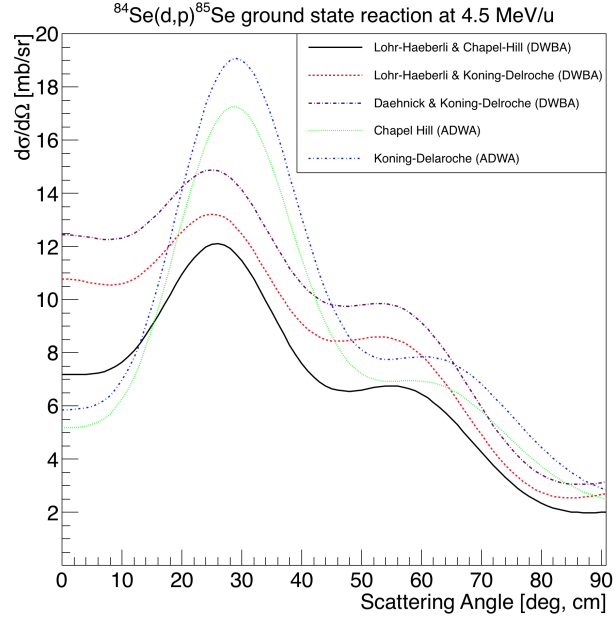
(a)
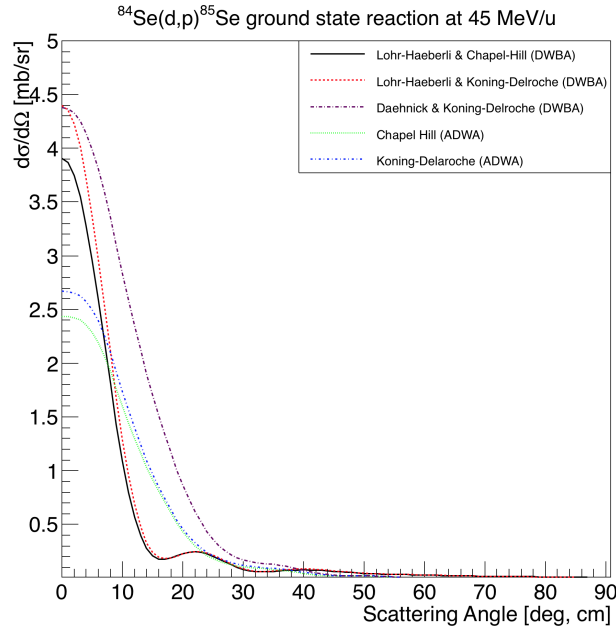
(b)

Figure 5.3: Comparison of global optical models for the ground state reaction of ^{84}Se$(d,p)^{85}$Se at (a) 4.5 MeV/u and (b) 45 MeV/u assuming $S{=}1$. Each DWBA calculation shows the model used for the entrance and exit channel of the reaction. The ADWA calculated cross sections use the treatment of Johnson and Tandy [Joh74], along with the shown global optical model to build the adiabatic potentials

5.2 $d(^{84}\mathrm{Se}, p)^{85}\mathrm{Se}$ at 45 MeV/u

The $d(^{84}\mathrm{Se}, p)^{85}\mathrm{Se}$ was measured at the NSCL with 45 MeV/u beams in December 2017. The protons of interest were measured by the ORRUBA and SIDAR detector arrays and the detectors were configured for this experiment as displayed in Fig. 5.5. Heavy recoils were detected in coincidence using the S800 magnetic spectrograph. One of the major challenges of (d, p) reactions with fast beams is the ejectile proton energies rapidly change with laboratory angle. The reaction performed using inverse kinematics will produce the ejectile protons with the lowest energies at the most backward angles in the laboratory (180°) and will rapidly increase in energy towards 90°. Sufficient thickness of silicon is needed to stop the ejectile proton in order to measure the total energy. Therefore, it is advantageous to place the silicon detector arrays at angles where the proton energies are sufficiently low to stop the protons in the detector. Figure 5.4 shows a kinematics calculation of the expected proton energies as a function of laboratory angle for the population of the ground state and also a state at the neutron separation energy of $^{85}\mathrm{Se}$.

The shaded boxes in Fig. 5.4 indicate the approximate angular coverage of the detector arrays ORRUBA and SIDAR. The height of the shaded boxes indicate the approximate proton energy that will punch through the thickness of silicon (See Fig. 5.5). Each SIDAR detector consisted of a stack of detectors with front layer (dE) $\sim 60\mu$m and back layer (E) $\sim 1000\mu$m. The same thicknesses were used for the most upstream barrel of ORRUBA, which is able to stop a proton with energy of about 12 MeV incident perpendicular to the detector surface. The downstream barrel consisted of a front layer (dE) $\sim 500\mu$m and back layer (E) $\sim 1000\mu$m, which is able to stop a proton of up to about 16 MeV incident perpendicular to the detector surface.

The detector configuration used is shown by the schematic in Fig. 5.5. In contrast
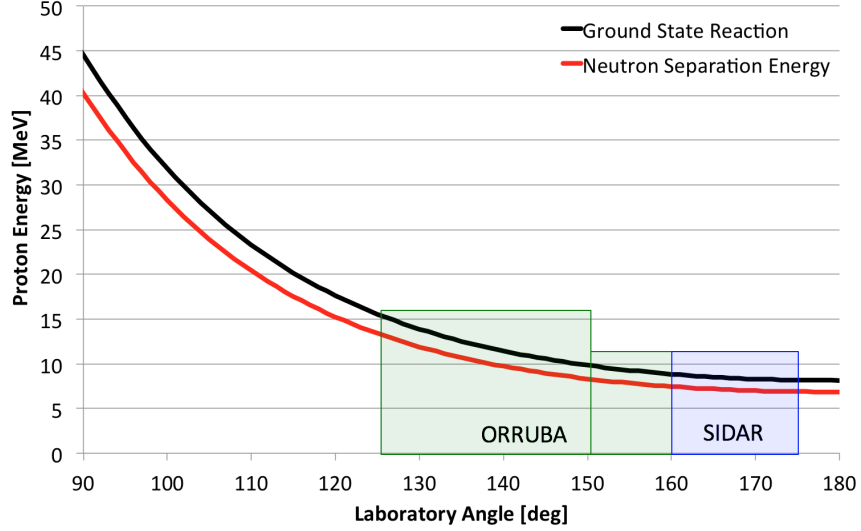
Figure 5.4: Kinematics calculation of the ejectile proton energies for the ground state and a state at the neutron separation energy from the $d(^{84}\text{Se}, p)^{85}\text{Se}$ reaction at 45 MeV/u. The shaded boxes indicate approximate angular coverage along the x-axis, and approximate punch through energy for protons through the various thicknesses of silicon of each array along the y-axis

to the $^{86}\text{Kr}(d, p)^{87}\text{Kr}$ measurement, most of the solid angle coverage for detecting the ejectile proton moved to backward angles in the laboratory. There was still a small amount of coverage at $\leq 90°$ in the laboratory to measure elastic scattering.

Another reason for covering the very backward angles in the laboratory when measuring (d, p) reactions with fast beams is because the cross section is largest at these angles, due to the inverse kinematics of the reaction. More importantly, these angles are forward center-of-mass angles where the direct reaction cross section is highest and has minimal compound contributions. Figure 5.6 shows FR-ADWA predicted cross sections for three different final states of the $d(^{84}\text{Se}, p)^{85}\text{Se}$ at 45 MeV/u along with the approximate angular coverage of each of the detector arrays.

The cross sections for each of the final states shown in Fig. 5.6 are highest at the most backward angles in the laboratory, and fall off rapidly towards 90°. It is especially important to cover angles with the highest cross section when measuring (d, p) reactions with radioactive nuclei in order to collect significant statistics in a
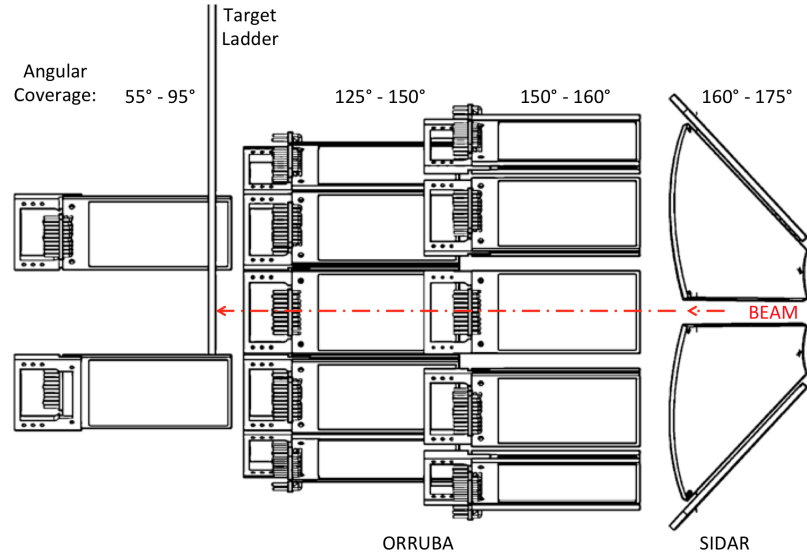
Figure 5.5: Schematic of the ORRUBA barrel and SIDAR as configured for the measurement of $d(^{84}\text{Se}, p)^{85}\text{Se}$ at 45 MeV/u. Overlayed are approximate angles covered by the detectors in the laboratory.

reasonable amount of beam time, which is typically about one week. Radioactive ion beam rates at the current accelerator facilities are usually around 10^5 pps or lower. Also, the purity of the beams are expected to be $\leq 70\%$, due to the fragmentation methods used to produce and separate the radioactive isotopes of interest.

Detected particles are gated on coincidences with ^{85}Se recoils detected in the focal plane of the S800. The S800 was triggered by events in ORRUBA, and events were synchronized using timestamps from a 10 MHz clock in the ORNL data acquisition system. To ensure synchronization between the S800 and ORRUBA, the timestamp differences were recorded over time and monitored for any drift. Preliminary reconstruction of particle energies as a function of scattering angle in the laboratory is shown in Fig. 5.7, with and without requiring concident events in the S800 to show how much of the fusion evaporation background is suppressed when requiring coincident events. Kinematic loci are visible in the most backward angles in the lab (i.e. $>140°$) corresponding to particles detected in SIDAR and the upstream barrel
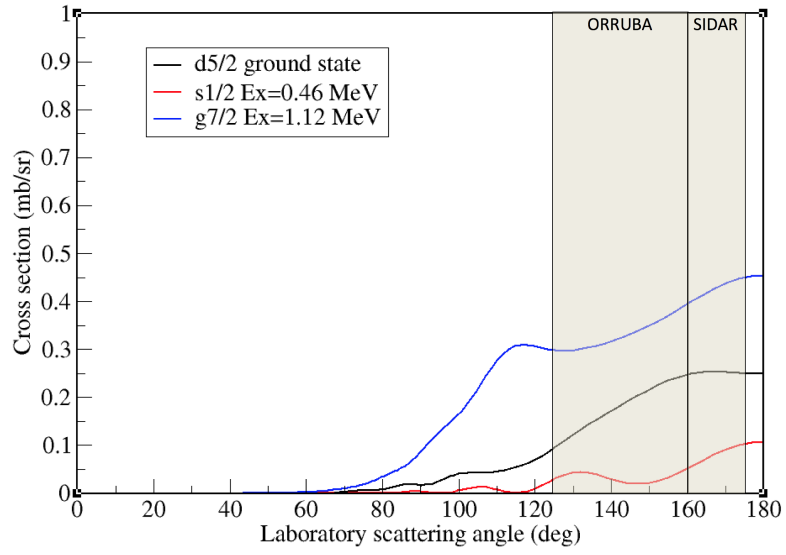
Figure 5.6: FR-ADWA calculated cross sections for three different final states from the $d(^{84}\mathrm{Se}, p)^{85}\mathrm{Se}$ reaction at 45 MeV/u. Shaded boxes indicate approximate angular coverage of each detector array ORRUBA and SIDAR.

of ORRUBA, when requiring a coincidence event from the S800 and ORRUBA. The downstream barrel of ORRUBA consisted of silicon telescopes with a 500 μm ΔE layer, which was sufficiently thick enough to stop the protons of interest from punching through to the E layer at scattering angles between $\sim$130 - 145°. The punch through energy for a proton impinging on a 500 μm thick silicon detector at an angle of 45° is 10.1 MeV. The ΔE layer detectors only recorded energy deposited and did not have position reconstruction capabilities in use during the experiment; therefore any particle that did not have sufficient energy to punch through to the E layer detector was not included in Fig. 5.7. This effect is seen as the gap of data below $\sim$10 MeV at scattering angles $<\approx$145° in Fig. 5.7.

We were not able to resolve the kinematic loci from different states in the downstream ORRUBA barrel. This is due to the lack of beam tracking as well as the straggling through the steep angles in the deuterated polyethylene target causing the kinematic loci to broaden. The C_2D_4 target thickness used in this measurement was $\sim$1.2 mg/cm^2, and was chosen to collect sufficient statistics with an expected low
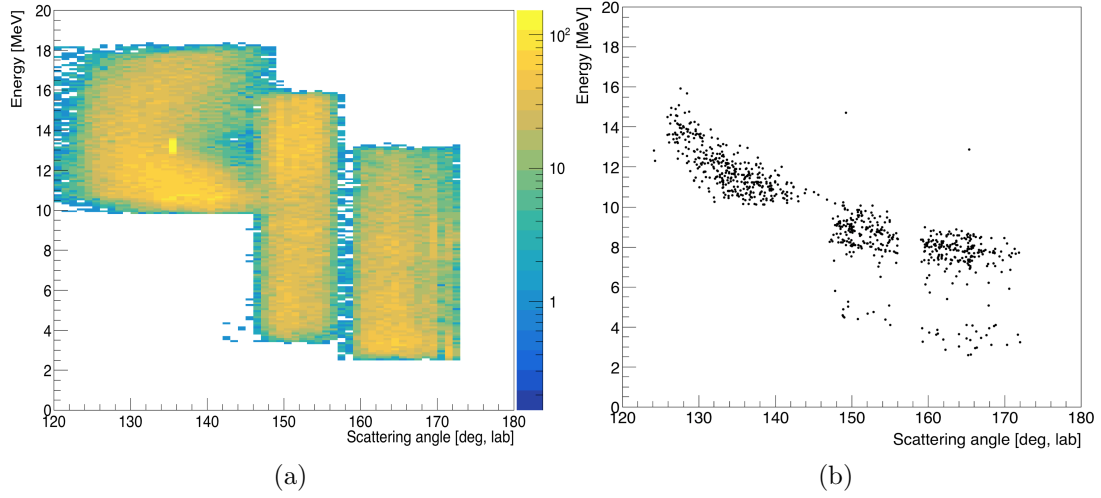
Figure 5.7: Charge particles detected in ORRUBA and SIDAR arrays as a function of scattering angle in the laboratory frame. (a) Particle singles with no gating (b) Particles are gated on ^{85}Se recoil detected in the S800 focal plane.

beam rate, which was on the order of 10^5 pps.

The features from the data in Fig. 5.7 are made apparent in the preliminary Q-value plot in Fig. 5.8, where the ground state Q-value for the reaction is 2.313 MeV [Joh15] and the excited states are at lower Q-value. Overlayed for reference are the low-lying excited states measured in Ref. [Tho07]. The data in Fig. 5.8 are gated on coincidences with ^{85}Se detected in the focal plane of the S800, and summed over angles >90° in the laboratory. The comparison of the levels measured in Ref. [Tho07] show that the higher energy measurement populates different final states at higher energy, and possibly higher angular momentum. Details of the states around an excitation energy of ~2.0 MeV, including spin-parities assignments, will require further analysis.

The analysis of the recent $d(^{84}\text{Se},p)^{85}$Se measurement at 45 MeV/u is still underway and has not yet reached the point to extract reliable differential cross sections for low-lying states of ^{85}Se. The future analysis and interpretation is part of the PhD dissertation project of Harrison Sims. Future results will detail the same combined measurement analysis for the low- and high-beam energies as was performed for the
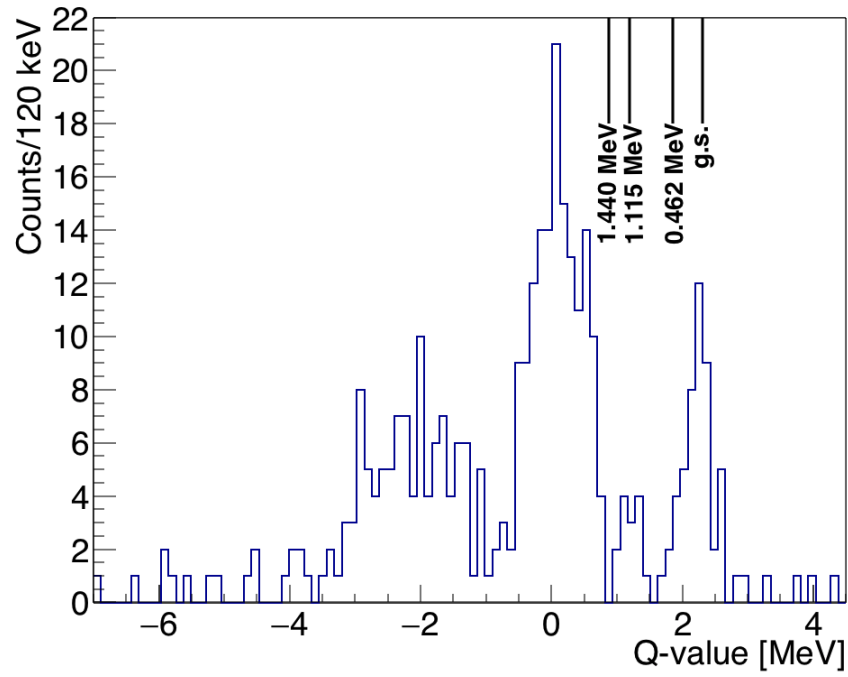
Figure 5.8: Q-value spectrum from the events shown in Fig. 5.7. Ground state (g.s.) Q-value for the $d(^{84}\text{Se},p)^{85}\text{Se}$ reaction is 2.313 MeV. A few excited states in ^{85}Se are labeled at the top of the plot.

$^{86}\text{Kr}(d,p)^{87}\text{Kr}$ reaction.

Chapter 6

Summary and Outlook

The $d(^{86}\text{Kr},p)^{87}\text{Kr}$ and $d(^{84}\text{Se},p)^{85}\text{Se}$ reactions were measured in inverse kinematics at 35 MeV/u and 45 MeV/u, respectively, at the National Superconducting Cyclotron Laboratory with the ORRUBA detector system coupled to the S800 magnetic spectrograph. These measurements aim to test the combined method proposed by Mukhamedzhanov and Nunes [Muk05] as a way of extracting spectroscopic factors with reduced ambiguities in neutron-rich isotopes by constraining the neutron bound-state potential.

The results from the $d(^{86}\text{Kr},p)^{87}\text{Kr}$ measurement were combined with those from a previously published study at 5.5 MeV/u [Har70]. The present work demonstrates that for the $\ell=2$ transfer to the ground state of ^{87}Kr, the single-particle ANC, and hence the bound-state potential, can be constrained from measurements at two energies using the combined method. A single-particle ANC of $b_{2d5/2}$=6.46 $^{+1.12}_{-0.57}$ fm was deduced for the ground state of ^{87}Kr, which constrained the spectroscopic factor to S=0.44 $^{+0.09}_{-0.13}$ fm. For an $\ell=4$ transfer to a state at excitation energy of Ex=2.52 MeV, it appears that the reaction, even at 35 MeV/u, remains peripheral, yielding statistically identical results to the low-energy measurement. This result could be contributed to the higher centrifugal barrier to transfer ($\ell=4$) compared to transfer to the $\ell=2$ ground state.

The present work has demonstrated that by combining measurements at two very different beam energies, the spANC $b_{\ell j}$ can be constrained and spectroscopic factors can be deduced with greater certainty. However, the spectroscopic factor extracted

in this work for the $5/2^+$ ground state of ^{87}Kr from the present combined method analysis is lower than previous analyses. There are ongoing efforts in the reaction theory community to better understand these differences and further develop the theoretical framework to enable the most valid extraction of spectroscopic factors. Extending the theoretical framework is beyond this experimental dissertation.

In order to confirm the success of the combined method in the mass range around A=80, and to apply it to a nucleus in the vicinity of possible r-process sensitivities, the recent $d(^{84}$Se$,p)^{85}$Se reaction measurement at 45 MeV/u will be combined with the peripheral measurement by Thomas *et al.* [Tho07] at 4.5 MeV/u. The many-body ANCs for low-lying states in ^{85}Se have been extracted using the FR-ADWA formalism and, similar to the ^{86}Kr case, are consistently lower than the ANCs extracted using the traditional DWBA. The analysis of the recent high-energy measurement will help to extract a spectroscopic factor consistent with the many-body ANC for a given final state when combined with the low-energy data.

Spectroscopic factors for relatively low-ℓ transfers determined with a reduced dependence on the bound-state potential will impact calculations of direct neutron capture rates on nuclei with low level densities near the neutron separation energy and near the waiting points during freeze-out from an r-process event.

6.0.1 Outlook

Further measurements on neutron-rich nuclei near closed nuclear shells are highly sought after due to their importance in r-process nucleosynthesis. However, the charged particle measurements become significantly more difficult further from stability due to lower beam rates, lower beam purity, and single-neutron strengths can be highly fragmented. It is crucial, in this sense, to have better energy resolution in order to resolve these highly fragmented single-particle states of radioactive nuclei, which in some cases can be as close as a few tens of keV in separation.

The ability to measure γ-rays from the de-excitation of excited states in the recoil nucleus in coincidence with charged particles emitted in the reaction would considerably helps to improve the energy resolution of charged particle measurements of neutron-rich nuclei. Also, recent efforts have validated the $(d, p\gamma)$ reaction as a surrogate for (n, γ) neutron capture reactions [Rat15], further strengthening the need for particle-gamma coincidence measurements. High-purity germanium (HPGe) detectors are traditionally used for their high energy resolution ($\sim$2 keV at E$_\gamma$=1.33 MeV) [Kno00]), although the efficiency of gamma-ray detection is low. Therefore, it is advantageous to use large HPGe arrays to maximize the detection efficiency without sacrificing energy resolution. The detector coupling GODDESS (Gammasphere ORRUBA Dual Detectors for Experimental Structure Studies) has been recently commissioned at Argonne National Laboratory to measure such particle-gamma coincidences [Pai17]. GODDESS combines the charged particle detector array ORRUBA, discussed in this work, with a large array of 110 Compton suppressed HPGe detectors that make up the Gammasphere array [Lee90]. A schematic of GODDESS is shown in Fig. 6.1. Beams of rare isotopes are made available with the CAlifornium Rare Isotope Breeder Upgrade (CARIBU) [Par07] accelerated through the Argonne Tandem Linac Accelerator System (ATLAS), providing radioactive beams around the fission fragment peaks of ^{252}Cf. The reactions $d(^{134}$Xe,$p\gamma)^{135}$Xe, $d(^{95}$Mo,$p\gamma)^{96}$Mo, and ^{16}F$(^{3}He, t\gamma)^{19}$Ne have been measured as the commissioning experiments for GODDESS.

Future measurements with GODDESS using radioactive ion beams to study nuclei near closed shells have been approved at Argonne National Laboratory, for example, $d(^{143}$Ba,$p\gamma)^{144}$Ba and $d(^{134}$Te,$p\gamma)^{135}$Te. These measurements would provide detailed spectroscopic information for nuclei that exhibit a complex spectra through the fragmentation of single-particle strengths and nuclear deformation, the details of which
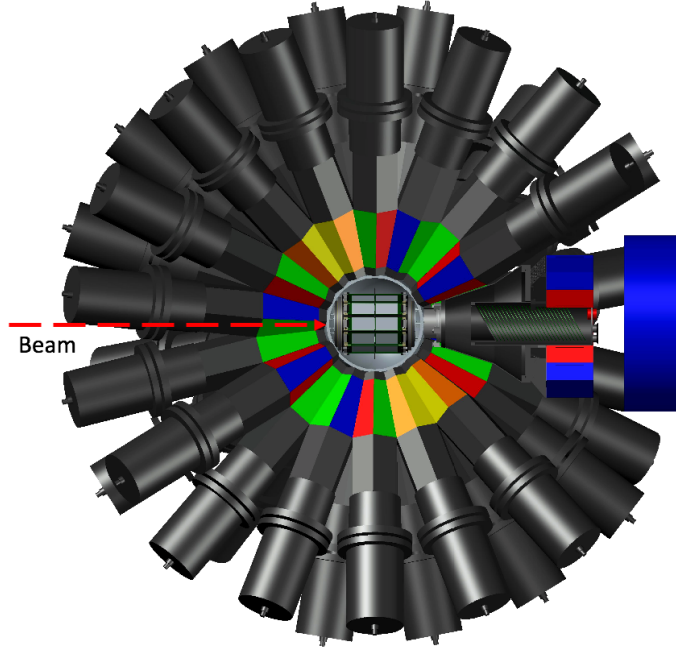
Figure 6.1: Schematic of ORRUBA detectors inside the Gammasphere array of HPGe detectors. Beam direction is shown by the red arrow. Directly downstream of the OR-RUBA scattering chamber is a high-rate ionization chamber for recoil identification. Figure adapted from Ref. [Pai14]

are previously unresolvable through charged particle measurements alone. These measurements help to understand the evolution of shell structure away from stability. In addition, the measured cross sections would be used to infer (n, γ) cross sections for direct neutron capture into low lying states, important for understanding abundances of r-process nuclei.

The upcoming $(d, p\gamma)$ measurements with GODDESS plan to use the Gamma-Ray Energy Tracking In-beam Nuclear Array (GRETINA) [Del99; Lee99], although ORRUBA can be coupled to many different gamma-ray detection systems including the Hybrid Array of Gamma Ray Detectors (HAGRiD) [Smi18], and the more longer term Gamma-Ray Energy Tracking Array (GRETA) [Del99; Lee99].

The proven capabilities of ORRUBA with fast beams at the NSCL with the measurements of states in ^{87}Kr and ^{85}Se from this work have paved the way to measure $d(^{80}\mathrm{Ge},p\gamma)^{81}\mathrm{Ge}$ at 40 MeV/u. This experiment has been approved to run in the

near future and will be the first fast-beam experiment to implement ORRUBA with HAGRiD, which is an array of LaBr$_3$ detectors [Smi18]. An example of a possible configuration for this experiment is shown in Fig. 6.2, where the scattering chamber is transparent to show the ORRUBA barrel and the cylinders surrounding the barrel represent the LaBr$_3$ crystals. This measurement would extract spectroscopic factors that can be combined with the measurements in Ref. [Ahn13] using the same methods in this work. Also, measuring $(d, p\gamma)$ would not only enhance the resolution in detecting the charged particle, but also provide information on nuclear states that are not populated through the reaction, but may be seen through γ cascades from excited states. This would provide crucial information of γ branches above the neutron separation energy which is necessary in providing a surrogate reaction for compound neutron capture (n, γ).
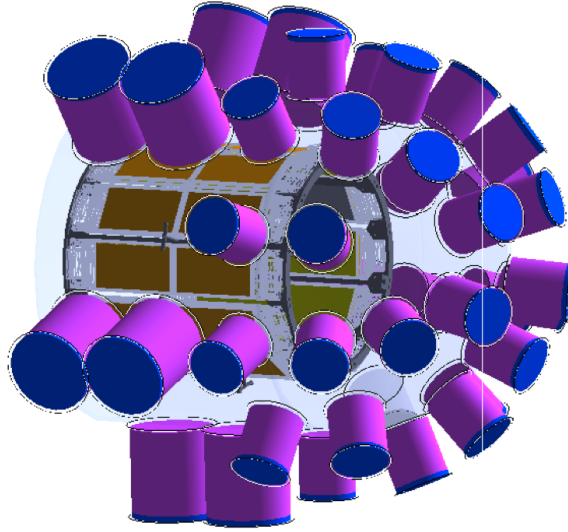
Figure 6.2: Schematic design of ORRUBA detectors in a possible configuration with the HAGRiD array of LaBr$_3$ scintillators for measuring $(d, p\gamma)$ reactions with fast beams at the NSCL/FRIB.

As discussed in section 5.2, the design requirements for measuring transfer reactions with fast beams require a reconfiguration from the experiments designed for

lower energy measurements. The Facility for Rare Isotope Beams (FRIB) at Michigan State University is the future of radioactive ion beam experiments in the U.S., promising to provide greater beam intensities and extend the reach of available beams further away from stability. New advancements in nuclear reaction theory along with transfer reaction measurements with fast beams and particle-gamma coincidences will be crucial for future experiments exploring this previously un-reachable area of the nuclear landscape.

Bibliography

[Abb17]   B. P. Abbott et al. "GW170817: Observation of Gravitational Waves from
           a Binary Neutron Star Inspiral". In: *Phys. Rev. Lett.* 119 (16 Oct. 2017),
           p. 161101.

[Abo95]   Y. Aboussir et al. "Nuclear mass formula via an approximation to the
           Hartree-Fock method". In: *Atomic Data and Nuclear Data Tables* 61.1
           (1995), pp. 127–176. ISSN: 0092-640X.

[Ahn13]   S. Ahn. "The study of nuclear structure of neutron-rich ^{81}Ge and its con-
           tribution in the r-process via the neutron transfer reaction ^{80}Ge(d,p)".
           PhD thesis. University of Tennessee - Knoxville, Aug. 2013.

[Arm13]   Wilfred L.F. Armarego and Christina Chai. "Chapter 4 - Purification of
           Organic Chemicals". In: *Purification of Laboratory Chemicals (Seventh
           Edition)*. Ed. by Wilfred L.F. Armarego and Christina Chai. Seventh Edi-
           tion. Boston: Butterworth-Heinemann, 2013, pp. 103–554. ISBN: 978-0-12-
           382161-4.

[Arn07]   M. Arnould, S. Goriely, and K. Takahashi. "The r-process of stellar nucle-
           osynthesis: Astrophysics and nuclear physics achievements and mysteries".
           In: *Phys. Rep.* 450 (2007), p. 97.

[Aus70]   N. Austern. *Direct Nuclear Reaction Theories*. John Wiley and Sons Inc,
           1970.

[Bai16]   G. W. Bailey, N. K. Timofeyuk, and J. A. Tostevin. "Sensitivity of (d, p) Reactions to High $n-p$ Momenta and the Consequences for Nuclear Spectroscopy Studies". In: *Phys. Rev. Lett.* 117 (16 Oct. 2016), p. 162502.

[Bar01]   D. W. Bardayan et al. "Destruction of ^{18}F via ^{18}F$(p, \alpha)^{15}$O burning through the $E_{\text{c.m.}} = 665$ keV resonance". In: *Phys. Rev. C* 63 (6 May 2001), p. 065802.

[Baz03]   D. Bazin et al. "The {S800} spectrograph". In: *Nuclear Instruments and Methods in Physics Research Section B: Beam Interactions with Materials and Atoms* 204 (2003). 14th International Conference on Electromagnetic Isotope Separators and Techniques Related to their Applications, pp. 629–633. ISSN: 0168-583X.

[Ber05]   M.J. Berger et al. *ESTAR, PSTAR, and ASTAR: Computer Programs for Calculating Stopping-Power and Range Tables for Electrons, Protons, and Helium Ions (version 1.2.3)*. National Institute of Standards and Technology, Gaithersburg, MD http://physics.nist.gov/Star. 2005.

[Ber73]   I.B. Berlman and O.J. Steingraber. "Liquid scintillation solutions for pulse-shape discrimination". In: *Nuclear Instruments and Methods* 108.3 (1973), pp. 587–591. ISSN: 0029-554X.

[Ber90]   Martin Berz. "Computational aspects of optics design and simulation: COSY INFINITY". In: *Nuclear Instruments and Methods in Physics Research Section A: Accelerators, Spectrometers, Detectors and Associated Equipment* 298.1 (1990), pp. 473–479. ISSN: 0168-9002.

[Ber93]   M. Berz et al. "Reconstructive correction of aberrations in nuclear particle spectrographs". In: *Phys. Rev. C* 47 (2 Feb. 1993), pp. 537–544.

[Bin18]   Average Binding. Energy per Nucleon `http://mrwhibley.weebly.com/nuclear-binding-energy.html`. 2018.

[Bir72]   J.B. Birks and G. Poullis. *Liquid Scintillators*. Heyden and Son ltd, 1972.

[CAE18]   CAEN. Electronic Instrumentation `http://www.caen.it`. 2018.

[Cat02]   W.N. Catford. "Nucleon transfer studies with radioactive beams". In: *Nuclear Physics A* 701.1 (2002). 5th International Conference on Radioactive Nuclear Beams, pp. 1–6. ISSN: 0375-9474.

[Chi08]   S. Chiba et al. "Direct and semi-direct capture in low-energy (n, γ) reactions of neutron-rich tin isotopes and its implications for r-process nucleosynthesis". In: *Phys. Rev. C* 77 (1 Jan. 2008), p. 015809.

[Cle78]   Terrance P. Cleary. "The 88Sr(d, p) reaction and the structure of 89Sr". In: *Nuclear Physics A* 301.2 (1978), pp. 317–335. ISSN: 0375-9474.

[Cow99]   John J. Cowan et al. "r-Process Abundances and Chronometers in Metal-poor Stars". In: *The Astrophysical Journal* 521.1 (1999), p. 194.

[Dae80]   W. W. Daehnick, J. D. Childs, and Z. Vrcelj. "Global optical model potential for elastic deuteron scattering from 12 to 90 MeV". In: *Phys. Rev. C* 21 (6 June 1980), pp. 2253–2274.

[Del99]   M.A. Deleplanque et al. "GRETA: utilizing new concepts in γ-ray detection". In: *Nuclear Instruments and Methods in Physics Research Section A: Accelerators, Spectrometers, Detectors and Associated Equipment* 430.2 (1999), pp. 292–310. ISSN: 0168-9002.

[Dob96]   J. Dobaczewski et al. "Mean-field description of ground-state properties of drip-line nuclei: Pairing and continuum effects". In: *Phys. Rev. C* 53 (6 June 1996), pp. 2809–2840.

[Eng07]   George L. Engel et al. "A multi-channel integrated circuit for use in low- and intermediate-energy nuclear physics-HINP16C". In: *Nuclear Instruments and Methods in Physics Research Section A: Accelerators, Spectrometers, Detectors and Associated Equipment* 573.3 (2007), pp. 418–426. ISSN: 0168-9002.

[Fam17]   Mike Famiano. private communication. 2017.

[Feb17]   M. Febbraro et al. "Improved technique for preparation of deuterated-polyethylene targets". In: *Nuclear Instruments and Methods in Physics Research Section B: Beam Interactions with Materials and Atoms* 410 (2017), pp. 53–59. ISSN: 0168-583X.

[Feb18a]   M. Febbraro et al. "Development of an array of liquid-scintillator-based bar detectors: SABRE". In: *Nuclear Instruments and Methods in Physics Research Section A: Accelerators, Spectrometers, Detectors and Associated Equipment* (2018). ISSN: 0168-9002.

[Feb18b]   Mike Febbraro. private communication. 2018.

[Gad14]   Alexandra Gade, C. Konrad Gelbke, and Thomas Glasmacher. "NSCL and the Facility for Rare Isotope Beams (FRIB) Project". In: *Nuclear Physics News* 24.1 (2014), pp. 28–30.

[Gil13]   A. Gillibert et al. "Windowless thin solid-hydrogen target: CHyMENE". In: *The European Physical Journal A* 49.12 (Dec. 2013), p. 155. ISSN: 1434-601X.

[Góm18]   M. Gómez-Ramos and N. K. Timofeyuk. "Reduced sensitivity of the (d, p) cross sections to the deuteron model beyond the adiabatic approximation". In: *Phys. Rev. C* 98 (1 July 2018), p. 011601.

[Ham18]   Hamamatsu. Photonics www.Hamamatsu.com. 2018.

[Har70]   K. Haravu et al. "^{86}Kr$(d,p)^{87}$Kr". In: *Phys. Rev. C* 1 (3 May 1970), pp. 938–944.

[Hau52]   Walter Hauser and Herman Feshbach. "The Inelastic Scattering of Neutrons". In: *Phys. Rev.* 87 (2 July 1952), pp. 366–373.

[Hax49]   Otto Haxel, J. Hans D. Jensen, and Hans E. Suess. "On the "Magic Numbers" in Nuclear Structure". In: *Phys. Rev.* 75 (11 June 1949), pp. 1766–1766.

[Hon04]   Satoshi Honda et al. "Spectroscopic Studies of Extremely Metal-Poor Stars with the Subaru High Dispersion Spectrograph. II. The r-Process Elements, Including Thorium". In: *The Astrophysical Journal* 607.1 (2004), p. 474.

[Hor70]   Donald L. Horrocks. "Scintillation Efficiencies at High Solute Concentrations: Possible Energy Transfer from S3 States of Excited Aromatic Solvents". In: *The Journal of Chemical Physics* 52.3 (1970), pp. 1566–1572.

[Joh15]   T.D. Johnson and W.D. Kulp. "Data extracted from the ENSDF database". In: *Nucl. Data Sheets* 129.1 (2015).

[Joh70]   R. C. Johnson and P. J. R. Soper. "Contribution of Deuteron Breakup Channels to Deuteron Stripping and Elastic Scattering". In: *Phys. Rev. C* 1 (3 Mar. 1970), pp. 976–990.

[Joh74]   R.C. Johnson and P.C. Tandy. "An approximate three-body theory of deuteron stripping". In: *Nuclear Physics A* 235.1 (1974), pp. 56–74. ISSN: 0375-9474.

[Kas17]   D. Kasen et al. "Origin of the heavy elements in binary neutron-star mergers from a gravitational-wave event". In: *Nature* 551 (Oct. 2017), p. 80.

[KJ18]   K&J. Magnetics ,Inc. `https://www.kjmagnetics.com`. 2018.

[Kla09]   Petr Klan and Jakob Wirz. *Photochemistry of Organic Compounds From Concepts to Practice.* John Wiley and Sons, Ltd, 2009.

[Kno00]   G. Knoll. *Radiation Detection and Measurement.* Wiley, 2000.

[Kon03]   A.J. Koning and J.P. Delaroche. "Local and global nucleon optical models from 1 keV to 200 MeV". In: *Nuclear Physics A* 713.3 (2003), pp. 231–310. ISSN: 0375-9474.

[Koz12]   R. L. Kozub et al. "Neutron Single Particle Structure in ^{131}Sn and Direct Neutron Capture Cross Sections". In: *Phys. Rev. Lett.* 109 (17 Oct. 2012), p. 172501.

[Kra96]   E. Krausmann et al. "Direct neutron capture for magic-shell nuclei". In: *Phys. Rev. C* 53 (1 Jan. 1996), pp. 469–474.

[Kra98]   K.S. Krane. *Indroductory Nuclear Physics.* John Wiley and Sons Inc, 1998.

[Lai93]   A. Laid, J. A. Tostevin, and R. C. Johnson. "Deuteron breakup effects in transfer reactions using a Weinberg state expansion method". In: *Phys. Rev. C* 48 (3 Sept. 1993), pp. 1307–1317.

[Lee90]   I-Yang Lee. "The GAMMASPHERE". In: *Nuclear Physics A* 520 (1990). Nuclear Structure in the Nineties, pp. c641–c655. ISSN: 0375-9474.

[Lee99]   I.Y. Lee. "Gamma-ray tracking detectors". In: *Nuclear Instruments and Methods in Physics Research Section A: Accelerators, Spectrometers, Detectors and Associated Equipment* 422.1 (1999), pp. 195–200. ISSN: 0168-9002.

[Liu04]   X. D. Liu et al. "Systematic extraction of spectroscopic factors from ^{12}C$(d,p)^{13}$C and ^{13}C$(p,d)^{12}$C reactions". In: *Phys. Rev. C* 69 (6 June 2004), p. 064313.

[Loh74]   J.M. Lohr and W. Haeberli. "Elastic scattering of 9-13 MeV vector polarized deuterons". In: *Nuclear Physics A* 232.2 (1974), pp. 381–397. ISSN: 0375-9474.

[Lov17]   A. E. Lovell et al. "Energy dependence of nonlocal optical potentials". In: *Phys. Rev. C* 96 (5 Nov. 2017), p. 051601.

[Mar01]   F Marti et al. "Commissioning of the Coupled Cyclotron system at NSCL". In: *AIP Conference Proceedings* 600 (Dec. 2001).

[May48]   Maria G. Mayer. "On Closed Shells in Nuclei". In: *Phys. Rev.* 74 (3 Aug. 1948), pp. 235–239.

[May49]   Maria Goeppert Mayer. "On Closed Shells in Nuclei. II". In: *Phys. Rev.* 75 (12 June 1949), pp. 1969–1970.

[McC14]   M. McCleskey et al. "Determination of the asymptotic normalization coefficients for $^{14}C + n \leftrightarrow ^{15}C$, the $^{14}C(n,\gamma)^{15}C$ reaction rate, and evaluation of a new method to determine spectroscopic factors". In: *Phys. Rev. C* 89 (4 Apr. 2014), p. 044605.

[Men71]   J. J. H. Menet et al. "Total-Reaction-Cross-Section Measurements for 30-60-MeV Protons and the Imaginary Optical Potential". In: *Phys. Rev. C* 4 (4 Oct. 1971), pp. 1114–1129.

[Mes18]   Mesytec. GmbH & Co. KG `www.mesytec.com`. 2018.

[Mic18]   Micron. Semiconductor Ltd. `http://www.micronsemiconductor.co.uk`. 2018.

[Muk01]   A. M. Mukhamedzhanov, C. A. Gagliardi, and R. E. Tribble. "Asymptotic normalization coefficients, spectroscopic factors, and direct radiative capture rates". In: *Phys. Rev. C* 63 (2 Jan. 2001), p. 024612.

[Muk05]   A. M. Mukhamedzhanov and F. M. Nunes. "Combined method to extract spectroscopic information". In: *Phys. Rev. C* 72 (1 July 2005), p. 017602.

[Muk08]   A. M. Mukhamedzhanov, F. M. Nunes, and P. Mohr. "Benchmark on neutron capture extracted from (d, p) reactions". In: *Phys. Rev. C* 77 (5 May 2008), p. 051601.

[Mum16]   M. R. Mumpower et al. "The impact of individual nuclear properties on r-process nucleosynthesis". In: *Prog. Part. Nucl. Phys.* 86 (2016). [Erratum: Prog. Part. Nucl. Phys. **87**, 116 (2016)], pp. 86–126.

[Nak10]   Kimitsugu Nakamura et al. "Latest bialkali photocathode with ultra high sensitivity". In: *Nuclear Instruments and Methods in Physics Research Section A: Accelerators, Spectrometers, Detectors and Associated Equipment* 623.1 (2010). 1st International Conference on Technology and Instrumentation in Particle Physics, pp. 276–278. ISSN: 0168-9002.

[Ngu10]   N. B. Nguyen, F. M. Nunes, and R. C. Johnson. "Finite-range effects in (d, p) reactions". In: *Phys. Rev. C* 82 (1 July 2010), p. 014611.

[NSC18]   National Superconducting Cyclotron Laboratory NSCL. `http://nscl.msu.edu/public/science/isotope.html`. 2018.

[Nuc18]   Nuclear. Chart `http://www.phys.utk.edu/expnuclear/nucastro.html`. 2018.

[Nun11]   F. M. Nunes and A. Deltuva. "Adiabatic approximation versus exact Faddeev method for (d, p) and (p, d) reactions". In: *Phys. Rev. C* 84 (3 Sept. 2011), p. 034607.

[Pai07]   S.D. Pain et al. "Development of a high solid-angle silicon detector array for measurement of transfer reactions in inverse kinematics". In: *Nuclear*

Instruments and Methods in Physics Research Section B: Beam Interactions with Materials and Atoms 261.1 (2007), pp. 1122–1125. ISSN: 0168-583X.

[Pai09] S. D. Pain et al. "Development of the ORRUBA Silicon Detector Array". In: *AIP Conference Proceedings* 1090.1 (2009), pp. 570–572.

[Pai14] S. D. Pain. "Advances in instrumentation for nuclear astrophysics". In: *AIP Advances* 4.4 (2014), p. 041015. eprint: `https://doi.org/10.1063/1.4874116`.

[Pai17] S.D. Pain et al. "Direct Reaction Measurements Using GODDESS". In: *Physics Procedia* 90 (2017). Conference on the Application of Accelerators in Research and Industry, CAARI 2016, 30 October - 4 November 2016, Ft. Worth, TX, USA, pp. 455–462. ISSN: 1875-3892.

[Pan07] D. Y. Pang, F. M. Nunes, and A. M. Mukhamedzhanov. "Are spectroscopic factors from transfer reactions consistent with asymptotic normalization coefficients?" In: *Phys. Rev. C* 75 (2 Feb. 2007), p. 024601.

[Pan13] D. Y. Pang et al. "Rapid convergence of the Weinberg expansion of the deuteron stripping amplitude". In: *Phys. Rev. C* 87 (6 June 2013), p. 064613.

[Pan14] D. Y. Pang and A. M. Mukhamedzhanov. "Asymptotic normalization coefficients and spectroscopic factors from deuteron stripping reactions". In: *Phys. Rev. C* 90 (4 Oct. 2014), p. 044611.

[Par07] Richard C. Pardo et al. "Radioactive beams from 252Cf fission using a gas catcher and an ECR charge breeder at ATLAS". In: *Nuclear Instruments and Methods in Physics Research Section B: Beam Interactions with Materials and Atoms* 261.1 (2007). The Application of Accelerators in Research and Industry, pp. 965–968. ISSN: 0168-583X.

[Pea96]   J.M. Pearson, R.C. Nayak, and S. Goriely. "Nuclear mass formula with Bogolyubov-enhanced shell-quenching: application to r-process". In: *Physics Letters B* 387.3 (1996), pp. 455–459. ISSN: 0370-2693.

[Per76]   C.M. Perey and F.G. Perey. "Compilation of phenomenological optical-model parameters 1954-1975". In: *Atomic Data and Nuclear Data Tables* 17.1 (1976), pp. 1–101.

[Pfe01]   B. Pfeiffer et al. "Nuclear structure studies for the astrophysical r-process". In: *Nuclear Physics A* 693.1 (2001). Radioactive Nuclear Beams, pp. 282–324. ISSN: 0375-9474.

[Qia03]   Y.-Z. Qian. "The origin of the heavy elements: Recent progress in the understanding of the r-process". In: *Progress in Particle and Nuclear Physics* 50.1 (2003), pp. 153–199. ISSN: 0146-6410.

[Qua18]   Quantar. Technology ,Inc. `http://www.quantar.com`. 2018.

[Ran09]   David W. H. Rankin. *CRC handbook of chemistry and physics, 89th edition, edited by David R. Lide.* Vol. 15. Taylor & Francis, July 2009, pp. 223–224.

[Rat15]   Ratkiewicz, A. et al. "Validating (d,p) a Surrogate for Neutron Capture". In: *EPJ Web of Conferences* 93 (2015), p. 02012.

[Rat73]   R.D. Rathmell, P.J. Bjorkholm, and W. Haeberli. "Vector analysing power and cross section for 90Zr(d, p)91Zr at 11 and 12 MeV". In: *Nuclear Physics A* 206.3 (1973), pp. 459–476. ISSN: 0375-9474.

[Rau98]   T. Rauscher et al. "Dependence of direct neutron capture on nuclear-structure models". In: *Phys. Rev. C* 57 (4 Apr. 1998), pp. 2031–2039.

[Rei68]   Roderick V Reid. "Local phenomenological nucleon-nucleon potentials". In: *Annals of Physics* 50.3 (1968), pp. 411–448. ISSN: 0003-4916.

[Rog15] A.M. Rogers et al. "Tracking rare-isotope beams with microchannel plates". In: *Nuclear Instruments and Methods in Physics Research Section A: Accelerators, Spectrometers, Detectors and Associated Equipment* 795 (2015), pp. 325–334. ISSN: 0168-9002.

[Ros15] A. Ross et al. "Effects of nonlocal potentials on (p, d) transfer reactions". In: *Phys. Rev. C* 92 (4 Oct. 2015), p. 044607.

[S8018] NSCL Magnetic Spectrograph S800. `https://wikihost.nscl.msu.edu/S800Doc/doku.php`. 2018.

[Sas65] Richard E. Sass, Baruch Rosner, and Edward J. Schneid. "$Kr^{86}(d, p)Kr^{87}$". In: *Phys. Rev.* 138 (2B Apr. 1965), B399–B404.

[Sat83] G.R. Satchler. *Direct Nuclear Reactions*. Clerendon Press, 1983.

[Sha00] D. Shapira, T.A. Lewis, and L.D. Hulett. "A fast and accurate position-sensitive timing detector based on secondary electron emission". In: *Nuclear Instruments and Methods in Physics Research Section A: Accelerators, Spectrometers, Detectors and Associated Equipment* 454.2 (2000), pp. 409–420. ISSN: 0168-9002.

[Sha13] D. K. Sharp et al. "Neutron single-particle strength outside the $\mathbf{N = 50}$ core". In: *Phys. Rev. C* 87 (1 Jan. 2013), p. 014312.

[Smi18] K. Smith et al. "First data with the Hybrid Array of Gamma Ray Detector (HAGRiD)". In: *Nuclear Instruments and Methods in Physics Research Section B: Beam Interactions with Materials and Atoms* 414 (2018), pp. 190–194. ISSN: 0168-583X.

[Sto05] A. Stolz et al. "Production of rare isotope beams with the NSCL fragment separator". In: *Nuclear Instruments and Methods in Physics Research Section B: Beam Interactions with Materials and Atoms* 241.1 (2005). The

Application of Accelerators in Research and Industry, pp. 858–861. ISSN: 0168-583X.

[Sur09]   R. Surman et al. "Neutron capture rates near $A = 130$ that effect a global change to the r-process abundance distribution". In: *Phys. Rev. C* 79 (4 Apr. 2009), p. 045809.

[Sur14]   R. Surman et al. "Sensitivity studies for the weak r process: neutron capture rates". In: *AIP Advances* 4.4 (2014), p. 041008.

[Tan17]   Masahiko Taniguchi and Jonathan S. Lindsey. "Database of Absorption and Fluorescence Spectra of >300 Common Compounds for use in PhotochemCAD". In: *Photochemistry and Photobiology* 94.2 (2017), pp. 290–327.

[Tho07]   J. S. Thomas et al. "Single-neutron excitations in neutron-rich ^{83}Ge and ^{85}Se". In: *Phys. Rev. C* 76 (4 Oct. 2007), p. 044302.

[Tho09]   Ian J Thompson and Filomena M Nunes. *Nuclear reactions for astrophysics: principles, calculation and applications of low-energy reactions.* Cambridge: Cambridge Univ. Press, 2009.

[Tho88]   Ian J. Thompson. "Coupled reaction channels calculations in nuclear physics". In: *Computer Physics Reports* 7.4 (1988), pp. 167–212. ISSN: 0167-7977.

[Tit16]   L. J. Titus, F. M. Nunes, and G. Potel. "Explicit inclusion of nonlocality in (d, p) transfer reactions". In: *Phys. Rev. C* 93 (1 Jan. 2016), p. 014604.

[Tos14]   J.A. Tostevin. *University of Surrey version of the code TWOFNR (of M. Toyama, M. Igarashi and N. Kishida) and code FRONT.* private communication. 2014.

[Tsu17]   K. Tsukada et al. "First Elastic Electron Scattering from ^{132}Xe at the SCRIT Facility". In: *Phys. Rev. Lett.* 118 (26 June 2017), p. 262501.

[Var91]   R.L. Varner et al. "A global nucleon optical model potential". In: *Physics Reports* 201.2 (1991), pp. 57–119. ISSN: 0370-1573.

[Ver68]   V.V. Verbinski et al. "Calibration of an organic scintillator for neutron spectrometry". In: *Nuclear Instruments and Methods* 65.1 (1968), pp. 8–25. ISSN: 0029-554X.

[Wal07]   M. S. Wallace et al. "The high resolution array (HiRA) for rare isotope beam experiments". In: *Nuclear Instruments and Methods in Physics Research, Section A: Accelerators, Spectrometers, Detectors and Associated Equipment* 583.2-3 (Dec. 2007), pp. 302–312. ISSN: 0168-9002.

[Wu99]   X. Wu et al. "The K500-to-K1200 coupling line for the coupled cyclotron facility at the NSCL". In: *Proceedings of the 1999 Particle Accelerator Conference (Cat. No.99CH36366)*. Vol. 2. Mar. 1999, pp. 1318–1320.

[Yur99]   J Yurkon et al. "Focal plane detector for the S800 high-resolution spectrometer". In: *Nuclear Instruments and Methods in Physics Research Section A: Accelerators, Spectrometers, Detectors and Associated Equipment* 422.1 (1999), pp. 291–295. ISSN: 0168-9002.